OPEN ACCESS

EUROPEAN MECHANICAL SCIENCE

ISSN: 2587-1110

Volume 5
Issue 4
December 2021

Editor in Chief: M. Ozcanli

EUROPEAN MECHANICAL SCIENCE

Indexed / Abstracted in:

TR-Dizin, CrossRef, Index Copernicus, Journal Factor, Rootindexing, ResearchBip, JournalFactor, JIFACTOR, Google Scholar, I2OR, Cosmos Impact Factor, International Innovative Journal Impact Factor (IIJIF), Scientific Indexing Services, InfoBase Index, Scientific Journal Impact Factor

Aims and Scopes

European Mechanical Science (EMS) is an international, peer reviewed journal which publishes full length original research papers, reviews related to all areas of Mechanical Engineering such as: Solid Mechanics, Materials Engineering, Automotive Engineering, Fluid Mechanics, Thermal Engineering, Engine and Power Engineering, Dynamics & Control, Robotics & Mechatronics, Transportation Engineering, Computational Mechanics, Design, Systems, Manufacturing, Bio-Medical Engineering; Process Engineering, Aerospace Engineering. No charges are required from the Authors to publish the articles.EMS is a quarterly published journal operating an online submission and peer review system. It allows authors to submit articles online and track their progress via its web interface.

http://dergipark.gov.tr/ems

EUROPEAN MECHANICAL SCIENCE

Contents

— *Research Paper*

EUROPEAN MECHANICAL SCIENCE
e-ISSN: 2587-1110

Research Paper

An Experimental Investigation of the Flow Structure on a Face Mannequin With / Without a Face Shield

Cemre Polat[1], Dogan Burak Saydam[1*], Mustafa Soyler[1], Coskun Ozalp[1]

[1]Osmaniye Korkut Ata University, Faculty of Engineering, Department of Energy Systems Engineering, Osmaniye, Turkey.

Abstract

This study investigated experimentally the flow regime with a face shield on a face mannequin placed at different distances (L=50 cm and L=150 cm to source of flow), i.e., perpendicular to the channel or at an angle of 10°, through the PIV (Particle Imaging Velocimetry) method along with the dye experiments, based on which the face shield and dye injector were positioned to conduct the PIV tests. As a result of the experiments, instantaneous velocity vectors and velocity magnitude data were obtained, and the flow structure around the face shield was examined in detail. The study revealed that the flow released through the respiratory tract hit the face and eye area of the mannequin in the experiments performed without using a face shield, yet, with the face shield, the flow that emerged while talking at a close distance was directed from the lower part of the face shield towards the neck and jaw but protected the face and eye area compared to the case without a face shield. It was observed that the flow lost its energy when it first left the flow source, and the velocity vectors were directed down the neck area. Positioning the mannequin at an angle of 10° turned out to be less protective than positioning it perpendicular to the channel, due to the flow being directed from the jaw to the mouth area with the effect of the angle.

Keywords: Social Distance, Face Shield, Flow Characteristic, Covid-19, PIV

1. INTRODUCTION

It is stated by health authorities that COVID-19 is rapidly transmitted by respiratory tract or contact [1]. In recent years, it has been observed that viral spread has dispersed groups of infectious particles [2]. Biological particles from bacteria, viruses and fungi can be found in the air that is breathing [3]. Droplets carrying infectious virus are ejected by an infected person because of activities such as breathing, coughing, speaking, and sneezing, and these particles, which can be carried, can be made to surfaces or suspended in the air, can be inhaled or taken into the body by people who are not adequately protected or who do not pay much attention to hand hygiene [4, 5]. Considering this situation, infectious disease outbreaks are likely to spread in places where there is a high human population in public spaces, office spaces, lecture halls, public transportation [6]. The typical breathing processes of an individual can be classified as breathing- i.e., inhaling and exhaling- talking, laughing, coughing, and sneezing. Human respiration changes according to the respiration rate. Depending on the intensity of breathing, talking, coughing and sneezing, an air flow occurs through the respiratory tract, within which particles of various sizes exist. Particles can lose their initial high velocity due to air friction after the first moment they leave the source, and it is, therefore, crucial to understand the movement of particles caused by coughing, sneezing, talking, and breathing to control the spread of infectious respiratory diseases [7-9].

The use of personal protective equipment (PPE) is essential to reduce or prevent people and especially healthcare workers from the risk of getting infected [10]. In particular, healthcare-related infection risks can be encountered in healthcare facilities around the world [11]. Considering this situation, PPE designed and recommended to be used especially for healthcare workers acts as a shield between healthcare workers and viruses [12]. It is also known that using a protective face mask is effective in reducing the risk of contagion due to coronavirus particles transmitted by droplets and aerosols [13]. Surgical masks have been a part of healthcare workers' clothing for over 100 years. Surgical masks are developed to filter and prevent the spread of microorganisms in the mouth [14]. Not only masks, but also gloves, goggles, face shields and aprons are used extensively as PPE in infections where the risk of transmission is high [15]. Especially healthcare professionals are in the high-risk group as they work in close proximity to the face of patients during the treatment of Covid-19 [16]. Healthcare profes-

* Corresponding author
Email: doganburaksaydam@osmaniye.edu.tr

European Mechanical Science (2021), 5(4): 153-160
doi: https://doi.org/10.26701/ems.907162
Received: March 31, 2021
Accepted: May 29, 2021

sionals use such equipment as face shields as a physical barrier to wear on the head to prevent direct contact with the droplets during some droplet-producing procedures such as intubation and respiratory physiotherapy [17]. This kind of equipment is designed to reduce the risk of direct exposure to infective droplets through splash [18].

There are limited studies in the literature on the behavior of personal protective equipment under a flow. However, it is possible to see many different experimental and numerical studies in which breathing, speaking, coughing, and sneezing reactions are simulated from the starting point whereas the flow movements of these situations are examined under different conditions in an environment [19-26]. In the study by Licinia et al. [21], the researchers examined the velocity field around the mannequin under two different ambient temperatures and body postures, and the effects of different types of clothing, chair design and table positioning on the airflow properties of the breathing zone for a sitting mannequin. Badeau et al. [22], examined the impacts of microorganism transport in confined spaces during coughing process in relation to computational fluid dynamics of particles and flow-field behavior in a designed square chamber. Using Computational Fluid Dynamics (CFD), Ge et al. [23], conducted a numerical study to analyze the inhalation of particles by a mannequin in a closed space with a ventilation system. Richmond-Bryant [24], who used the computational fluid dynamics simulations, examined the characteristics of the dimensional velocity and concentration profiles of airflow, which could cause healthcare workers to be exposed to a pathogenic substance in the air in the infection isolation room (AIIR). Tang et al. [25], researchers have visualized the sneezing and breathing states of healthy volunteers using a real-time shadow graph display technique. Clark and Golf [26], examined the interaction of airborne dispersion of photogenic particles and droplets with ventilation in an operating room environment.

As can be seen in the literature review, many researchers examined the flow structure of the distribution of the air flow and the number of particles, especially because of talking or breathing, in different simulations. Understanding the motion of a liquid or a molecule within the flow is as important as the motion of fluid on bodies. For this, in this study, contrary to the literature, the flow structure around a bluff body (face shield) was investigated experimentally, independent of particle density and particle amount. The main purpose of this study is to examine the flow structure around the face shield used as personal protective equipment. This study conducted two different experiments in which the distances between the two mannequin heads were 50 cm and 150 cm, respectively, to determine the flow characteristics of the face shield. First the dye and then the particles for PIV experiments were sent by an adjustable pump from the first mannequin to the second. Later, PIV experiments were conducted by placing the second mannequin's head with the face shield at an angle of 10°. This study aims to pose an original example for scientific research or engineering applications and designs to be carried out in this respect.

2. MATERIALS AND METHOD

The experiments were conducted in an open water channel, shown in Figure 1, in the Advanced Fluid Mechanics Laboratory at Osmaniye Korkut Ata University. The water channel includes two axial pumps with rotation control, two collecting pools, and one flow regulator in a honeycomb pattern with grids, in addition to the field of view made of plexiglass. The water tunnel was manufactured as fully sealed. The tunnel is 1.8 m high and 4 m wide with the maximum length of 15 m. The test chamber in the water tunnel is of 6 m long, with 80x80 cm of a cross-sectional top opening. The length of the channel is 80 cm, and its depth is 100 cm. A maximum of 80 cm of water can be filled. The speed ranges in the channel are between 10mm/s - 500mm/s. Prior to entering the test chamber, the flow passes through a sedimentation tank, a honeycomb, and a constriction at a ratio of 2:1. The change in the speed profile with height in the middle of the test chamber is less than 2%. The turbulence density in the middle of the test chamber at a speed of 0.3 m/s was calculated below 2%.

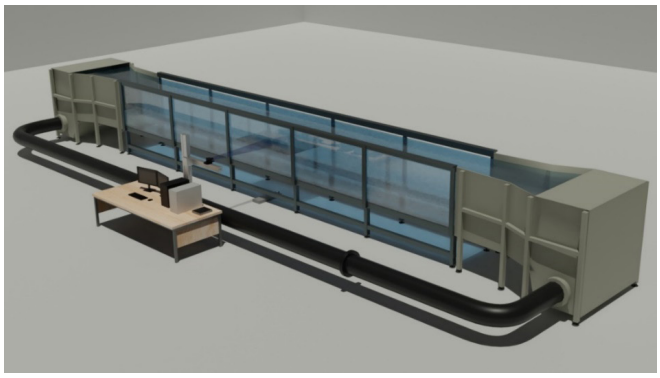

Figure 1. Technical Drawing of the Closed-circuit, Open Water Channel [31]

The study first examined the flow structure through dye experiments to have preliminary information about the structure, and to position the experimental equipment correctly. In the dye experiments, snapshots were taken with a Canon brand, EOS M50 (24MP) model digital mirrorless camera at a resolution of 1280*720 pixels in the form of 100 frames per second and of at least 66 seconds (the time corresponding to the acquisition of 1000 sets of instant data in PIV experiments), after which the images were analyzed and visuals representing the flow structure were formed for each experiment. Rhodamine 6G dye in powder form was mixed with water so that it would glow under laser light and allow detailed observation of the flow structure. A certain amount of salt was added into the dye and water mixture to obtain a solution with increased density compared to water with the aim of modelling the particles and droplets in water, which come out of the mouth while talking approximately. During the experiments, the dye was injected into the pump by designing. In this way, not only flow visualization

was achieved but also necessary information was obtained about the flow structure before PIV experiments. As a result of the dye experiments, the mannequins and the speech simulation were positioned to start the PIV experiments. Upon collecting the experimental data in the flow plane, the distorted or bad vectors were removed, with the data filtered and arranged. Images of silver coated particles used in PIV were used to calculate vector displacements. Since the particle images had random functions, the resulting correlation functions had random components with the possibility of producing slightly inaccurate measurements that needed to be removed before the data set could be used. After calculating the velocity field, the distorted vectors (less than about 3%) were removed with the CleanVec program and the field of view was scaled according to the real flow area [27]. The PIV system consists of a basic software that performs the analysis to obtain velocity vectors by providing the connection between laser, camera, synchronizer subsystems, a computer, and the system. It involves a pair of Nd:YAG laser sources, each with a power of 120 mJ, a high-resolution digital camera, laser sources and a synchronizer as well as various optical elements that enable the digital camera to work together. The digital camera can shoot 15 snapshots per second with a resolution of 1600x1186 pixels. In addition, the camera was equipped with a 50 mm f1.8 aperture lens. Spherical silver-plated particles of 20-micron diameter with a density higher than that of water were scattered into the flow so that it would collapse under the effect of gravity in still water. The measurement area was illuminated by a laser beam approximately 2 mm thick. The time interval between laser pulses was chosen as 0.066 seconds. It was concluded that the errors in velocity measurements made using the PIV technique were less than 2% [28].

The experiments involved a human head mannequin and a face shield model, which is used extensively by healthcare and community care professionals in the fight against the pandemic, in order to represent reality. Figure 2 presents a schematic representation of the mannequin head model in the flow area, and the visual of the face shield placed on the model, as well as a second mannequin where the speech simulation was performed. Figure 2-(a) represents the schematic representation of the mannequin head models placed perpendicular to the channel, whereas Figure 2-(b) shows those at an angle of 10° to the channel. We investigated the impact on the flow structure in relation to the distances between the two models positioned at two different spots as L=50 cm and L=150 cm, and the positioning of the mannequin model with the face shield placed perpendicular to the channel and at an angle of 10°. The cameras optical sensor uses Charge-Coupled Device (CCD) technology for converting light info collected from lens to digital image data. In Figure 3, there is an image of the CCD sensor camera used in the PIV study and the head mannequin with a face shield, around which the flow structure was examined. PIV studies in the literature have shown that the average flow velocity during speech can be 3.1 m/s in air [29,30]. In the study, Reynolds' Law of Similarity was used and the Reynolds number for water was found to be Re≅35500. In this direction, taking into account the studies in the literature, water containing dye and particulates was injected into the channel through an injector out of a reservoir at a constant velocity of ≅ 0.31 m/s for water and containing silver-coated particles. Figure 4 presents the image with the viewing area of the examined mannequin model.

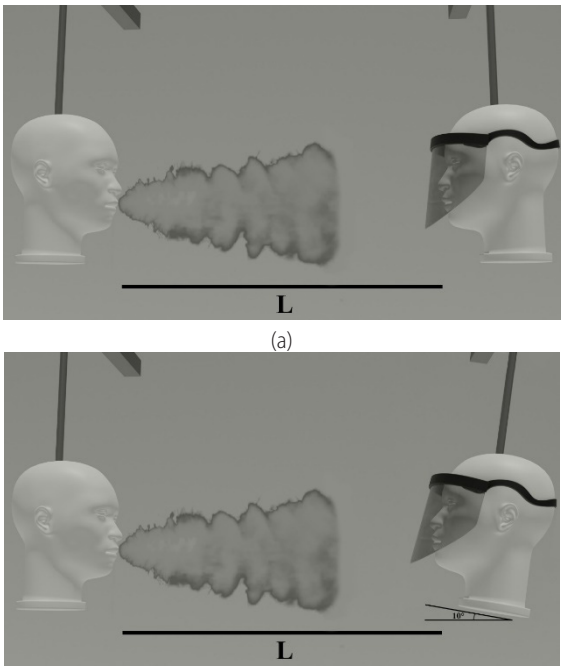

Figure 2. The image of the mannequin head models within the water channel, a) perpendicular to the channel and b) placed at an angle of 10° to the channel

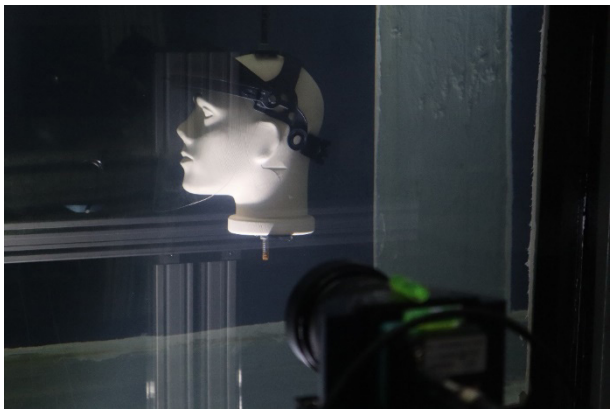

Figure 3. The image of the mannequin head model and the CCD sensor camera located in the water channel where the experiments were conducted

3. RESULTS AND DISCUSSION

Figures 4, 5 and 6 present the images of the dye experiments on the mannequin model performed using the PIV technique in the open surface water channel in the Advanced Fluid Mechanics Laboratory at Osmaniye Korkut Ata University. Snapshots were selected from among the dye experiments within a certain time interval to reach the results. Figure 5 shows how the dye was sprayed on the head model from a distance of L=50 cm without using face shield, and

the movement of the dye on the mannequin surface. It is clearly seen that the dye hitting the face directly progresses towards the mannequin's nose and eyes (t=2.320s). Figure 5 presents the images of the dye experiment conducted at certain time intervals with the dye spraying apparatus positioned at a distance of L = 50 cm for the trial where face shield was used. Since the time elapsed between the first time the dye came out of the injector and the contact with the face shield was short due to the short distance between the two objects, the dye directly hit the face shield surface (t=1.40s) and moved from the lower area of the face shield towards the neck of the mannequin (t=2.332s) after hitting. Compared to the experiment without one, the face shield directed the flow coming to the face away from the nose and eye area in the first place. However, it is seen that the flow of the dye injected at very close range (L=50cm) can be carried up from the lower surface of the face shield towards the neck, even up to the jaw. Figure 6 shows the images of the dye experiments conducted with the dye spraying apparatus positioned at L=150 cm away from the face shield. The dye sprayed from a further distance than L=50 cm (L=150 cm) seemed to lose its motion energy in the flow until it reached the face shield and moved away from the neck area (t=20s and t=24s) without creating a flow movement from the lower part of the face shield to the jaw. It is also evident that the use of PPE has a preventive effect at first contact. The study examined the flow structure through the PIV method to make a spraying process, like the act of speech, reach the face shield from different distances (L=50cm and L=150 cm) as well as determining the flow characteristics on the face shield. The highest and lowest values of velocity magnitude, which is the resultant flow velocity, on the contour were 0 m/s and 0.31 m/s, respectively, whereas the increase interval was ΔV=0.026 m/s. PIV experiments were also conducted in that speed range at different L distances and different angles.

Figures 7-11 present the snapshots obtained at different times (1/15s) as a result of the PIV experiments. The time interval is taken as 4 seconds for both frames. The mannequin inside the channel was examined when it was perpendicular (0°) and when positioned at an angle of 10° to the channel. Figure 7 shows the snapshots of the face shield surface taken flow simulation at L=50cm. The figures show the velocity vectors hitting the shield surface with high speed. Such vectors reach the neck of the mannequin model with the impact of the flow. The images for the values of t=1.866s, t=2.232s and t=2.800s represent that the flow was directed by hitting the lower tip of the face shield. In Figure 8, there are snapshots of the face shield taken flow simulation at L=150cm. It is seen that the velocity vectors that emerged as a result of the performed from a farther position compared to the L=50 cm lost their energy and weakened. Consequently, the

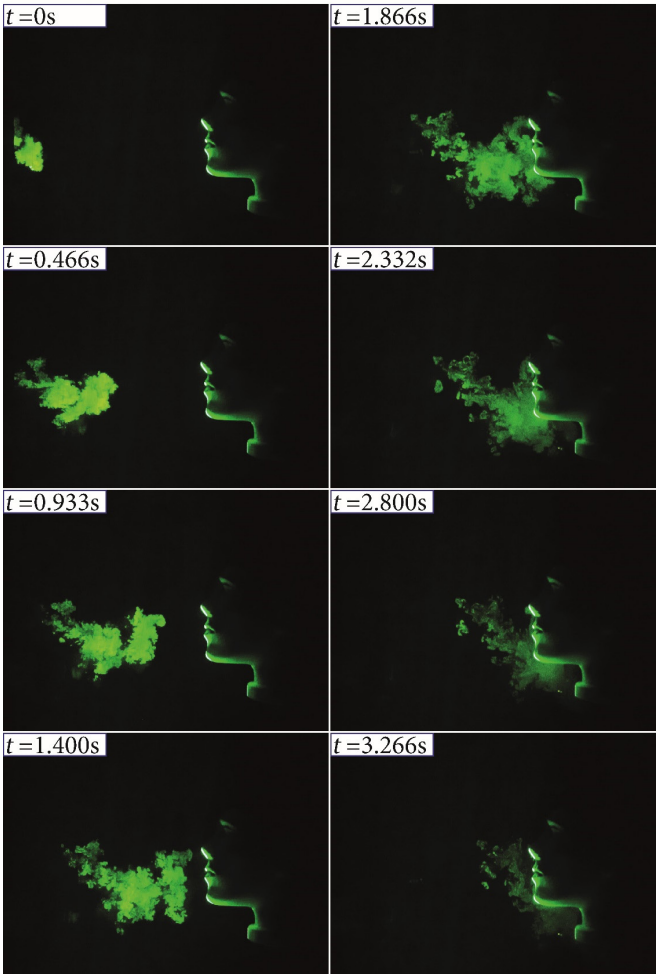

Figure 4. The snapshots of the dye experiments performed on the mannequin without a face shield at different time intervals (50cm)

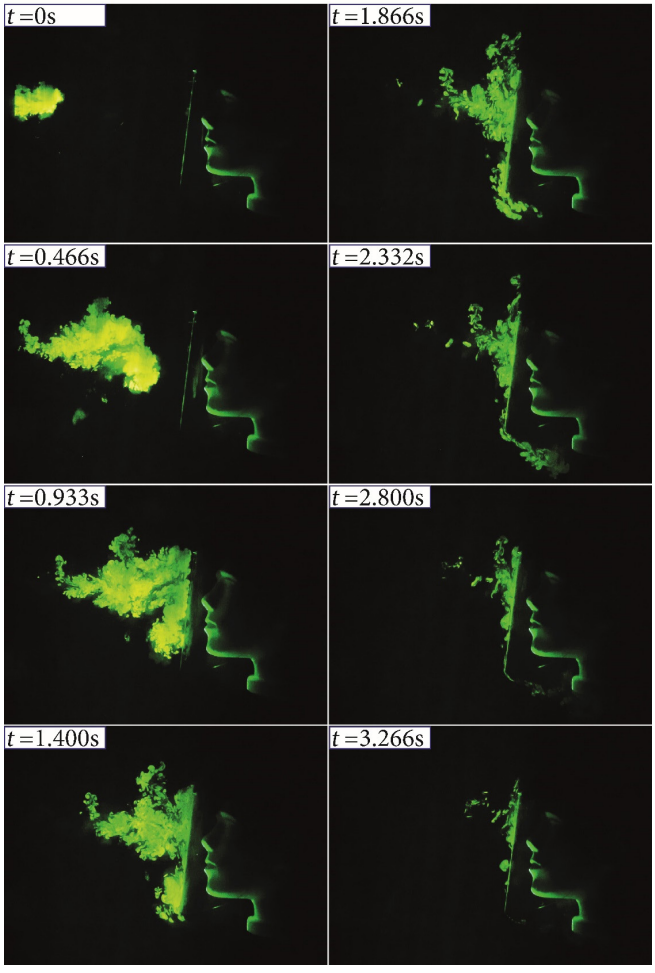

Figure 5. The snapshots of the dye experiments performed on the mannequin with a face shield at different time intervals (50cm)

doi: https://doi.org/10.26701/ems.907162

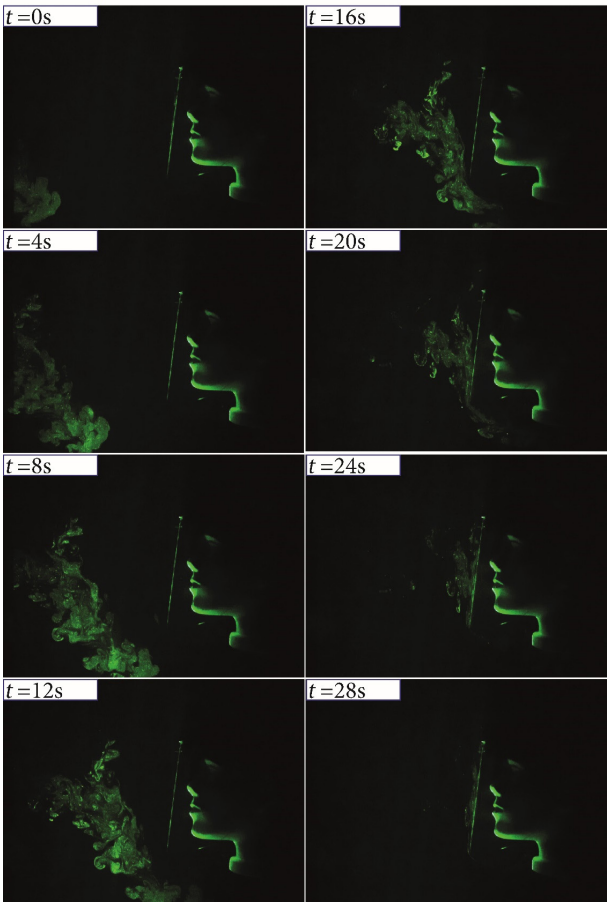

Figure 6. The snapshots of the dye experiments performed on the mannequin with a face shield at different time intervals (150cm)

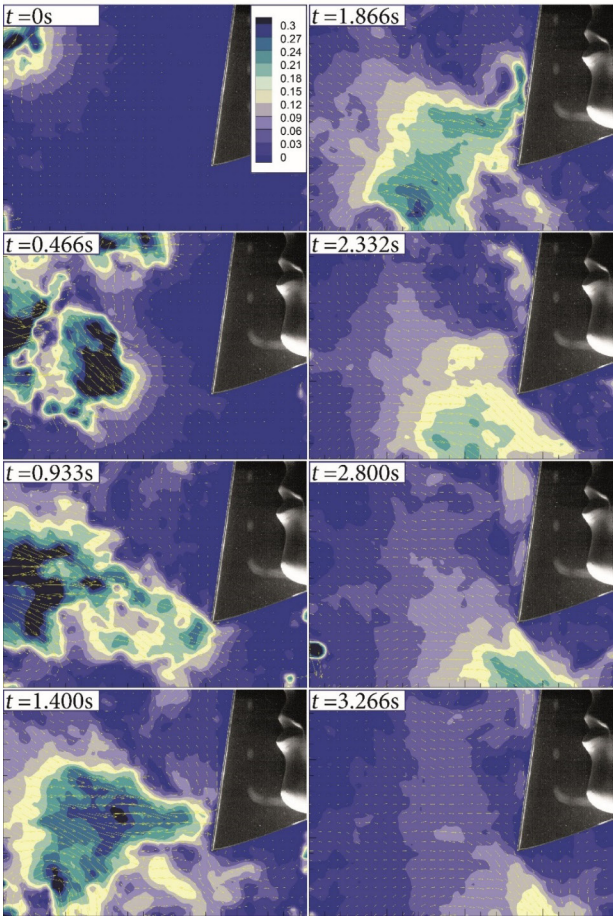

Figure 7. Snapshots of velocity vectors for the case where the mannequin is at an angle of 0° from a distance of L= 50 cm

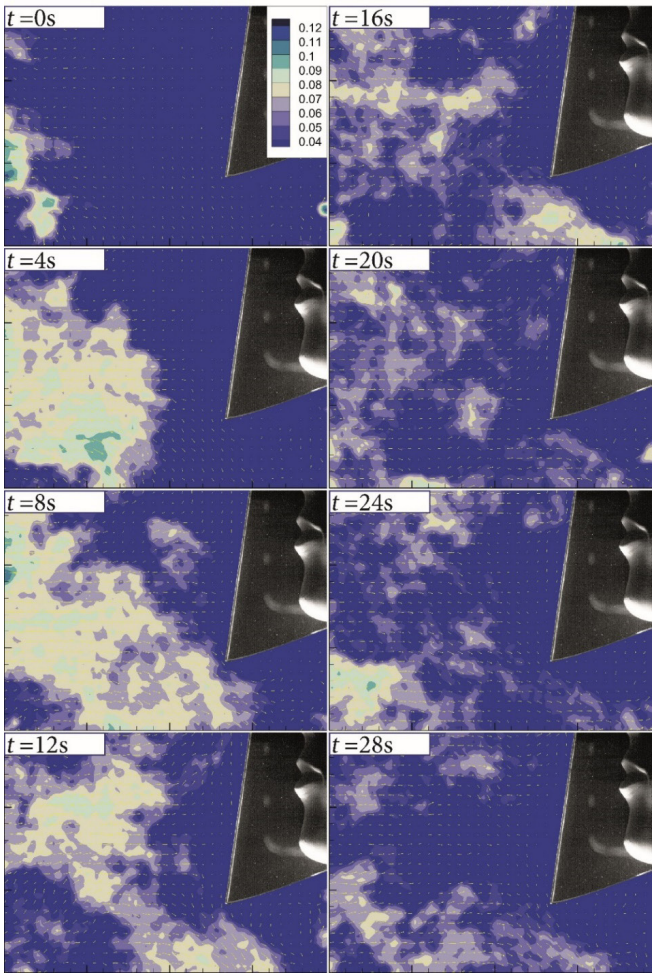

Figure 8. Snapshots of velocity vectors for the case where the mannequin is at an angle of 0° from a distance of L = 150 cm

velocity vectors coming to the surface of the mannequin moved away from the neck without reaching the face and jaw with the impact of the face shield. It will be seen more clearly when the snapshots taken at t=8,12 and 16 seconds are examined.

Figure 9 displays the snapshots of the face shield surface taken flow simulation by positioning the mannequin at L=50cm and at an angle of 10°. It did not take long for the fluid injected into the channel from the position of L=50 cm to reach the face shield as the two mannequins were close to each other, which preserved the energy emanating from the flow source and hit the shield surface intensely. Especially, the snapshots taken at t=1.866s and t=2.232s indicate that a vortex was formed due to the vectors hitting the shield surface at an angle of 10° and the resulting vortex was in an orientation from the lower part of the shield to the jaw. Figure 10 presents the snapshots of the face mannequin positioned at L=150cm away and an angle of 10° to the flow. The fact that the time elapsed between the point where the flow simulation originated from the source and the point where it touched the face shield due to the distance caused the vectors to lose their energy. Although the vectors had a low velocity, they moved from the lower tip of the face shield to the jaw, especially between t=16s and t=28s, due to the 10° angle of the shield. In t=20s, in particular, it is more clearly

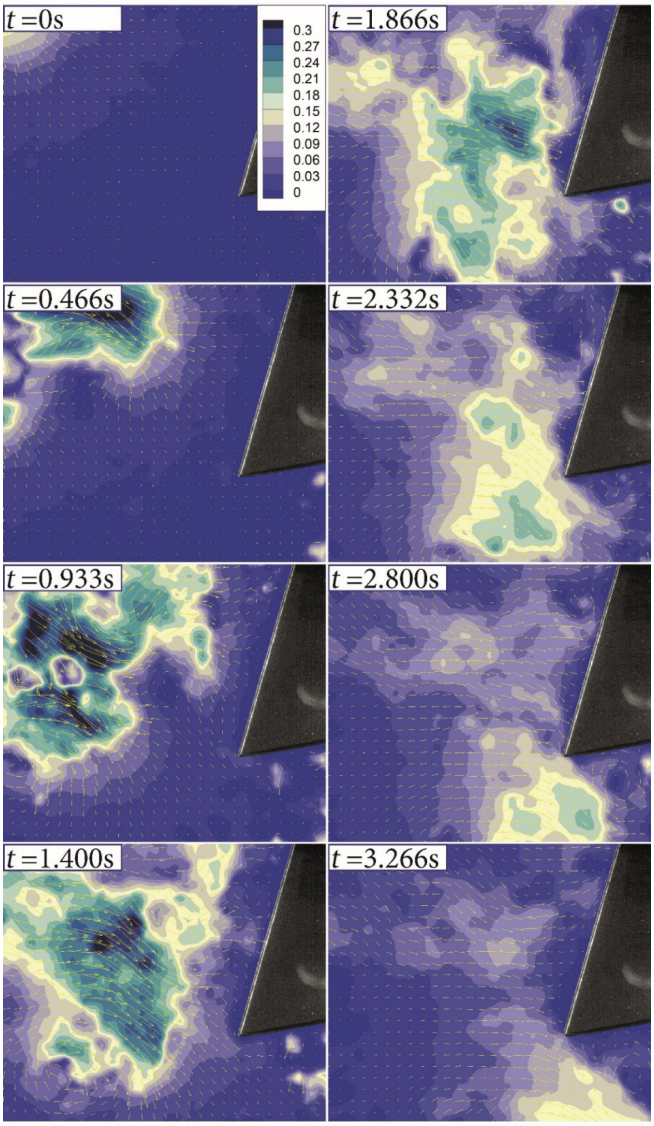

Figure 9. Snapshots of velocity vectors for the case where the mannequin is at an angle of 10° from a distance of L = 50 cm

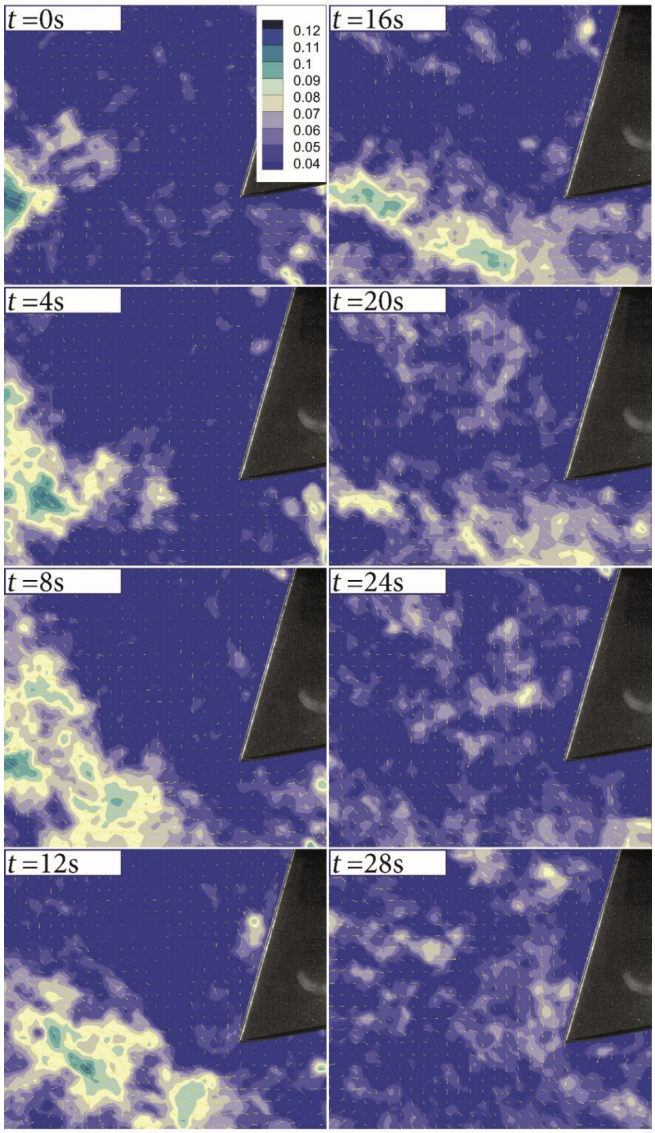

Figure 10. Snapshots of velocity vectors for the case where the mannequin is at an angle of 10° from a distance of L = 150 cm

seen that the velocity vectors were directed towards the jaw with the effect of the angle. Figures 11 and 12 contain Velocity Magnitude / Time graphs at the positions of L=50cm-0° and L=150cm-0°, respectively. Time-dependent velocity change graphs were formed by putting points at different positions in the Y axis and the X axis in the field of view. X_1 was created with the data obtained from the coordinates of Y=60-X= 40, X_2 from the coordinates of Y=60-X=80, and X_3 from those of Y=60-X=120. Figure 11 and Figure 12 show that the vectors emerging from the source located L=50cm away reach the face shield in a short time, while in a longer time when located L=150 cm away. The velocity data got dimensionless with dividing the velocity magnitude by source velocity. The graphs also indicate that the velocity of the vectors from L=50cm away is approximately 10 times higher than that from L=150cm away. In addition, the velocity of the vectors seems to decrease as a result of their movement towards the shield in the X axis over time. The flow loses its velocity as it moves away from the outlet source, and the X_1 point close to the source has higher values than those acquired from the time-dependent velocity data taken from

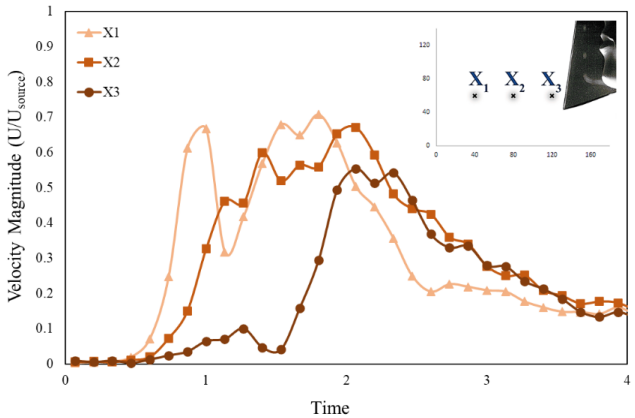

Figure 11. Time-dependent dimensionless velocity profiles taken from the positions X = 40 mm, X = 80 mm and X = 120 mm in the flow direction from the fixed Y axis at a distance of L = 50 cm

the X_2 and X_3 points in both graphs. It is apparent how important the distance is between people and the way of using personal protective equipment with respect to the risk of direct exposure to infective droplets at first glance. However,

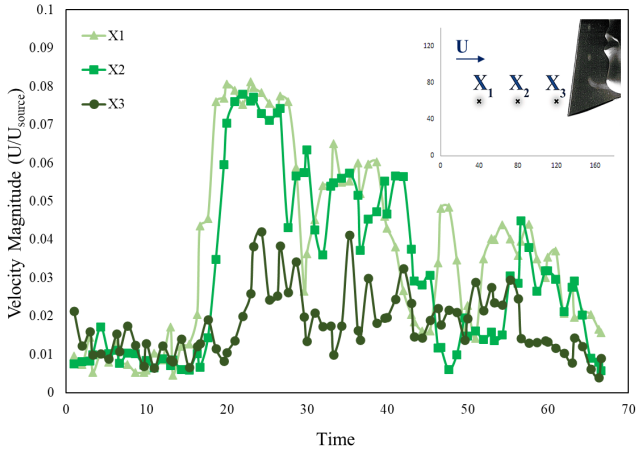

Figure 12. Time-dependent dimensionless velocity profiles taken from the positions X = 40 mm, X = 80 mm and X = 120 mm in the flow direction from the fixed Y axis at a distance of L = 150 cm

it should be known that using PPE alone will not be enough. In this study, the flow structure around PPE exposed to a flow is examined.

4. CONCLUSIONS

The study conducted dye experiments and used the particle imaging velocity measurement (PIV) technique to determine the flow characteristics of the action of flow simulated from different distances (L=50 cm and L=150 cm) placed in a channel in relation to the face shield positioned at different angles (10° and 0°). In the results of study;

- In the experiment in which no face shields were used, the dye hitting the face directly moved towards the nose and eyes of the mannequin, whereas in the next experiment with a face shield, the shield caused to change direction of the flow in the first place and protected it away from the face and eyes.
- The experiment performed at a close distance (L=50 cm 0°) revealed that the face shield protected the face and eye area of the mannequin compared to the model without the face shield, but the flow was directed towards the neck region due to the energy of flow. The result of the experiment performed from a longer distance (L=150 cm) demonstrated that the flow lost most of its energy as it approached the face shield and the flow hitting the shield surface moved away from the neck area without being directed to the jaw area.
- It was observed that the face shield prevented the contact of the vectors released at different speeds to the mannequin skins in the first place. However, the flow sent from L=50 cm and L=150 cm away from the face shield positioned at an angle of 10° was directed towards the jaw area due to the vortex formed in the lower part of the shield.

As a result of this work, it has been shown that the risk of direct exposure to velocity vectors (infective droplets) at first glance, the distance between people as well as the way of using the personal protective equipment and their characteristics are of great importance for health. Additionally, this study has shown that exposure to the air flow released as a result of speech at a close distance is a health risk even if protective equipment is used, and the distance between people should be maintained under all conditions.

The study of the flow characteristic on the face shield, which is a personal protective equipment, aimed to reveal the conditions of the object under the flow. From the results obtained, it is clearly seen that protection is insufficient in face shields so long as jaw, upper forehead and side gaps are not covered since the face shields appear to be very sensitive to the up/down movement of the head. It is recommended that a surgical mask should be used together with a face shield against the possibility of particles entering the respiratory tract from the gaps on the sides and under the jaw especially in such types of face shields.

ACKNOWLEDGEMENT

We would like to express our deepest regards and thanks to the healthcare professionals in Turkey and all around the world, who work very hard in these difficult times.

We are also very grateful to the reviewers for their valuable comments, which have been utilized to improve the quality of the paper.

REFERENCES

[1] Correia, G., Rodrigues L., Gameiro da Silva, M., Gonçalves, T. (2020). Airborne route and bad use of ventilation systems as non-negligible factors in SARS-CoV-2 transmission. Med Hypotheses; 141:109781. https://doi.org/10.1016/j.mehy.2020.109781.

[2] Segredo-Otero, E., Sanjuán, R. (2019). The effect of genetic complementation on the fitness and diversity of viruses spreading as collective infectious units. Virus Res; 267:41–8. https://doi.org/10.1016/j.virusres.2019.05.005.

[3] Pan, M., Lednicky, J.A., Wu, C.Y. (2019). Collection, particle sizing and detection of airborne viruses. J Appl Microbiol; 127:1596–611. https://doi.org/10.1111/jam.14278.

[4] Chen, C., Lin, C.H., Jiang, Z., Chen, Q. (2014). Simplified models for exhaled airflow from a cough with the mouth covered. Indoor Air, 24:580–91. https://doi.org/10.1111/ina.12109.

[5] Wang, J., Chow, T.T. (2011) Numerical investigation of influence of human walking on dispersion and deposition of expiratory droplets in airborne infection isolation room. Build Environ; 46:1993–2002. https://doi.org/10.1016/j.buildenv.2011.04.008.

[6] Li, X., Inthavong, K., Tu, J. (2012). Particle inhalation and deposition in a human nasal cavity from the external surrounding environment. Build Environ; 47:32–9. https://doi.org/10.1016/j.buildenv.2011.04.032.

[7] Nishimura, H., Sakata, S., Kaga, A. (2013). A new methodology for studying dynamics of aerosol particles in sneeze and cough using a digital high-vision, high-speed video system and vector analyses. PLoS One; 8. https://doi.org/10.1371/journal.pone.0080244.

[8] Tang, J. W., Noakes, C. J., Nielsen, P. V., Eames, I., Nicolle, A., Li, Y., & Settles, G. S. (2011). Observing and quantifying airflows in the infection control of aerosol-and airborne-transmitted diseases: an over-

view of approaches. Journal of Hospital Infection, 77(3), 213-222.

[9] Berlanga FA, de Adana MR, Olmedo I, Villafruela JM, San José JF, Castro F. (2018). Experimental evaluation of thermal comfort, ventilation performance indices and exposure to airborne contaminant in an airborne infection isolation room equipped with a displacement air distribution system. Energy Build; 158:209–21. https://doi.org/10.1016/j.enbuild.2017.09.100.

[10] Thierry, B., Célérier, C., Simon, F., Lacroix, C., Khonsari, R.H. (2020). How and why use the EasyBreath® Decathlon surface snorkeling mask as a personal protective equipment during the COVID-19 pandemic? Eur Ann Otorhinolaryngol Head Neck Dis: 5–7. https://doi.org/10.1016/j.anorl.2020.05.006.

[11] King, M.F., Noakes, C.J., Sleigh, P.A. (2015) Modeling environmental contamination in hospital single- and four-bed rooms. Indoor Air; 25:694–707. https://doi.org/10.1111/ina.12186.

[12] Vordos, N., Gkika, D.A., Maliaris, G., Tilkeridis, K.E., Antoniou, A., Bandekas, D. V., et al. (2020) How 3D printing and social media tackles the PPE shortage during Covid – 19 pandemic. Saf Sci;1 30:104870. https://doi.org/10.1016/j.ssci.2020.104870.

[13] Vuorinen, V., Aarnio, M., Alava, M., Alopaeus, V., Atanasova, N., Auvinen, M., et al. (2020) Modelling aerosol transport and virus exposure with numerical simulations in relation to SARS-CoV-2 transmission by inhalation indoors. Saf Sci; 130:104866. https://doi.org/10.1016/j.ssci.2020.104866.

[14] Davis, P.J., Spady, D., Forgie, SED. (2007) A survey of Alberta physicians' use of and attitudes toward face masks and face shields in the operating room setting. Am J Infect Control; 35:455–9. https://doi.org/10.1016/j.ajic.2006.08.011.

[15] Boškoski, I., Gallo, C., Wallace, M. B., & Costamagna, G. (2020). COVID-19 pandemic and personal protective equipment shortage: protective efficacy comparing masks and scientific methods for respirator reuse. Gastrointestinal endoscopy, 92(3), 519-523.

[16] Sapoval, M., Gaultier, A. L., Del Giudice, C., Pellerin, O., Kassis-Chikhani, N., Lemarteleur, V., ... & Attal, J. P. (2020). 3D-printed face protective shield in interventional radiology: Evaluation of an immediate solution in the era of COVID-19 pandemic. Diagnostic and interventional imaging, 101(6), 413-415.

[17] Shokrani, A., Loukaides, E.G., Elias, E., Lunt, A.J.G. (2020). Exploration of alternative supply chains and distributed manufacturing in response to COVID-19; a case study of medical face shields. Mater Des, 192:108749. https://doi.org/10.1016/j.matdes.2020.108749.

[18] Skamnelos, A., Murino, A., Lazaridis, N., Cunado, L., & Despott, E. J. (2020). Endoscopy during the COVID-19 pandemic: simple construction of a single-use, disposable face shield using inexpensive and readily available materials. VideoGIE, 5(9), 399-401.

[19] Zhou, Q., Qian, H., Ren, H., Li, Y., & Nielsen, P. V. (2017). The lock-up phenomenon of exhaled flow in a stable thermally-stratified indoor environment. Building and Environment, 116, 246-256.

[20] Dbouk, T., & Drikakis, D. (2020). On coughing and airborne droplet transmission to humans. Physics of Fluids, 32(5), 053310.

[21] Licina, D., Pantelic, J., Melikov, A., Sekhar, C., & Tham, K. W. (2014). Experimental investigation of the human convective boundary layer in a quiescent indoor environment. Building and Environment, 75, 79-91.

[22] Badeau, A., Afshari, A., Goldsmith, T., Frazer, D. (2002) Preliminary prediction of flow and particulate concentration produced from normal human cough dispersion. Annu Int Conf IEEE Eng Med Biol - Proc; 1:246–7. https://doi.org/10.1109/iembs.2002.1134475.

[23] Ge, Q., Li, X., Inthavong, K., Tu, J. (2013). Numerical study of the effects of human body heat on particle transport and inhalation in indoor environment. Build Environ, 59:1–9. https://doi.org/10.1016/j.buildenv.2012.08.002.

[24] Richmond-Bryant, J. (2009). Transport of exhaled particulate matter in airborne infection isolation rooms. Build Environ, 44:44–55. https://doi.org/10.1016/j.buildenv.2008.01.009.

[25] Tang, J.W., Nicolle, A.D., Klettner, C.A., Pantelic, J., Wang, L., Suhaimi, A. Bin, et al. (2013). Airflow Dynamics of Human Jets: Sneezing and Breathing - Potential Sources of Infectious Aerosols. PLoS One; 8:1–7. https://doi.org/10.1371/journal.pone.0059970.

[26] Clark, R. P., & de Calcina-Goff, M. L. (2009). Some aspects of the airborne transmission of infection. Journal of the Royal Society Interface, 6(suppl_6), S767-S782.

[27] Ozalp, C., Pinarbasi, A. H. M. E. T., & Sahin, B. (2010). Experimental measurement of flow past cavities of different shapes. Experimental Thermal and Fluid Science, 34(5), 505-515. https://doi.org/10.1016/j.expthermflusci.2009.11.003.

[28] Alnak, D.E., Varol, Y., Firat, M., Oztop, H.F., Ozalp, C. (2019). Experimental and numerical investigation of impinged water jet effects on heated cylinders for convective heat transfer. Int J Therm Sci; 135:493–508. https://doi.org/10.1016/j.ijthermalsci.2018.09.037.

[29] Gupta, J.K., Lin, C.H., Chen, Q. (2010). Characterizing exhaled airflow from breathing and talking. Indoor Air, 20:31–9. https://doi.org/10.1111/j.1600-0668.2009.00623.x.

[30] Chao, C. Y. H., Wan, M. P., Morawska, L., Johnson, G. R., Ristovski, Z. D., Hargreaves, M., ... & Katoshevski, D. (2009). Characterization of expiration air jets and droplet size distributions immediately at the mouth opening. Journal of aerosol science, 40(2), 122-133.

[31] Özalp, C., Polat, C., Saydam, D., Söyler, M. (2020). Dye Injection Flow Visualization Around a Rotating Circular Cylinder . European Mechanical Science , 4 (4) , 185-189 . doi: https://doi.org/10.26701/ems.794683

EUROPEAN MECHANICAL SCIENCE
e-ISSN: 2587-1110

Research Paper

Some New Approximate Solutions in Closed-Form to Problems of Nanobars

Ugurcan Eroglu[1*]

[1]Izmir University of Economics, Faculty of Engineering, Department of Mechanical Engineering, İzmir, Turkey

Abstract

Following recent technological advancements, a great attention has been paid to the mechanical behaviour of structural elements of nanosize. In this study, some solutions to mechanical problems of bars of nanosize are examined using Eringen's two-phase nonlocal elasticity. Assuming the fraction coefficient of nonlocal part of the material is small, a perturbation expansion with respect to it is performed. With this procedure, the original nonlocal problem is broken into a set of local elasticity problems. Solutions to some example problems of nanobars are provided in closed-form for the first time, and commented on. The new solutions provided herein may well serve for benchmark studies, as well as identification of material parameters of nano-sized structural elements, such as carbon nanotubes.

Keywords: Nanobars; nonlocal elasticity; nanomechanics; closed-form solutions; approximate methods.

1. INTRODUCTION

Rational theories on deformable solids stemmed from the corpuscular models, by which the internal structure of the material was accounted for [1-3]. Oversimplifying the relations between the atoms gave rise to conclusions which were inconsistent with experimental results; about the same time continuum models of solids were proposed and widely accepted. Interested readers are kindly referred to [4] for more detailed information about the evolution of continuum models, and the roots of molecular dynamic analysis.

Cauchy's continuum model is a great approximation to the actual physics of the matter, for most of the engineering materials. However, when the smallest internal organization constituing the material has comparable dimensions with respect to the overall size of the structure; or when the waves of frequency of interest are dispersed due to constituent of the material, more enhanced theories are required to reflect better the behavior of the material [5-10]. For this purpose one may resort to methods which use a model of the smallest unit of the internal structure of the material: molecular dynamic simulations at atomic scale [11], or limit analysis for masonry walls, for example [12]. Being accurate, these models are quite time consuming due to discrete modelling of a very high number of degrees of freedom [4]. As a good alternative, continuum models which account for the characteristics of the internal material organization have been developed, which are called nonlocal continuum theories. These theories either introduces additional kinematic descriptors to those of classical theory of elasticity (classified as "implicit") or assumes a convolution-type constitutive equation, cancelling the axiom of locality (classified "explicit") [13-14]. Possible equivalencies and distinctions between these two classes are recently studied in [15-16].

As one of the simplest, yet, most widely used structural elements, bars are the interest of this study. Herein, bars of nanosize will be examined utilizing Eringen's nonlocal theory of elasticity. In the literature, there is a vast amount of studies dealing with similar problems; yet most of them resort to numerical resolutions of the differential equations; see, for example, [17]. This is obviously for a good reason: the governing equations of nanobars are of integro-differential type, the existence and uniqueness of which requires a great deal of examination. Indeed, the exact solution in [18] was only provided for some special loading and boundary conditions, which satisfy some additional and non-physical conditions, called *constitutive boundary conditions*. Such an additional requirement for an exact solution to exist (albeit in a certain form) induced a debate among the researchers which still continues, and it even led to some strong conclusions indicating the use of strain-driven non-local models must be prevented [18]. The intention here is to stay out of this discussion, and to look for the possibilities of finding approximate solutions to the problems of bars of nanosize, by using a perturbation technique which is recently proposed

* Corresponding author
Email: ugurcan.eroglu@izmirekonomi.edu.tr

European Mechanical Science (2021), 5(4): 161-167
doi: https://doi.org/10.26701/ems.773106
Received: July 24, 2020
Accepted: July 26, 2021

by this author [20], and extending the example problems considered therein.

In addition to those landmark studies cited in up to this point, the interested readers are kindly referred to [21, 22] for relatively recent applications of Eringen's two-phase model, [23-27] for different approaches to the modelling of nanobars, and a review paper [28] for a better insight on classification, limitations, and mathematical aspects of nonlocal continuum models.

The novel points of the present study are the following: different example problems are examined by using the method proposed in [20], the solutions to them are given in closed-form, quantitative comparison of the results with the literature are provided for further verification of the method, and the convergence of the results are examined. Some benchmark results are provided which can be used for verification purposes of new numerical or analytical techniques to be presented in the future for this very hot topic of solid mechanics.

2. MECHANICS OF NANOBARS

Eringen's nonlocal theory of elasticity is based on the axioms of causality, determinism, equipresence, objectivity, material invariance, neighbourhood, memory, and admissibility. The axiom of locality, which basically leads to the local theory of elasticity, is skipped; and as a result, the stress at a point depends on the strain multiplied by an attenuation function and integrated over the entire domain which consists of material points. Note that this theory keeps the primal fields of local elasticity, but the relation between them is, in the end, qualitatively different. Examinations of structures with finite dimensions provided that there seems to be the need for additional conditions, so-called constitutive boundary conditions, for an exact solution to exist in a certain (differential) form or for the reduction of integro-differential equations to differential equations [29, 30]. Here such requirements will not be looked for; instead, an approximate solution to the integro-differential equation will be pursued.

Consider a bar of length L, along the axis x. The displacement of each point inside the bar will be denoted with u, and the resultant of stress normal to the cross-sections is N. The kinematic relation and balance requirement are independent of its constitution under the assumption of vanishing of nonlocal residuals [10]; therefore,

$$\frac{dN}{dx}=-q(x),\ \varepsilon=\frac{du}{dx} \tag{1}$$

where q is the external distributed load along the axis of the bar, and ε the normal strain along the bar axis and it is the only non-vanishing strain component in case of normal external loads. The constitutive equation of Eringen's two-phase local/nonlocal mixture law is

$$N(x)=B\left[(1-\xi)\varepsilon(x)+\xi\int_0^L K(x,X)\varepsilon(X)dX\right] \tag{2}$$

where B is axial rigidity of the bar, ξ is the mixture parameter denoting the weight of the nonlocal part, and $K(x,X)$ is the attenuation function which represents the interaction between the points depending on the distance between them. Among many alternatives, the exponential kernel is utilized herein:

$$K(x,X)=\frac{1}{2\kappa}\exp\left(\frac{|x-X|}{\kappa}\right) \tag{3}$$

where κ is nonlocal parameter quantifying the zone of interaction between material points. The coefficient of the exponential part stems from the usual normalization of kernel function over infinite domain.

3. SOLUTION PROCEDURE

Formal series expansions of normal force field, N, and axial strain, ε, and axial displacement, u, about a certain value η_0 of a generic parameter η, are as follows.

$$\begin{aligned}
N\approx N^n&=\sum_{j=0}^{n}\frac{(\eta-\eta_0)^j}{j!}\frac{d^jN}{d\eta^j}\bigg|_{\eta=\eta_0}=\sum_{j=0}^{n}\frac{(\eta-\eta_0)^j}{j!}N_j(\eta_0)\\
\varepsilon\approx\varepsilon^n&=\sum_{j=0}^{n}\frac{(\eta-\eta_0)^j}{j!}\frac{d^j\varepsilon}{d\eta^j}\bigg|_{\eta=\eta_0}=\sum_{j=0}^{n}\frac{(\eta-\eta_0)^j}{j!}\varepsilon_j(\eta_0)\\
u\approx u^n&=\sum_{j=0}^{n}\frac{(\eta-\eta_0)^j}{j!}\frac{d^ju}{d\eta^j}\bigg|_{\eta=\eta_0}=\sum_{j=0}^{n}\frac{(\eta-\eta_0)^j}{j!}u_j(\eta_0)
\end{aligned} \tag{4}$$

Admitting $\eta=\xi$ and $\xi_0=0$ provide,

$$\{N,\varepsilon,u\}\approx\{N^n,\varepsilon^n,u^n\}=\sum_{j=0}^{n}\frac{\xi^j}{j!}\frac{d^j\{N,\varepsilon,u\}}{d\xi^j}\bigg|_{\xi=0}=\sum_{j=0}^{n}\frac{\xi^j}{j!}\{N_j,\varepsilon_j,u_j\} \tag{5}$$

where N_j, ε_j, and u_j are j^{th} derivatives of normal force, axial strain, and axial displacement fields evaluated for ξ = 0.

Inserting Eq. (5) into first of Eq. (1), and Eq. (2) provides,

$$\begin{aligned}
&0^{th}\text{ order:}\quad \frac{dN_0}{dx}=-q(x),\qquad \varepsilon_0=\frac{N_0}{B},\qquad \frac{du_0}{dx}=\varepsilon_0.\\
&j^{th}\text{ order:}\quad \frac{dN_j}{dx}=0,\qquad \varepsilon_j=\frac{N_j}{B}-j\left(K*\varepsilon_{j-1}-\varepsilon_{j-1}\right),\qquad \frac{du_j}{dx}=\varepsilon_j.
\end{aligned} \tag{6}$$

where the convolution between kernel function and any generic function, f, is described as below.

$$K*f=\int_0^L K(x,X)f(X)dX \tag{7}$$

This procedure stipulates the nonhomogeneous part to depend on the evolution parameter, providing the dependence of inner actions on stiffness due to the requirement of compatibility equations. Here it is important to note that in case of statically determinate structures, there is no such dependence.

The axial force field and axial displacement field of different orders may be obtained by integration.

$$N_0(x)=N_0(0)-\int_0^x q(\Xi)d\Xi,\quad u_0(x)=u_0(0)+\int_0^x \varepsilon_0(\Xi)d\Xi.$$

$$N_j(x)=N_j(0),\quad u_j(x)=u_j(0)+\int_0^x \varepsilon_j(\Xi)d\Xi. \tag{8}$$

where $N_i(0)$ and $u_i(0)$ $(i=0,1,2,...)$ are initial values of normal force and axial displacement, to be obtained by imposing only the physical boundary conditions.

4. EXAMPLE PROBLEMS

Some example problems of bars of nano-size with this method have been presented in [20]. Here we will skip those basic examples, and focus on statically indeterminate problems and bars of variable section. Convergence of all examples will be looked for numerically.

4.1. Doubly-fixed uniform bar under uniform distributed load

This is an important example to show numerically the possible convergence of the solution technique for statically indeterminate problems. Boundary conditions are,

$$u(0)=u(L)=0 \tag{9}$$

which, with the formal series expansion, becomes,

$$u_i(0)=u_i(L)=0,\quad i=0,1,2,...,n \tag{10}$$

In the case of uniform distributed load,

$$q(x)=q_0 \Rightarrow N_0=N_0(0)-q_0x$$
$$\frac{du_0}{dx}=\frac{N_0(0)-q_0x}{B}\Rightarrow u_0=u_0(0)+\frac{N_0(0)}{B}x-\frac{q_0x^2}{2B} \tag{11}$$

Applying the boundary conditions, $u(0)=0, u(L)=0$ provide,

$$N_0=\frac{1}{2}q_0(L-2x),\quad u_0=\frac{q_0L}{2B}x-\frac{q_0x^2}{2B} \tag{12}$$

which are very well-known solutions of local elasticity.

Using the 0^{th}-order solutions, and boundary conditions of each order, the normal force field of higher-order turns out to be identical to zero. Higher-order displacement fields are obtained as below.

$$u_1=\frac{\left(1-e^{x/\kappa}\right)e^{-\frac{L+z}{\kappa}}\left(e^{z/\kappa}-e^{L/\kappa}\right)(2\kappa+L)\kappa q_0}{4B} \tag{13}$$

$$u_2=\frac{q_0e^{\frac{x-2L}{\kappa}}}{B}\left(e^{L/\kappa}\left(-\frac{\kappa^2}{4}+\frac{L^2}{4}+\kappa\left(\frac{3L}{8}-\frac{x}{2}\right)-\frac{Lx}{4}\right)+\kappa\left(\frac{\kappa}{4}+\frac{L}{8}\right)\right)+\frac{q_0\kappa e^{-\frac{L+x}{\kappa}}}{B}\left(\frac{\kappa}{4}+\frac{L}{8}\right)$$
$$+\frac{q_0\kappa}{B}\left(1-e^{-2L/\kappa}-2\frac{L}{\kappa}e^{-L/\kappa}\right)\left(\frac{\kappa}{4}+\frac{L}{8}\right)+\frac{q_0e^{\frac{L}{\kappa}}e^{\frac{L+x}{\kappa}}}{B}\left(-\frac{\kappa^2}{4}+\kappa\left(\frac{x}{2}-\frac{L}{8}\right)+\frac{Lx}{4}\right) \tag{14}$$

$$u_3=\frac{q_0e^{\frac{2L}{\kappa}}\left(-\frac{3\kappa^2}{8}+\frac{3L^2}{8}+\frac{9\kappa L}{16}\right)}{B}+\frac{q_0e^{\frac{L}{\kappa}}}{B}\left(-\frac{3\kappa^2}{16}+\frac{3L^3}{16\kappa}-\frac{3L^2}{16}-\frac{39\kappa L}{32}\right)$$
$$+\frac{q_0e^{L/\kappa}}{B}\left[e^{-\frac{2L+x}{\kappa}}\left(\frac{9\kappa^2}{16}-\frac{3L^2}{16}+\kappa\left(-\frac{3L}{32}-\frac{3x}{8}\right)-\frac{3Lx}{16}\right)\right.$$
$$\left.+e^{\frac{x-3L}{\kappa}}\left(\frac{9\kappa^2}{16}-\frac{3L^2}{8}+\kappa\left(\frac{3x}{8}-\frac{15L}{32}\right)+\frac{3Lx}{16}\right)\right]+\frac{3q_0\kappa}{16B}\left(2+e^{-\frac{3L}{\kappa}}-e^{\frac{x-3L}{\kappa}}-e^{-\frac{2L+x}{\kappa}}\right)\left(\kappa+\frac{L}{2}\right)$$
$$+\frac{q_0e^{\frac{2L}{\kappa}}}{B}\left[e^{\frac{x-3L}{\kappa}}\left(-\frac{3\kappa^2}{8}+\frac{3L^2}{8}-\frac{3L^3}{16\kappa}+\frac{3L^2x}{8\kappa}-\frac{3Lx^2}{16\kappa}+\kappa\left(\frac{21L}{16}-\frac{3x}{2}\right)-\frac{3x^2}{8}\right)\right. \tag{15}$$
$$\left.+e^{-\frac{2L+x}{\kappa}}\left(-\frac{3\kappa^2}{8}-\frac{3Lx^2}{16\kappa}+\kappa\left(\frac{3x}{2}-\frac{3L}{16}\right)+\frac{3Lx}{4}-\frac{3x^2}{8}\right)\right]$$

To look for the (weak) convergence, L_2-norm of the balance residual, R^m, will be utilized.

$$R^m=\frac{d}{dx}\left[(1-\xi)\frac{du^m}{dx}+\xi K*\frac{du^m}{dx}\right]+q_0 \tag{16}$$

Fig. 1 shows the variation of the residual of balance equation for different orders of approximate displacement fields, nonlocal parameter, and fraction coefficient. As expected, they are null for the full local model, designated with $\boldsymbol{\xi} = 0$, and tend to grow as the fraction coefficient increases. This is, again, expected since the approximation is made on the value of the fraction coefficient; hence, increasing values of it simply requires the consideration of more terms in the series expansion. A similar outcome is reported in [20], but in the absence of distributed load and for statically determinate problems of nanobars.

Fig.2 provides the visual representation of Eqs. $(12)_2$, (13), (14), and (15). Higher-order functions of displacement grow with increasing nonlocal parameter which gives us a hint on a possible limit for $\boldsymbol{\kappa}$ when looking for formal proof of convergence of the method. Note that these functions are to be modulated with the fraction coefficient when obtaining the final displacement field, see Eq. (5). The increasing effect of nonlocality close to boundaries become more visible as the order of function increases.

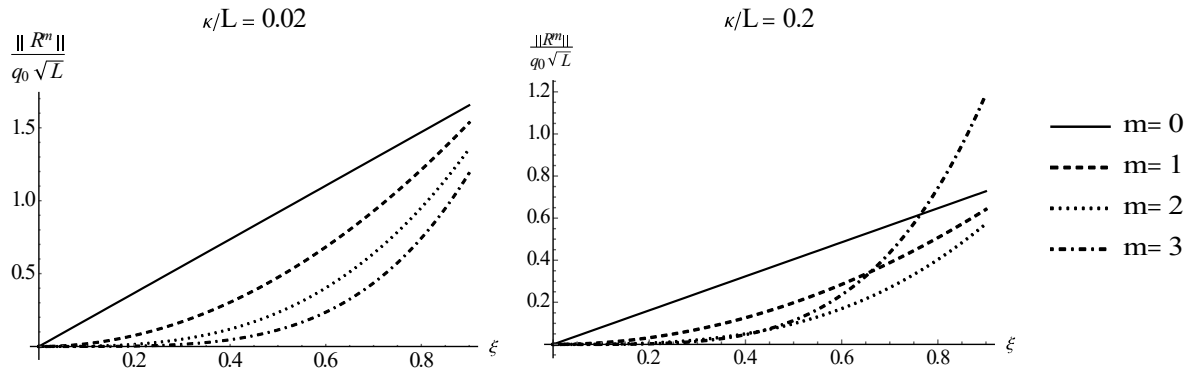

Figure 1. L_2-norm of balance residual for different orders of approximation

doi: https://doi.org/10.26701/ems.773106

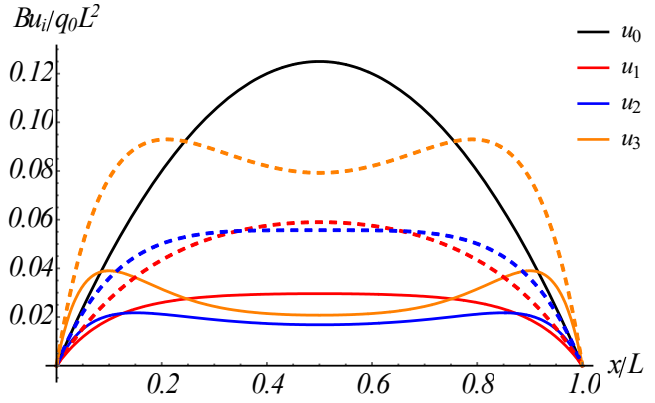

Figure 2. Variations of displacement functions of different orders. Solid lines: **κ**/*L* = 0.1, Dashed lines. **κ**/*L* = 0.2

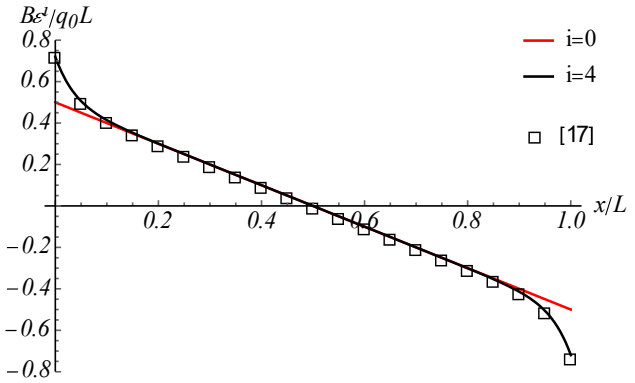

Figure 3. Variation of strain along doubly-fixed bar under uniform distributed load. **ξ** = 0.5, **κ**/*L* = 0.05

A similar problem is considered in [17], where a numerical technique with considerable computational expense is utilized. Fig.3 shows the comparison of the present results with [17], where an excellent agreement is observed. It strengthens the argument that the closed-form expressions presented herein are very effective.

4.2. Bar with exponentially varying section

This example is to illustrate the behavior of nanobars of variable section, and the possible convergence characteristics of the present solution procedure. The axial stiffness of the bar is assumed to vary exponentially.

$$B = B_0 \exp\left(-\beta x / L\right) \tag{17}$$

In the case of uniform normal force, which results from a concentrated load at the free end (with other end fixed), displacement fields of different orders are as reported below.

$$u_0 = \frac{N_0 L\left(e^{\frac{\beta x}{L}} - 1\right)}{\beta B_0} \tag{18}$$

$$u_1 = \frac{N_0}{2B_0(L-\beta\kappa)(\beta\kappa+L)}\left[-\kappa L e^{\beta-\frac{L+x}{\kappa}+\frac{x}{\kappa}}\left(L+\beta\kappa\right)+\kappa L e^{\beta-\frac{L+x}{\kappa}+\frac{2x}{\kappa}}\left(L+\beta\kappa\right)\right.$$
$$\left.+\kappa L e^{\frac{L}{\kappa}-\frac{L+x}{\kappa}}\left(-L+\left(\beta\kappa+L\right)e^{x/\kappa}+\beta\kappa\left(1-2e^{\frac{\beta x}{L}+\frac{x}{\kappa}}\right)\right)\right] \tag{19}$$

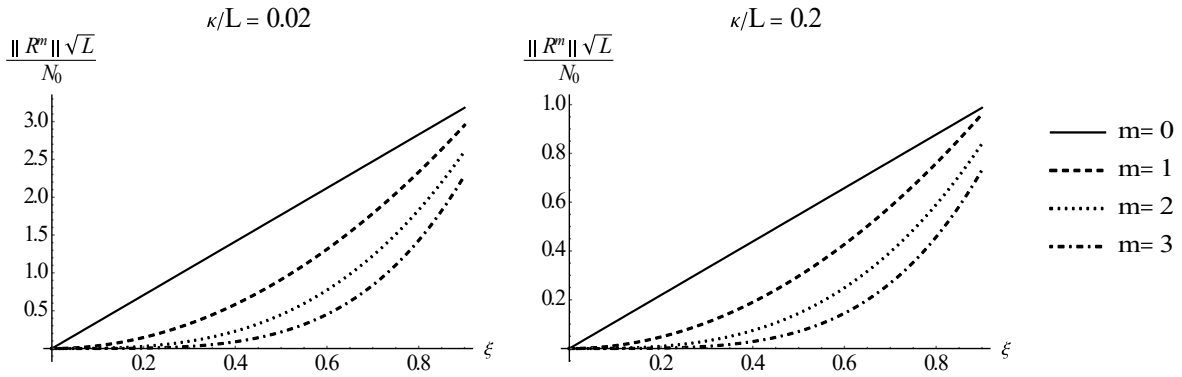

Figure 4. L_2-norm of balance residual for bar of variable section (**β** = 1) for different orders of approximation.

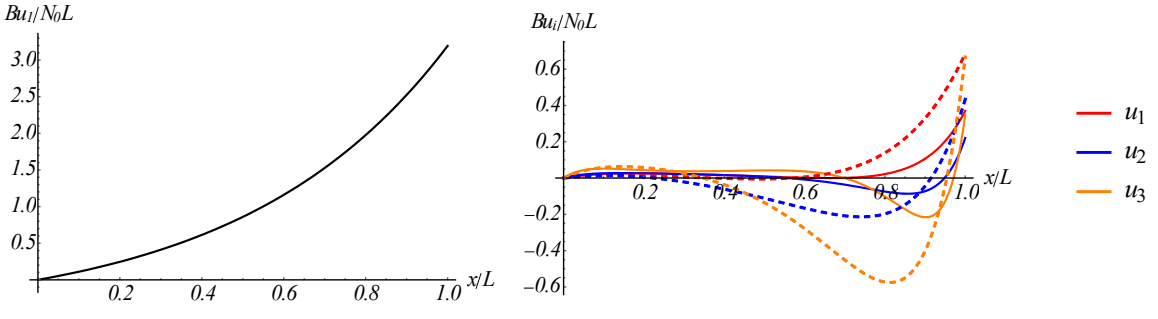

(a) (b)

Figure 5. Variations of displacement functions of different orders. Solid lines: **κ**/*L* = 0.1, Dashed lines. **κ**/*L* = 0.2, **β** = 2.

$$u_2 = \frac{N_0}{B_0(L-\beta\kappa)^2(\beta\kappa+L)^2}\Bigg[\kappa L^4\left(\frac{1}{4}-\frac{1}{4}e^{\frac{2L}{\kappa}}\right)+\kappa^2L^3\left(\frac{1}{4}\beta e^{-\frac{2L}{\kappa}}-\frac{\beta}{4}\right)$$
$$+\kappa^3L^2\left(\frac{1}{4}\beta^2e^{\frac{2L}{\kappa}}-\frac{5\beta^2}{4}\right)+\frac{1}{4}e^{-\frac{2(L-x)}{\kappa}-\frac{x}{\kappa}}\left(\kappa L^4-\beta\kappa^2L^3-\beta^2\kappa^3L^2+\beta^3\kappa^4L\right)$$
$$+e^{-\frac{x}{\kappa}}\left(\frac{L^4x}{2}+\kappa^3\left(\frac{5\beta^2L^2}{4}+\frac{\beta^3Lx}{2}\right)-\kappa\left(\frac{L^4}{4}+\frac{\beta L^3x}{2}\right)+\kappa^2\left(\frac{\beta L^3}{4}-\frac{\beta^2L^2x}{2}\right)\right.$$
$$\left.+\kappa^4L\left(2\beta^3e^{x\left(\frac{1}{\kappa}+\frac{\beta}{L}\right)}-\frac{5\beta^3}{4}\right)\right)+e^{\beta+\frac{L}{\kappa}-\frac{2(L-x)}{\kappa}-\frac{x}{\kappa}}\left(-\frac{L^5}{2}+\frac{L^4x}{2}+\kappa^3\left(\left(\frac{\beta^3}{2}-\frac{5\beta^2}{4}\right)L^2-\frac{1}{2}\beta^3Lx\right)\right. \quad (20)$$
$$\left.+\kappa\left(\left(\frac{1}{4}-\frac{\beta}{2}\right)L^4+\frac{1}{2}\beta L^3x\right)+\kappa^2\left(\left(\frac{\beta^2}{2}+\frac{\beta}{4}\right)L^3-\frac{1}{2}\beta^2L^2x\right)-\frac{5}{4}\beta^3\kappa^4L\right)$$
$$+e^{\beta-\frac{L}{\kappa}}\left(\frac{L^5}{2}+\frac{1}{2}\beta\kappa L^4-\frac{1}{2}\beta^2\kappa^2L^3+\left(\beta^2-\frac{\beta^3}{2}\right)\kappa^3L^2+\beta^3\kappa^4L\right.$$
$$\left.+e^{-\frac{x}{\kappa}}\left(-\frac{\kappa L^4}{4}-\frac{1}{4}\beta\kappa^2L^3+\frac{1}{4}\beta^2\kappa^3L^2+\frac{1}{4}\beta^3\kappa^4L\right)\right)+\kappa^4L\left(-\frac{3\beta^3}{4}-\frac{1}{4}\beta^3e^{-\frac{2L}{\kappa}}\right)\Bigg]$$

$$u_3 = \frac{N_0}{(\beta\kappa-L)^3(\beta\kappa+L)^3B_0}\Bigg[C_0+C_1e^{-\frac{3L+x}{\kappa}+\frac{2L+2x+\beta\kappa}{\kappa}}+C_2e^{-\frac{2L}{\kappa}}+C_3e^{\beta+\frac{2x}{\kappa}-\frac{3L+x}{\kappa}}+C_4e^{\frac{L}{\kappa}-\frac{3L+x}{\kappa}}$$
$$C_5e^{\beta-\frac{3L}{\kappa}}+C_6e^{\beta+\frac{2L}{\kappa}-\frac{3L+x}{\kappa}}C_7e^{-\frac{3L+x}{\kappa}+\frac{L+2x}{\kappa}}C_8e^{\beta-\frac{L}{\kappa}}+C_9e^{\frac{3L}{\kappa}-\frac{3L+x}{\kappa}}\Bigg] \quad (21)$$

The constants C_i in Eq.(21) are provided in the appendix. Similar to Eq. (16), a balance residual is defined. Figure 4 provides its variation with the fraction coefficient. The figures are provided for $\beta = 1$, but note that different values of this parameter do not alter the balance residual appreciably. Similar to the case of the uniform section, a smaller value of nonlocal parameter requires the consideration of more terms in the series expansion as it provides a sharper change of field functions providing higher gradients to be represented by higher-order terms.

Displacement functions of different orders, the expressions of which are given in Eqs. (18-21) in closed-form, are illustrated in Fig. 5. Zeroth-order, and higher-order terms are provided separetely as they differ in terms of the order of magnitude in this case. It is observed that higher-order displacement functions provide corrections which are more appreciable closer to the free end, where the *boundary effect* is present. Then again it is important to note that even if the magnitudes of higher-order terms seem to be quite high, they are to be modulated with the fraction coefficient before the final (approximate) displacement field is calculated.

5. CONCLUSIONS

Example problems of nanobars under different loading and boundary conditions are considered herein. It is the extension of the work by this author providing an approximate solution procedure based on formal series expansion of field functions in terms of so-called fraction coefficient providing the contribution of long-range interactions in constitutive relation. In particular, demonstration of the convergence of solutions in different scenarios is of great importance as a general convergence theorem for this method and this problem has not been proven yet. Moreover, a verification study is performed to compare the solutions presented in closed-form to that of an existing study which provides a numerical technique. The very good agreement between the results basically indicates the applicability of the closed-form expressions presented in this study, which provides great simplifications especially when it comes to material identification procedures where the solutions of a certain mathematical model are to be calculated repetitively. The results of this work basically enlarges the area of applicability of this series solution technique, and therefore may well be used as benchmark solutions.

REFERENCES

[1] Navier, C.-L.-M.-H. (1827) . Mémoire sur le lois de l'équilibre et du mouvement des corps solides élastiques (1821), Mémoires de l'Academie des Sciences de l'Institut de France, s. II, 7: 375–393.

[2] Cauchy, A.-L. (1828) . Sur l'équilibre et le mouvement d'un système de points matériels sollicités par des forces d'attraction ou de répulsion mutuelle, Exercices de Mathématiques, 3, 188–213, 1822, 1827; Oeuvres, 2(8): 227–252 .

[3] Poisson, S.D. (1829). Mémoire sur l'équilibre et le mouvement des corps élastiques 1828. Mémoires de l'Académie des Sciences de l'Institut de France, s. II, 8: 357–380.

[4] Trovalusci, P., Capecchi, D., Ruta, G. (2009). Genesis of the multiscale approach for materials with microstructure. Archive of Applied Mechanics 79: 981-997.

[5] Mindlin, R. D. (1964). Micro-structure in linear elasticity. Archive for Rational Mechanics and Analysis, 16(1): 51–78,.

[6] Kunin, I. A. (1968). The theory of elastic media with microstructure and the theory of dislocation. Kröner, E. (Eds.), Mechanics of Generalized Continua, Springer, Berlin Heidelberg, p. 321.

[7] Capriz, G. (1989). Continua with Microstructure. Springer Tracts in Natural Philosophy. Springer-Verlag.

[8] Maugin, G.A. (1993). Material Inhomogeneities in Elasticity. Applied Mathematics. Taylor & Francis.

[9] Eringen, A. C. (1999). Microcontinuum Field Theory. Springer.

[10] Eringen, A. C. (2002). Nonlocal Continuum Field Theories. Springer-Verlag.

[11] Rapaport, D.C. (1995). The Art of Molecular Dynamics Simulation. Cambridge University Press, Cambridge.

[12] Baggio, C., Trovalusci, P. (1998). Limit analysis for no-tension and friction three dimensional discrete systems. Mechanics of Structures and Mach., 26:287 – 304, (1998).

[13] Trovalusci, P. (2014). Molecular approaches for multifield continua: origins and current developments. Tomasz Sadowski and Patrizia Trovalusci (Eds.), Multiscale Modeling of Complex Materials: Phenomenological, Theoretical and Computational Aspects. Springer Vienna, p. 211–278.

[14] Kunin, I. A. (1984). On foundations of the theory of elastic media with microstructure. International Journal of Engineering Sciences, 22(8):969 – 978.

[15] Tuna, M., Leonetti, L., Trovalusci, P., Kirca, M. (2020). 'Explicit' and 'implicit' non-local continuous descriptions for a plate with circular inclusion in tension. Meccanica 55: 927–944.

[16] Tuna, M., Trovalusci, P. (2020). Scale dependent continuum approaches for discontinuous assemblies: 'explicit' and 'implicit' non-local models. Mech. Res. Commun., 103:103461, 6 pages.

[17] Abdollahi, R., Boroomand, B. (2013) Benchmarks in nonlocal elasticity defined by Eringen's integral model. International Journal of Solids and Structures 50(18): 2758-2771.

[18] Benvenuti, E., Simone, A. (2013). One-dimensional nonlocal and gradient elasticity: Closed-form solution and size effect. Mechanics

Research Communications, 48: 46-51.

[19] Zaera R., Serrano, Ó., Fernández-Sáez, J. (2019). On the consistency of the nonlocal strain gradient elasticity. International Journal of Engineering Sciences 138:65-81.

[20] Eroglu, U. (2020). Perturbation approach to Eringen's local/non-local constitutive equation with applications to 1-D structures. Meccanica, 55: 1119-1134.

[21] Eroglu, U. (2021). Approximate solutions to axial vibrations of nanobars in nonlinear elastic medium. Second International Nonlinear Dynamics Conference NODYCON 2021, Rome, 16-19 February.

[22] Eroglu, U., Ruta, G. (2021). Perturbations for non-local elastic vibration of circular arches. Second International Nonlinear Dynamics Conference NODYCON 2021, Rome, 16-19 February.

[23] Shaat, M. (2018). Correction of local elasticity for nonlocal residuals: application to Euler Bernoulli beams. Meccanica 53: 3015-3035.

[24] Barretta, R., Canadija, M., Luciano, R., de Sciarra, F.M. (2018). Stress-driven modeling of nonlocal thermoelastic behavior of nanobeams. International Journal of Engineering Science 126: 53-67

[25] Patnaik, S., Sidhardh, S., Semperlotti, F. (2021). Towards a unified approach to nonlocal elasticity via fractional-order mechanics. International Journal of Mechanical Sciences 189: 105992.

[26] Pisano, A.A., Fuschi, P., Polizzotto, C. (2021) Euler-Bernoulli elastic beam models of Eringen's differential nonlocal type revisited within a C0-continuous displacement framework. Meccanica 56: 2323-2337.

[27] Faghidian, S.A., Ghavanloo, E. (2021) Unified higher-order theory of two-phase nonlocal gardient elasticity. Meccanica 56:607-627.

[28] Shaat, M., Ghavanloo, E., Fazelzadeh, S.A. (2020). Review on nonlocal continuum mechanics: Physics, material applicability, and mathematics. Mechanics of Materials 150: 103587.

[29] Romano, G., Barretta, R., Diaco, M., de Sciarra, F.M. (2017). Constitutive boundary conditions and paradoxes in nonlocal elastic nanobeams. International Journal of Mechanical Sciences 121:151-156.

[30] Polyanin, P., Manzhirov, A. (2008). Handbook of integral equations. Chapman and Hall/CRC, London.

Appendix:

The constants C_i in 3rd-order displacement field of nanobar with exponentially varying section.

$$C_0 = -\frac{3\kappa L^6}{8} + \frac{3}{8}\beta\kappa^2 L^5 + \frac{3}{2}\beta^2\kappa^3 L^4 - \frac{3}{2}\beta^3\kappa^4 L^3 - \frac{33}{8}\beta^4\kappa^5 L^2 - \frac{15}{8}\beta^5\kappa^6 L \tag{A.1}$$

$$\begin{aligned} C_1 = &-\frac{3L^8}{8\kappa} - \frac{3\beta L^7}{8} + \frac{3L^7 x}{4\kappa} + \frac{3L^7}{2} + \frac{3}{4}\beta^2\kappa L^6 + \frac{3}{2}\beta\kappa L^6 - \frac{3\kappa L^6}{8} - \frac{3L^6 x^2}{8\kappa} + \frac{3}{4}\beta L^6 x \\ &- \frac{3L^6 x}{2} + \frac{3}{4}\beta^3\kappa^2 L^5 - \frac{9}{2}\beta^2\kappa^2 L^5 - \frac{3}{8}\beta\kappa^2 L^5 - \frac{3}{8}\beta L^5 x^2 - \frac{3}{2}\beta^2\kappa L^5 x - \frac{3}{2}\beta\kappa L^5 x \\ &- \frac{3}{8}\beta^4\kappa^3 L^4 - \frac{9}{2}\beta^3\kappa^3 L^4 + \frac{3}{2}\beta^2\kappa^3 L^4 + \frac{3}{4}\beta^2\kappa L^4 x^2 - \frac{3}{2}\beta^3\kappa^2 L^4 x + \frac{9}{2}\beta^2\kappa^2 L^4 x \\ &- \frac{3}{8}\beta^5\kappa^4 L^3 + 3\beta^4\kappa^4 L^3 + \frac{3}{2}\beta^3\kappa^4 L^3 + \frac{3}{4}\beta^3\kappa^2 L^3 x^2 + \frac{3}{4}\beta^4\kappa^3 L^3 x + \frac{9}{2}\beta^3\kappa^3 L^3 x \\ &+ 3\beta^5\kappa^5 L^2 - \frac{33}{8}\beta^4\kappa^5 L^2 - \frac{3}{8}\beta^4\kappa^3 L^2 x^2 + \frac{3}{4}\beta^5\kappa^4 L^2 x - 3\beta^4\kappa^4 L^2 x - \frac{33}{8}\beta^5\kappa L \\ &- \frac{3}{8}\beta^5\kappa^4 L x^2 - 3\beta^5\kappa^5 L x \end{aligned} \tag{A.2}$$

$$\begin{aligned} C_2 = &-\frac{3L^7}{4} + \frac{3L^6\kappa}{8} + \frac{3}{4}L^6\beta\kappa - \frac{3}{8}L^5\beta\kappa^2 + \frac{3}{2}L^5\beta^2\kappa^2 - \frac{3}{2}L^4\beta^2\kappa^3 - \frac{3}{2}L^4\beta^3\kappa^3 \\ &+ \frac{3}{2}L^3\beta^3\kappa^4 - \frac{3}{4}L^3\beta^4\kappa^4 + \frac{9}{8}L^2\beta^4\kappa^5 + \frac{3}{4}L^2\beta^5\kappa^5 - \frac{9}{8}L\beta^5\kappa^6 \end{aligned} \tag{A.3}$$

$$C_3 = -\frac{3L^6\kappa}{16} - \frac{3}{16}L^5\beta\kappa^2 + \frac{3}{8}L^4\beta^2\kappa^3 + \frac{3}{8}L^3\beta^3\kappa^4 - \frac{3}{16}L^2\beta^4\kappa^5 - \frac{3}{16}L\beta^5\kappa^6 \tag{A.4}$$

$$C_4 = \frac{3L^6\kappa}{16} - \frac{3}{16}L^5\beta\kappa^2 - \frac{3}{8}L^4\beta^2\kappa^3 + \frac{3}{8}L^3\beta^3\kappa^4 + \frac{3}{16}L^2\beta^4\kappa^5 - \frac{3}{16}L\beta^5\kappa^6 \tag{A.5}$$

$$C_5 = \frac{3L^6\kappa}{16} + \frac{3}{16}L^5\beta\kappa^2 - \frac{3}{8}L^4\beta^2\kappa^3 - \frac{3}{8}L^3\beta^3\kappa^4 + \frac{3}{16}L^2\beta^4\kappa^5 + \frac{3}{16}L\beta^5\kappa^6 \tag{A.6}$$

$$\begin{aligned} C_6 = &-\frac{3L^7}{8} - \frac{3L^6 x}{8} + \frac{9L^6\kappa}{16} - \frac{3}{8}L^6\beta\kappa - \frac{3}{8}L^5 x\beta\kappa + \frac{9}{16}L^5\beta\kappa^2 + \frac{3}{4}L^5\beta^2\kappa^2 \\ &+ \frac{3}{4}L^4 x\beta^2\kappa^2 - \frac{15}{8}L^4\beta^2\kappa^3 + \frac{3}{4}L^4\beta^3\kappa^3 + \frac{3}{4}L^3 x\beta^3\kappa^3 - \frac{15}{8}L^3\beta^3\kappa^4 - \frac{3}{8}L^3\beta^4\kappa^4 \\ &- \frac{3}{8}L^2 x\beta^4\kappa^4 + \frac{21}{16}L^2\beta^4\kappa^5 - \frac{3}{8}L^2\beta^5\kappa^5 - \frac{3}{8}Lx\beta^5\kappa^5 + \frac{21}{16}L\beta^5\kappa^6 \end{aligned} \tag{A.7}$$

$$C_7 = \frac{3L^7}{4} - \frac{3L^6 x}{8} - \frac{9L^6\kappa}{16} - \frac{3}{4}L^6\beta\kappa + \frac{3}{8}L^5 x\beta\kappa + \frac{9}{16}L^5\beta\kappa^2 - \frac{3}{2}L^5\beta^2\kappa^2 + \frac{3}{4}L^4 x\beta^2\kappa^2$$
$$+\frac{15}{8}L^4\beta^2\kappa^3 + \frac{3}{2}L^4\beta^3\kappa^3 - \frac{3}{4}L^3 x\beta^3\kappa^3 - \frac{15}{8}L^3\beta^3\kappa^4 + \frac{3}{4}L^3\beta^4\kappa^4 - \frac{3}{8}L^2 x\beta^4\kappa^4$$
$$-\frac{21}{16}L^2\beta^4\kappa^5 - \frac{3}{4}L^2\beta^5\kappa^5 + \frac{3}{8}Lx\beta^5\kappa^5 + \frac{21}{16}L\beta^5\kappa^6 \tag{A.8}$$

$$C_8 = -\frac{9L^7}{8} + \frac{3L^7\beta}{8} + \frac{3L^8}{8\kappa} - \frac{3L^6\kappa}{16} - \frac{9}{8}L^6\beta\kappa - \frac{3}{4}L^6\beta^2\kappa - \frac{3}{16}L^5\beta\kappa^2 + \frac{15}{4}L^5\beta^2\kappa^2$$
$$-\frac{3}{4}L^5\beta^3\kappa^2 + \frac{3}{8}L^4\beta^2\kappa^3 + \frac{15}{4}L^4\beta^3\kappa^3 + \frac{3}{8}L^4\beta^4\kappa^3 + \frac{3}{8}L^3\beta^3\kappa^4 - \frac{21}{8}L^3\beta^4\kappa^4 + \frac{3}{8}L^3\beta^5\kappa^4$$
$$+\frac{45}{16}L^2\beta^4\kappa^5 - \frac{21}{8}L^2\beta^5\kappa^5 + \frac{45}{16}L\beta^5\kappa^6 \tag{A.9}$$

$$C_9 = -\frac{3L^6 x}{2} - \frac{3}{8}L^5 x^2\beta + \frac{3L^6 x^2}{8\kappa} + \frac{3L^6\kappa}{8} + \frac{3}{2}L^5 x\beta\kappa - \frac{3}{4}L^4 x^2\beta^2\kappa$$
$$-\frac{3}{8}L^5\beta\kappa^2 + \frac{9}{2}L^4 x\beta^2\kappa^2 + \frac{3}{4}L^3 x^2\beta^3\kappa^2 - \frac{3}{2}L^4\beta^2\kappa^3 - \frac{9}{2}L^3 x\beta^3\kappa^3$$
$$+\frac{3}{8}L^2 x^2\beta^4\kappa^3 + \frac{3}{2}L^3\beta^3\kappa^4 - 3L^2 x\beta^4\kappa^4 - \frac{3}{8}Lx^2\beta^5\kappa^4 + \frac{33}{8}L^2\beta^4\kappa^5$$
$$+3Lx\beta^5\kappa^5 - \frac{33}{8}L\beta^5\kappa^6 + 6e^{\frac{x\beta}{L}+\frac{x}{\kappa}}L\beta^5\kappa^6 \tag{A.10}$$

doi: https://doi.org/10.26701/ems.773106

EUROPEAN MECHANICAL SCIENCE
e-ISSN: 2587-1110

Research Paper

Numerical Investigation of Fatigue Behavior of Non-patched and Patched Aluminum/Composite Plates

Hamit Adin[1*], Zeyni Sağlam[2], Mehmet Şükrü Adin[3]

[1,2,3]Department of Mechanical Engineering, University of Batman, Batman, Turkey

Abstract

In this study, the fatigue behavior of composite patched and non-patched Al 5083 aluminum plates was numerically investigated. Al 5083 Aluminum plates with semi-circular notched (2, 3 and 4 mm long cracked) and "V" notched (30°, 45° and 60° angled) were used in the analyzes. Mechanical properties of Al 5083 Aluminum plate, DP460 type adhesive of produced by 3M and $[0°]_8$ glass fiber reinforced composite patch material was used for the study. The Finite Element Method was applied for numerical study. Numerical analyzes were performed with the Ansys version 15.0 Workbench Package program. As a result of the numerical study, the highest fatigue life (1593.2 N) is seen on the 30° angled "V" notched and patched specimen. However, the fatigue life in non-patched specimen (30° angled "V" notched) was found to be 277.69 N. Thus, the study revealed that the composite patch's contribution is very important.

Keywords: Aluminum, Composite, Patch, Notch, Crack, Fatigue analysis

1. INTRODUCTION

Aluminum and composite materials are used extensively in different industrial areas such as aviation, space, automotive and marine. Because of their intense use, experimental research is required to develop, as strength and repair, these materials. Experimental research to develop these materials requires significant financial resources and time. Therefore, there has been interest in numerical analysis. The main reason for interest in numerical analysis is that it is very close to experimental results. In addition, through numerical analysis programs, it is possible to find solutions to the damage that may occur in these materials in advance [1-11]. There are many numerical studies on different types of Aluminum and Composite materials [3, 6, 8, 9, 11]. However, these materials are used in many different areas. Therefore, every study on these materials is important.

Can C. [12] investigated experimentally and numerically the fiberglass epoxy composite patches applied on damaged Al 2024 T3 aluminum sheets. In study, the critical lines were determined and the stress distributions on the samples along these lines were examined. His study showed that the numerical results are very close to the experimental results. In a study performed by Ahmet S. [13], the Al 5754 aluminum material repaired with composite patch were experimentally and numerically investigated. As a result of his investigation, he stated that the stresses on double-sided composite patched aluminum sheets are less. Uğur S. [14] experimentally performed the tensile and bending tests of the Al-2024 T3 aluminum adherend material repaired with a graphite/epoxy patch and compared the results with numerical analysis. He stated that the experimental and numerical analysis were in harmony as a result of the examination. Osman A. [15] investigated repairing damaged glass fiber reinforced epoxy composite plates by using composite patches. In the study, the effect of patch size and patch number changes on flexural stress behavior was investigated experimentally and numerically. As a result of the study, he stated that numerical analysis results and experimental results were very close. Mehmet R. [16] examined experimentally and numerically by repairing elliptical damaged glass fiber reinforced composite plates with the same material. In his investigation, he showed that the tensile stresses of the repaired glass fiber reinforced composite plates were compatible with the numerical ones. Abdulkerim P. [17] examined the repair performance by subjecting the repaired composite plates to a tensile test. The result of the research indicated that the experimental and numerical results were compatible.

The harmony of the results of the experimental and numerical studies mentioned above increases the importance of numerical studies. Therefore, in our study, the fatigue behavior of composite patched and non-patched Al 5083 aluminum plates (semi-circular and "V" notched) was numeri-

* Corresponding author
Email: hamit.adin@batman.edu.tr

European Mechanical Science (2021), 5(4): 168-176
doi: https://doi.org/10.26701/ems.923798
Received: April 20, 2021
Accepted: June 1, 2021

cally investigated. Thus, the effects of both patch and notch shapes on fatigue life were found.

2. MATERIAL AND METHOD

In our study, numerical analyzes were performed using the Finite Element Method. Numerical analyzes were performed with the Ansys version 15.0 Workbench Package program [18, 19]. As materials, Al 5083 aluminum plate, [0°]8 glass fiber reinforced composite patch and DP460 type adhesive of produced by 3M were preferred. The mechanical properties of these materials were used in numerical analysis. The mechanical properties of Al 5083 Aluminum plate, [0°]8 glass fiber reinforced composite patch and DP-460 adhesive materials used in the analyzes are given in Table 1, Table 2 and Table 3, respectively [20-22].

Table 1. Mechanical properties of Al 5083 Aluminum plate [20].

Elasticity module	70000 MPa
Poisson ratio	0.3897
Tensile strength	345 MPa
Yield strength	270 MPa
Thermal conductivity	204 W/(m.K)
Thermal expansion coefficient	2.4e-005 1/K
Mass density	2660 kg/m^3
Specific heat	940 J/(kg.K)

Table 2. Mechanical properties of $[0°]_8$ glass fiber reinforced composite patch [21].

E_1	40510 MPa
E_2=E_3	13960 MPa
G_{12}	3100 MPa
G_{13}=G_{23}	1100 MPa
ϑ_{12}	0.22
$\vartheta_{13} = \vartheta_{23}$	0.15

Table 3. Mechanical properties of 3M brand DP460 type industrial adhesive [22].

Adhesive thickness	0.25 mm
Shear stress	23.99 MPa
Shear strength	33.35 MPa
Shear module	560 MPa
Elasticity Module	2077.1 MPa
Poisson's ratio	0.38
Tensile strength	44.616 MPa

In the study, Al 5083 Aluminum plates with semi-circular notched (with 2, 3 and 4 mm cracks) or "V" shaped notches (30°, 45° and 60° angled) were analyzed non-patched or patched. As patch material, $[0°]_8$ glass fiber reinforced composites were used. In numerical study, the effect of non-patched and patched aluminum plates on fatigue behaviors was investigated. Dimensions of Al 5083 Aluminum plates used in numerical studies are given in Fig. 1 and Fig. 2.

As seen in Fig. 1, Al 5083 Aluminum plates have semi-circular notch on one and both sides and 2, 3 and 4 mm long cracks advanced towards the interior.

As seen in Fig. 2, Al 5083 Aluminum plates have notches on one and both sides, these notches have 6 mm length and 30°, 45° and 60° angles. Dimensions of $[0°]_8$ glass fiber reinforced composite patch used in numerical analysis are given in Fig. 3.

As a result of the literature review, the thickness of the adhesive was selected as 0.25 mm [23-25].

3-Dimensional pictures of the materials used in numerical analysis are given in Fig. 4.

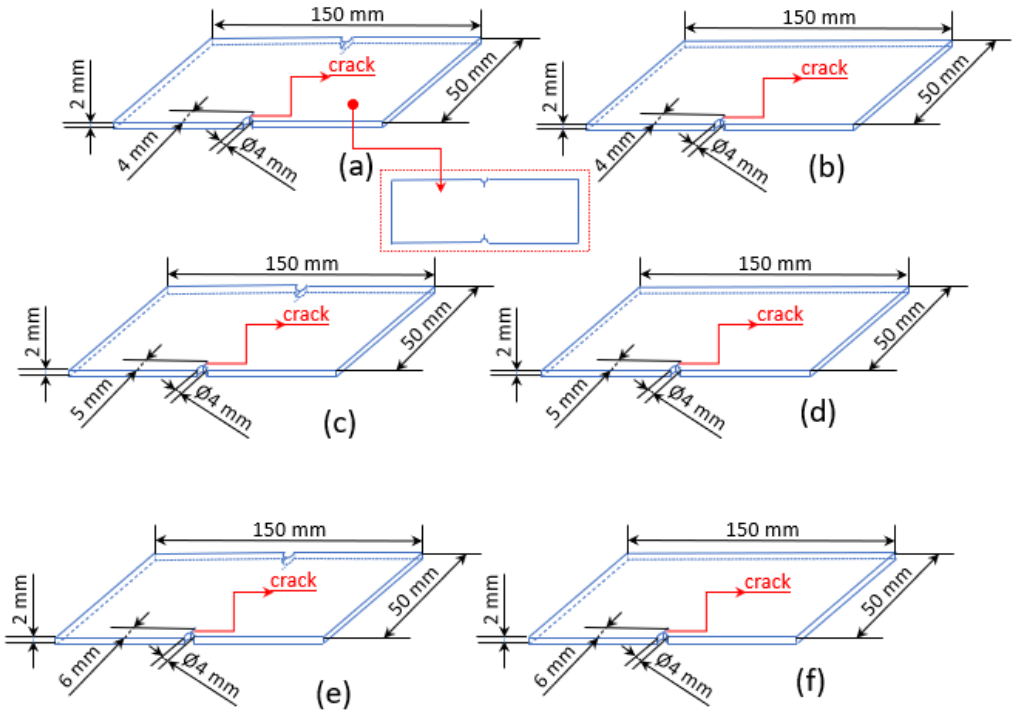

Figure 1. Dimensions of Al 5083 Aluminum plates with 2 mm (a, b), 3 mm (c, d) and 4 mm (e, f) cracks starting from the semi-circular notch (single and double sided).

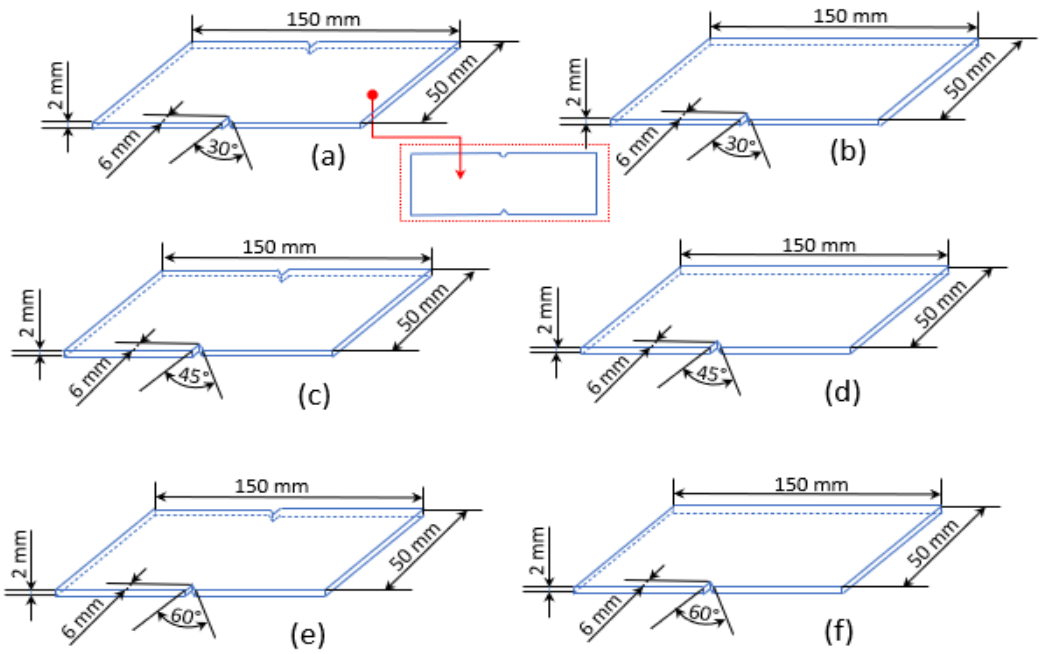

Figure 2. Dimensions of Al 5083 plates with notch length 6 mm, notch angles 30° (a, b), 45° (c, d), and 60° (e, f) (single and double sided).

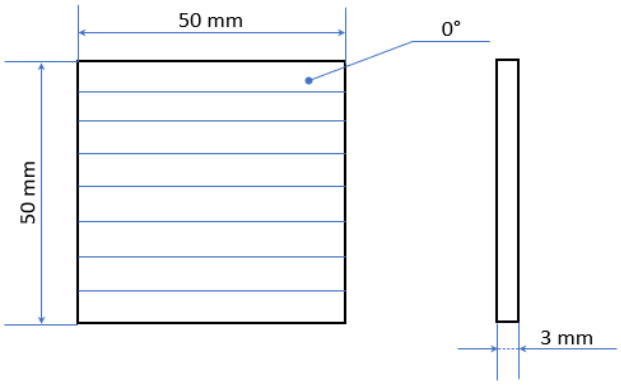

Figure 3. Dimensions of $[0°]_8$ glass fiber reinforced composite patch.

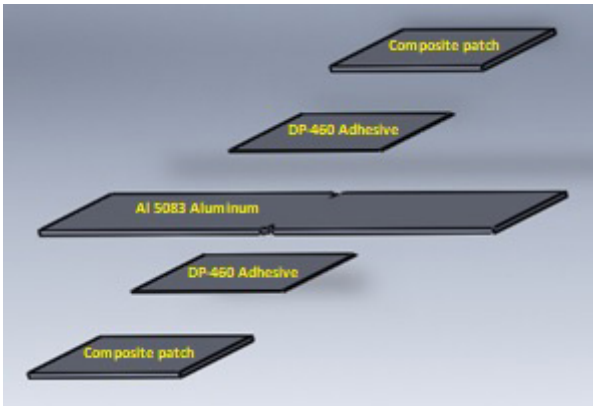

(a)

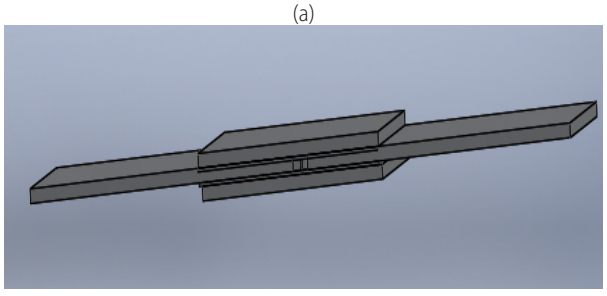

(b)

Figure 4. 3D pictures of materials before (a) and after (b) joining.

The materials, whose technical drawings were prepared first, were drawn in 3D using the Solidworks program, and then transferred to the Ansys Workbench 15.0 Package program. In the study, the fatigue lives, Von-mises stresses and deformations of the materials were investigated by applying tensile-compression load (R = -1). One end of the sample is modeled in a fixed support state. At the other end, pressure was applied based on 45% of the yield stress value of the Al 5083 aluminum plate sample. While the yield value of the Al 5083 Aluminum material, which is the analysis sample, is 270 MPa, tensile-compression loads were applied with a value of 121.5 MPa, which is 45% of this value. Pressure was applied directly opposite the fixed end. In Ansys, adding material to the contact parts of the joint (a), the screen accessed with the model (b), determination of the support and pressure points (c) and the mesh applied (d) are given in Fig. 5.

The number of elements and nodes of single and double sided, semi-circular notched and cracked (with 2, 3 and 3 mm) samples after mesh structure are given in Table 4.

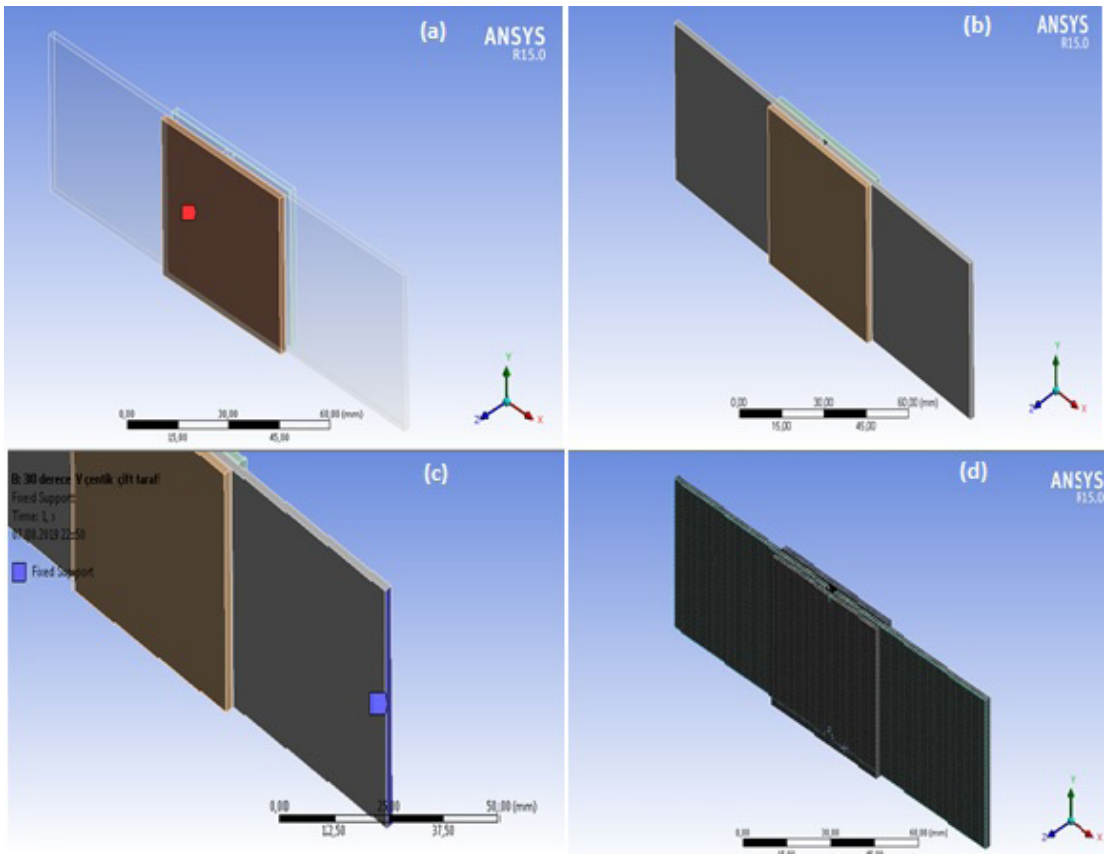

Figure 5. Pictures of adding material to the contact parts of the joint (a), the screen accessed with the model (b), determination of the support and pressure points (c) and the mesh applied (d).

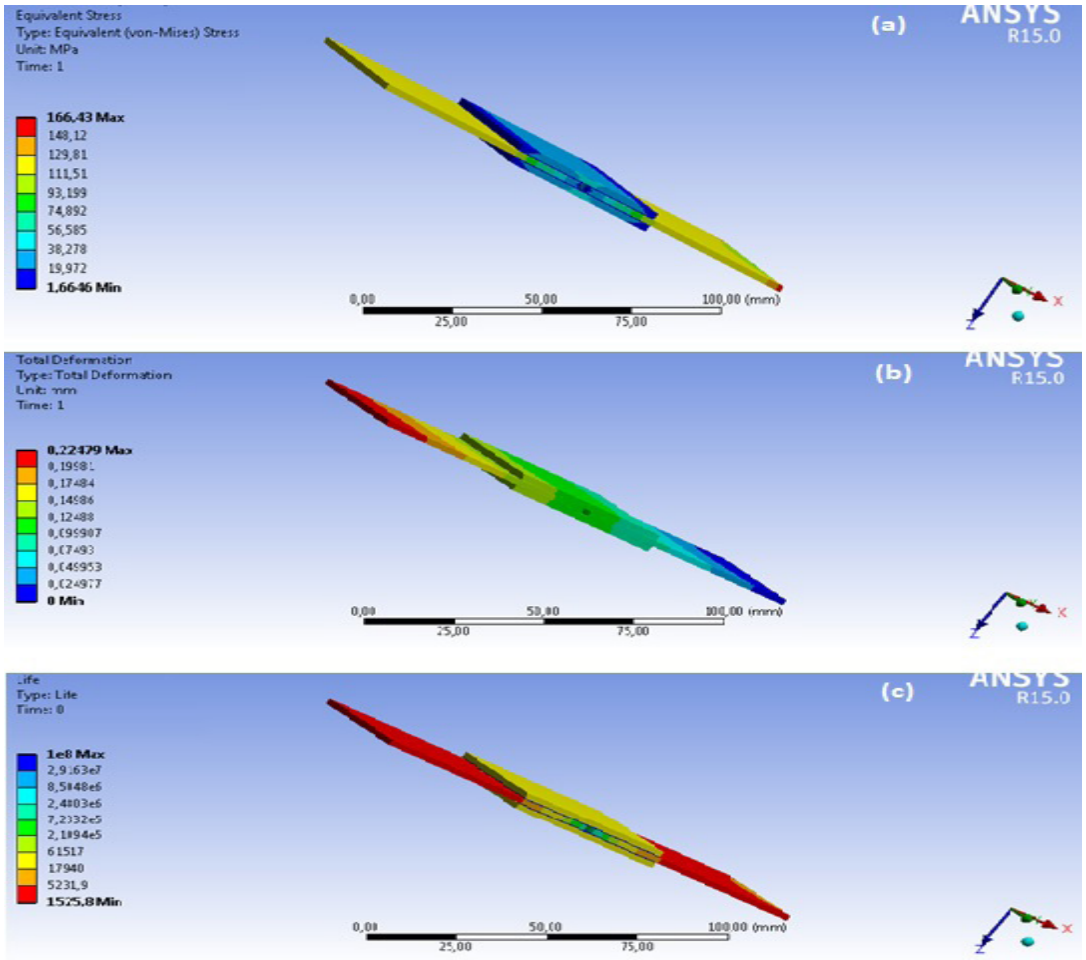

Figure 6. Pictures of Von-mises stress analysis (a), total deformation analysis (b) and fatigue life analysis (c) of the joints.

Table 4. The number of elements and nodes of single and double sided, semi-circular notched and cracked (with 2, 3 and 3 mm) samples.

Crack length		Semi-circular notches and cracks			
		One sided		Double-sided	
		Non-patched	Patched	Non-patched	Patched
2 mm	Elements	7548	102548	15172	110172
	Nodes	53879	695099	85187	726407
3 mm	Elements	7560	102560	15276	110276
	Nodes	53953	695173	85727	726947
4 mm	Elements	7584	102584	15194	110194
	Nodes	54126	695346	85332	726552

The number of elements and nodes of the samples with single and double sided "V" notched (30, 45 and 60 angled) after the mesh structure are given in Table 5.

Von-mises stress analysis (a), total deformation analysis (b) and fatigue life analysis (c) of the joints in the study are given in Fig. 6.

3. RESULTS AND DISCUSSION

3.1. Fatigue life

The results of fatigue analysis applied to Al 5083 aluminum plates (non-patched and patched) with semi-circular notches (single and double sided) and cracks (2, 3 and 4mm) are given in Table 6. Here, N symbolizes the number of cycles.

Table 6. The results of fatigue analysis.

With semi-circular notch and crack	Number of cycles (N)			
	Single sided		Double sided	
Crack length	Non-patched	Patched	Non-patched	Patched
2 mm	347.67	1267	428.68	1266.70
3 mm	321.80	1266.90	373.86	1266.40
4 mm	265.04	1266.80	323.20	1266.30

As can be seen in Table 6, in numerical analysis, the fatigue life of the patched samples was found to be quite high (about 3.5 times on average). It has been observed that the increase in the length of the cracks (2, 3 and 4 mm) negatively affected the fatigue life. It has been observed that samples with

Table 5. The number of elements and nodes of the samples with single and double sided "V" notched (30, 45 and 60 angled).

"V" Notch angle		"V" notched			
		One sided		Double-sided	
		Non-patched	Patched	Non-patched	Patched
30° Angled	Elements	71215	166215	15354	110354
	Nodes	128928	770148	86148	727368
45° Angled	Elements	70672	165672	15186	110186
	Nodes	128031	769251	85176	726396
60° Angled	Elements	15028	110028	15126	110126
	Nodes	84283	725503	84846	726066

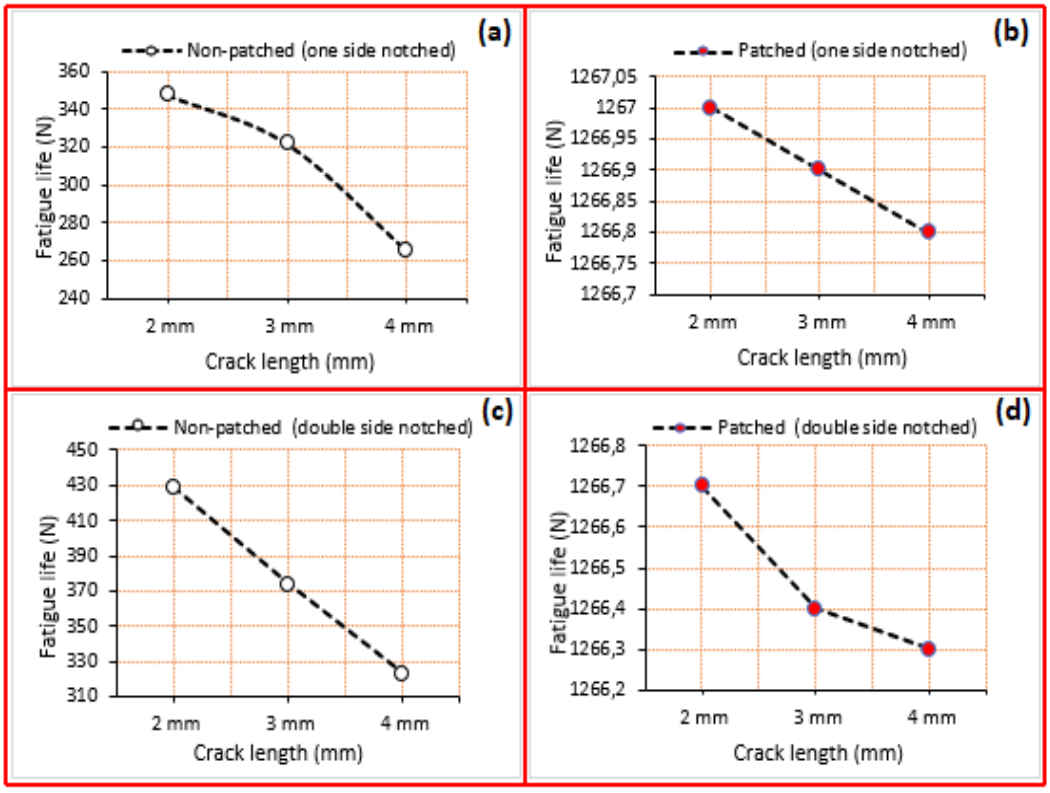

Figure 7. Fatigue lives of the samples.

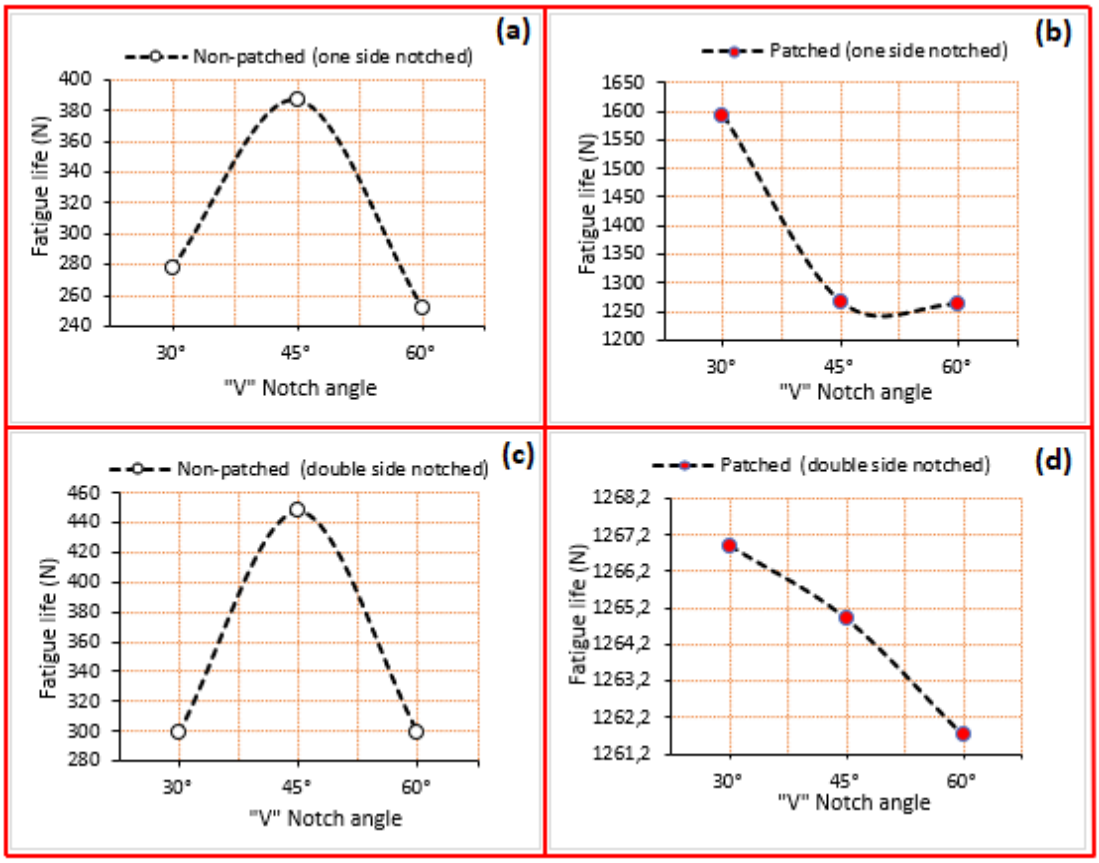

Figure 8. Fatigue lives of the samples.

Table 7. The results of fatigue life analysis.

With "V" notch Angle	Number of cycles (N)			
	Single sided		Double sided	
	Non-patched	Patched	Non-patched	Patched
30°	277.69	1593.2	298.45	1266.90
45°	387.11	1265.5	448.04	1264.90
60°	251.66	1262.3	298.70	1261.70

notches and cracks on one side have lower fatigue life than samples with notches and cracks on both sides.

As can be seen in Fig. 7 a, the increase in crack length caused a decrease in fatigue life. The fatigue lives of the notched (one-sided) and non-patched samples decreased due to increased crack length (Fig. 7 c). Fig. 7 b shows a decrease in fatigue life with increasing crack size. However, the fatigue lives of the samples are very close to each other in every crack size. When a comparison is made between Fig. 7 a and Fig. 7 b, it is seen that the fatigue life of the patched samples is quite high (Fig. 7 b and d). Therefore, it has shown that composite patches applied to semi-circular notched and cracked aluminum samples are very successful. In patched samples, as a result of the absorption of the applied load by the patches, the fatigue life has increased and the effect of crack lengths has been reduced to negligible. The linearity of the graph in samples with cracks on one side is due to the similarity of damage in one region of the load.

The results of the fatigue life analysis applied to single and double sided "V" notched (30°, 45° and 60° angled) Al 5083 aluminum plates (Non-patched and patched) are given in Table 7.

As seen in Table 7, in numerical analysis, non-patched samples have a lower fatigue life than patched samples. The fatigue life of the sample with 30° angled "V" notch (patched) on one side was found to be higher than all other samples. The fatigue life of the "V" notch with 30° angled is quite high because it is patched with composite material and has the least notch dimensions.

The fatigue life graphs of the samples with "V" shaped (30°, 45° and 60° angled) notches on their single and double sides are given in Fig. 8. The most striking point in the graph is that the fatigue life of the 45° angled "V" notch (non-patched) sample is much higher than the 30° and 60° angled samples (Fig. 8 a and c). On the other hand, the fatigue lives of 30° and 60° angled (non-patched) samples are close to each other, but the fatigue life of the 30° angled sample is longer (Fig. 8 a). The reason why the 45° angled "V" notched (non-patched) sample has the highest fatigue life is that the stress creates agglomeration at this point (Fig. 8 a and c). In Fig. 8 b and d, the highest fatigue lives are at 30° angled ("V" single notched) patched samples. On average, the fatigue lives of samples (patched) with "V" notches at 45° and 60° angles are close to each other (Fig. 8 b and d). It is also

understood from the graphs that the fatigue life of the composite patch samples is quite high (Fig. 8 b and d). As seen in Fig. 8, samples with "V" notches on single and double sides are 30° angled (patched) samples with the highest fatigue life. However, the highest fatigue life is the 30° angled, one side notched and patched sample.

3.2. Von-mises stresses

The results of the Von-mises stresses of the non-patched and patched semi-circular notched (and cracked) samples are given in Table 8. As can be understood from Table 8, the lowest Von-mises stress values are seen in composite patched samples. When the samples (patched) with "V" semi-circular notches and cracks (2, 3 and 4 mm long) on one side are compared with the samples (patched) with "V" semi-circular notches and cracks (2, 3 and 4 mm long) on both sides, it is seen that the stress values are very close to each other. This shows that the effect of the composite patch on the stress is quite high. Since the semi-circular notch and crack are symmetrical on the part, it slightly reduces the stress value.

Table 8. The results of Von-mises stresses.

With semi-circular notch and crack	Von-mises stresses (MPa)			
	Single sided		Double sided	
Crack length	Non-patched	Patched	Non-patched	Patched
2 mm	291.09	178.30	264.43	178.32
3 mm	300.94	178.31	281.85	178.34
4 mm	325.65	178.31	300.39	178.34

As can be seen from Fig. 9, while the stresses are less in patched samples, the stresses are higher in non-patched samples. Because, in composite-patched samples, some of the stresses are distributed over the composite and adhesive, so the stresses are less.

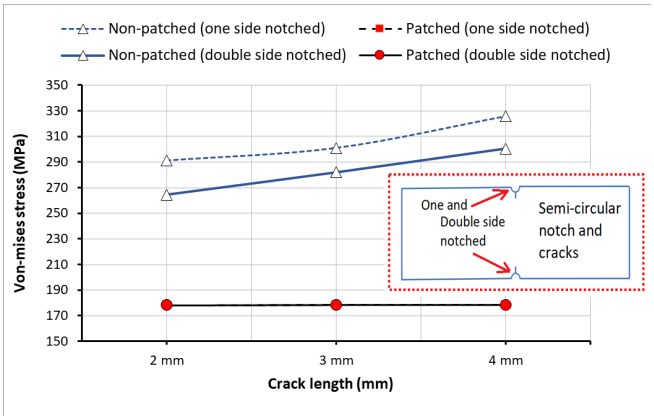

Figure 9. Von-mises stresses.

The results of the Von-mises stresses of the non-patched and patched "V" notched (30°, 45° and 60° angled) samples are given in Table 9.

Table 9. The results of Von-mises stresses.

With "V" notch	Von-mises stresses (MPa)			
	Single sided		Double sided	
Angle	Non-patched	Patched	Non-patched	Patched
30°	319.71	163.67	310.53	178.31
45°	277.41	178.38	258.8	178.41
60°	332.24	178.54	310.43	178.57

As seen in Table 9, the maximum stress values in patched samples are lower than non-patched samples. Because excessive stresses are distributed over the composite patch and adhesive. It is seen that the Von-mises stress values of non-patched 45° angled "V" notched joints are lower than those of 30° and 60° joints. It is seen that the 45° angle is a critical value in "V" notched connections and it is beneficial. The symmetrical notches in non-patched samples are beneficial in terms of stresses.

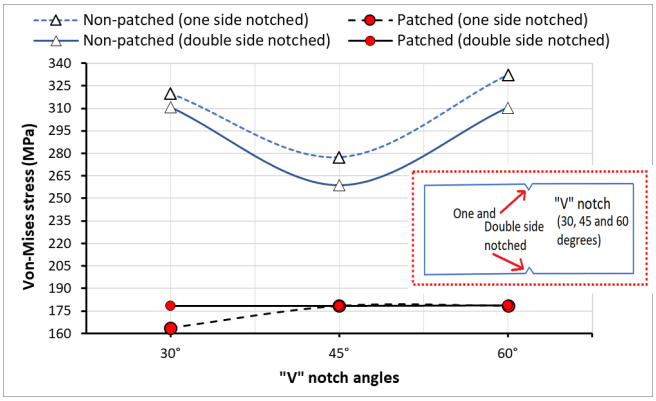

Figure 10. Von-mises stresses.

As can be seen from Fig. 10, while the stress is less in patched samples, it is higher in non-patched samples. Because, the composite patches have reduced the stresses.

3.3. Deformations

The results of the deformation of the non-patched and patched semi-circular notched (and cracked) samples are given in Table 10.

Table 10. The results of deformations.

With semi-circular notch and crack	Deformation (mm)			
	Single sided		Double sided	
Crack length	Non-patched	Patched	Non-patched	Patched
2 mm	0.26905	0.22522	0.26274	0.22451
3 mm	0.27571	0.22607	0.26513	0.22479
4 mm	0.28411	0.2262	0.26811	0.22475

As seen in Table 10, the deformation values in patched samples are lower than those non-patched. Because composite patches have helped prevent deformation in samples. In non-patched samples, deformation increased due to the increase in crack size.

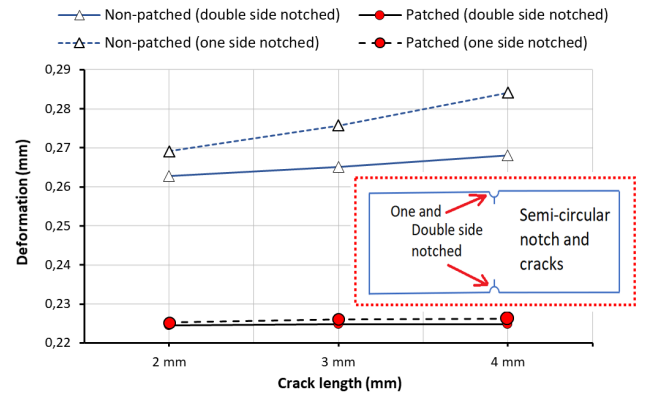

Figure 11. Deformation results.

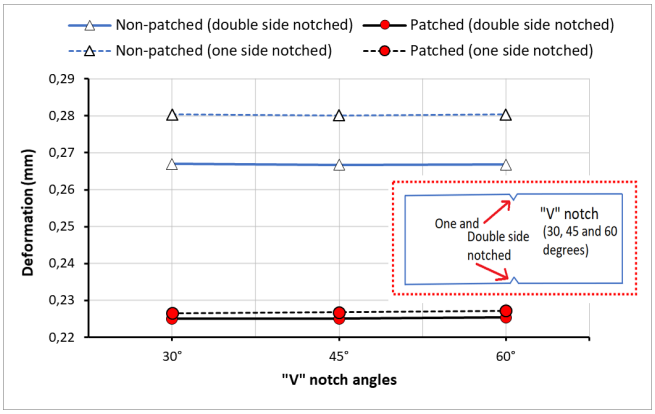

Figure 12. Deformation results.

As can be seen from Fig. 11, while the deformation is less in the patched samples, the deformation is higher in the non-patched samples. Because, in composite-patched samples, some of the stresses are distributed over the composite and adhesive, so the deformation is less.

The results of the deformation of the non-patched and patched "V" notched (30°, 45° and 60° angled) samples are given in Table 11.

Table 11. The results of deformations.

With "V" notch	Deformation (mm)			
	Single sided		Double sided	
Angle	Non-patched	Patched	Non-patched	Patched
30°	0.28034	0.22650	0.26692	0.22505
45°	0.28008	0.22672	0.26674	0.22499
60°	0.28032	0.22720	0.26683	0.22532

As seen in Fig. 13, while the deformation is less in the patched samples, the deformation is higher in the non-patched samples.

In addition, it is seen from Fig. 12 that the deformations of the single and double notched connections are very close to each other. This revealed that the contribution of the composite patch is very important.

4. CONCLUSIONS

In our numerical study, Al 5083 aluminum plate, glass fiber reinforced composite patch and DP460 adhesive were used. Analyzes were performed using the Finite Element Method. The Finite Element analyzes were made in Ansys Workbench. In the study, Al 5083 Aluminum plates with semi-circular notched (with 2, 3 and 4 mm cracks) or "V" shaped notches (30°, 45° and 60° angles) were used non-patched or patched. In numerical study, the fatigue lives, Von-mises stresses and deformations of the materials were investigated. Obtained results are presented below.

The fatigue lives of the patched samples with semi-circular notches and cracks (2, 3 and 4 mm long) on both sides was very close to each other. Fatigue lives decreases in proportion to the increase in the length of the crack, but this decrease seems to have a very low value. The fatigue lives of the samples with one-sided semi-circular notches and cracks were seriously affected by the increase in crack length. It has been stated in the literature that smaller cracks increase the patch efficiency [26-28]. In the analysis, the deformation was mostly seen in the area of the crack. The same situation is observed in double sided semi-circular and cracked samples.

One side "V" notched (30°, 45° and 60° angles) and patched specimens have been observed to increase fatigue life as the angle of the notch decreases. The highest fatigue life (1593.2 N) is seen on the 30° angled "V" notched and patched sample. However, the fatigue life in non-patched specimen (30° angled "V" notched) was found to be 277.69 N. As in the literature (in experimental studies with "V" notches), the positive effect of the composite patch on the fatigue life has been observed [29, 30]. The same situation is observed in double sided "V" notched samples. However, it is seen that the fatigue lives of the samples with double sided "V" notches does not change much with the angle.

In non-patched samples, the highest fatigue life was found with a 45° angled "V" notch on one side. Then, samples with 30° and 60° angles "V" notched are followed, respectively. The highest fatigue life of the non-patched specimens with "V" notches on double side is 45°, 60° and 30°, respectively.

The Von-mises stress and deformation values of single and double sided "V" notches (30°, 45° and 60° angles) and semi-circular notches (with 2, 3 and 4 mm cracks) were positively affected by the applied patches.

REFERENCES

[1] Carbas, R. J. C., Marques, E. A. S., & da Silva, L. F. M. (2021). The influence of epoxy adhesive toughness on the strength of hybrid laminate adhesive joints. Applied Adhesion Science, 9(1), 1-14.

[2] Deghoul, N., Errouane, H., Sereir, Z., Chateauneuf, A., & Amziane, S. (2019). Effect of temperature on the probability and cost analysis of mixed-mode fatigue crack propagation in patched aluminium plate. International Journal of Adhesion and Adhesives, 94, 53-63.

[3] Ergün, R. K., Adin, H., Şişman, A., & Temiz, Ş. (2018). Repair of an aluminum plate with an elliptical hole using a composite patch. Materials Testing, 60(11), 1104-1110.

[4] Wu, C., Gunnion, A. J., Chen, B., & Yan, W. (2015). Fatigue damage tolerance of two tapered composite patch configurations. Composite Structures, 134, 654-662.

[5] Gong, X. J., Cheng, P., Aivazzadeh, S., & Xiao, X. (2015). Design and optimization of bonded patch repairs of laminated composite structures. Composite Structures, 123, 292-300.

[6] Jian-Bin, H., Xu-Dong, L., & Zhi-Tao, M. (2015). Fatigue behavior of thick center cracked aluminum plates repaired by two-sided composite patching. Materials & Design, 88, 331-335.

[7] Saraç, İ., Adin, H., & Temiz, Ş. (2018). Experimental determination of the static and fatigue strength of the adhesive joints bonded by epoxy adhesive including different particles. Composites Part B: Engineering, 155, 92-103.

[8] Chung, K. H., & Yang, W. H. (2003). A study on the fatigue crack growth behavior of thick aluminum panels repaired with a composite patch. Composite Structures, 60(1), 1-7.

[9] Maligno, A. R., Soutis, C., & Silberschmidt, V. V. (2013). An advanced numerical tool to study fatigue crack propagation in aluminium plates repaired with a composite patch. Engineering Fracture Mechanics, 99, 62-78.

[10] Fekirini, H., Bouiadjra, B.B., Belhouari, M., Boutabout, B. & Serier, B., (2008). Numerical analysis of the performances of bonded composite repair with two adhesive bands in aircraft structures. Composite structures, 82(1),84-89.

[11] Adin, M.Ş., Kılıçkap, E. (2021). Strength of double-reinforced adhesive joints. Materials Testing, 63(2), 176-181.

[12] Canbolat, C. (2018). Repairement of Al 2024 T3 plates by means of fiberglass composite patches, Master thesis, Kahramanmaras Sutcu Imam University, Turkey.

[13] Saylık, A. (2016). The stress analysis of aluminum plates repaired with composite patch, Master thesis, Firat University, Turkey.

[14] Soy, U. (2005). The finite element analysis of bonded repair with composite patch, Master thesis, Sakarya University, Turkey.

[15] Ahlatlı, O. (2018). The expiremential and numerical investigation of the effects of dimension and number of layers of patches on bending stress behaviour of repairing composire plates having elliptical damage, Master thesis, Kahramanmaras Sutcu Imam University, Turkey.

[16] Ramazanoğlu, M. (2018). Experimental and numerical investigation of the effects of dimensions and number of layers of patches on tensile stress behaviour of repairing composite plates having elliptical damage, Master thesis, Kahramanmaraş Sutcu Imam University, Turkey.

[17] Parlamış, A. (2016). Investigation of patch repair performance for damaged composites pin loaded joint, Master thesis, Firat University, Turkey.

[18] ANSYS, (2014). ANSYS version R15 Canonsburg Pennsylvania, PA, USA. ANSYS Inc.

[19] Lee, H.-H., (2019). Finite Element Simulations with ANSYS Workbench 2019. SDC Publications.

[20] SolidWorks, (2013). Solidworks Software, SolidWorks Material Library. Dassault Systèmes, France. 3DExperience.

[21] Kiral, B.G. (2010). Effect of the clearance and interference-fit on failure of the pin-loaded composites. Materials & Design, 31(1), 85-93.

[22] Aydın, M.D., Akpınar, S., Erdoğan, S., Adnan, Ö. (2015). Determination of Mechanical Properties of Structural Adhesives From Adhesively Bonded Joints Subjected to Shear Load. Mühendis ve Makina, 56(668), 48-55.

[23] Sadeghi, M., Zimmermann, J., Saravana, K., Gabener, A., Dafnis, A., Schröder, K. (2020). Influence of fracture envelope on FE failure load prediction of adhesively bonded joints by using mixed mode bending tests. Procedia Structural Integrity, 28, 1601-1620.

[24] Nezhad, H.Y., Stratakis, D., Ayre, D., Addepalli, S., Zhao, Y. (2018). Mechanical performance of composite bonded joints in the presence of localised process-induced zero-thickness defects. Procedia Manufacturing, 16, 91-98.

[25] Adin, H. (2012). The effect of angle on the strain of scarf lap joints subjected to tensile loads. Applied Mathematical Modelling, 36(7), 2858-2867.

[26] Baker, A. (1999). Bonded composite repair of fatigue-cracked primary aircraft structure. Composite structures, 47(1-4), 431-443.

[27] Seo, D.-C., Lee, J.-J. (2002). Fatigue crack growth behavior of cracked aluminum plate repaired with composite patch. Composite Structures, 57(1-4), 323-330.

[28] Sun, C., Klug, J., Arendt, C. (1996). Analysis of cracked aluminum plates repaired with bonded composite patches. AIAA journal, 34(2), 369-374.

[29] Mohammed, S.M.K., Mhamdia, R., Albedah, A., Bouiadjra, B.A.B., Bouiadjra, B.B., Benyahia, F. (2021). Fatigue crack growth in aluminum panels repaired with different shapes of single-sided composite patches. International Journal of Adhesion and Adhesives, 105, 102781.

[30] Wang, Q.Y., Pidaparti, R.M. (2002). Static characteristics and fatigue behavior of composite-repaired aluminum plates. Composite Structures, 56(2), 151-155.

EUROPEAN MECHANICAL SCIENCE
e-ISSN: 2587-1110
Research Paper

Research of Effect on Gasoline-2-Propanol Blends on Exhaust Emission of Gasoline Engine with Direct Injection Using Taguchi Approach

Ekrem Tasoren*[1], Hasan Aydogan[2], Mehmet Selman Gokmen[3]*

[1]Selcuk University, Faculty of Technology, Department of Mechanical, Konya Turkey
[2]Selcuk University, Faculty of Technology, Department of Mechanical Engineering, Konya, Turkey
[3]Necmettin Erbakan University, Seydişehir Vocational School, Konya, Turkey

Abstract

One of the most important causes of global warming is the greenhouse gas effect caused by the increased CO_2 emission due to the use of petroleum-based fuels in internal combustion engines. O_2, H_2O, NO_X emissions released as a result of the combustion reaction and released into the atmosphere from the exhaust turn into nitric acid (HNO_3) as a result of some reactions taking place in nature. In addition, the OH radicals released as a result of these reactions that can not turn into nitric acid react with the ozone layer (O_3) and support the formation of hydroperoxyl (HO_2), which causes a harmful emission cycle. CO emissions, on the other hand, react with O_2 and NO_X and pollute the water vapor in the air, causing the O_2 level to drop. Despite quite a lot of work done to date, it is known that due to the increase in the number of gasoline engines, their environmental damage is excessive. In this study, the effect of 2-Propanol / Gasoline fuel mixtures on exhaust emission values has been experimentally investigated using Taguchi Approach. The input factors for Taguchi Approach are 2-Propanol ratio and Engine speed and output values are determined as carbon monoxide (CO), carbon dioxide (CO_2), hydrocarbon (HC), Nitrogen Oxide (NO_X), and Oxygen (O_2) emissions. In the created Taguchi design, experiments were planned by using an L9 orthogonal array. The engine speed was determined as 1500, 2500, and 3500 (rpm), and 2-propanol ratio was determined as 5%, 10%, and 15% (% by volume). Tests were conducted under partial load conditions. In tests conducted at 1500 rpm, CO emissions decreased by 41.99% compared to gasoline, while CO_2, HC, NO_x, and O_2 emissions decreased by 7,09%, 20,91%, 8.64%, and 20.34%, respectively. 2500 rpm test, CO, CO_2, HC, O_2, and NO_x reductions in emissions, respectively 16.60%, 2.09%, 17.39%, 10.64%, and 27.14% 3500 rpm, while the rate of decrease of the emission test values, respectively 25.30%, 4.88%, 29.09%, 9.72%, and 37.09% has been found in.

Keywords: Direct Injection, 2-Propanol, Exhaust Emissions, Taguchi Approach

5. INTRODUCTION

One of the most critical problems of today is environmental pollution. One of the primary sources of environmental pollution is the use of fossil fuels [1]. Fossil fuels are primarily used in internal combustion engines. Using biomass fuels instead of fossil fuels in these engines may reduce environmental pollution [2].

For engines that use gasoline as fuel, alcohol is considered a good biomass fuel. Alcohols obtained by biochemical processes have an alternative fuel potential with an excess oxygen content, renewable, and cleaner-burning [3]. Alcohols with a lower molecular weight than gasoline can significantly improve engine emissions when mixed with gasoline. Alcohols contain specific amounts of oxygen in their structures [4,5]. Alcohols have a smaller molecular structure than engine fuels, have oxygen in their structure, do not contain sulfur, carcinogenic substances, and heavy metals found in engine fuels, causing positive effects on exhaust emissions [6]. In this way, brighter and faster combustion is provided. Increasing the combustion speed improves combustion efficiency and ensures a more stable operation of the engine. In addition, by achieving high compression rates with fast combustion, efficiency can be increased without engine knock [7]. One of the alcohols that can be used as fuel in engines is 2-Propanol. It contains three carbons in the structure of 2-Propanol, defined by the formula C_3H_7OH. In addition, due to the presence of OH in its structure, it increases

* Corresponding author
Email: tasorenekrem@gmail.com

European Mechanical Science (2021), 5(4): 177-182
doi: https://doi.org/10.26701/ems.962605
Received: July 5, 2021
Accepted: September 8, 2021

the oxygen content of gasoline when added to gasoline [8]. 2-Propanol is a colorless, flammable, organic compound. 2-Propanol is well mixed with many solvents, including water. It is a volatile chemical 2-Propanol fuel, also known as isopropanol [9].

In a study conducted by Keskin and Guru [9], gasoline fuel in a four-stroke spark plug ignition engine 4%, 8%, 12%, 16%, 20% added ethanol in its proportions. Additionally, 4%, 8%, 12%, 16%, and %20 2-Propanol was added to gasoline fuel. By experimenting with the resulting fuels, they investigated the effect of the engine on exhaust and noise emissions. As a result of the experiments, they stated that HC and CO emissions decreased and NOx and CO_2 emissions increased using fuels added 2-Propanol.

Altun et al. [10] 5% and 10% 2-Propanol were added to gasoline fuel in a spark plug engine. They investigated the effect of fuel blends on exhaust emissions. As a result of the study, CO and HC observed decreased emission values while CO_2 emissions increased.

In a study conducted by Mourad and Mahmoud [8], propanol was added to gasoline fuel in 5%, 10%, 15%, and 20% by volume. They evaluated the performance of a spark plug engine using fuel blends. Their results stated that particular fuel consumption decreased by about 2.84%, exhaust emissions decreased by 4.18% in HC values, and 10.87% in CO values.

Simsek et al. [6] their study first added 20% n-Propanol and 2-Propanol to gasoline fuel in a spark plug engine. In the second stage, they examined 1-3% hexane addition to previous fuels on engine performance and emissions. The emission results obtained stated a significant decrease in HC and CO emissions compared to gasoline fuel, there was no significant change in NO_X emissions, and there was an increase in CO_2 emissions.

In this study, changes in the exhaust emission values of a direct injection engine were examined by adding 2-Propanol by 5%, 10%, and 15% volumetric to gasoline fuel. In this study, researches were taken into consideration while determining the fuel blends. But there is no such study on direct injection engines. For this reason, it was increased up to 15% while preparing fuel blends.

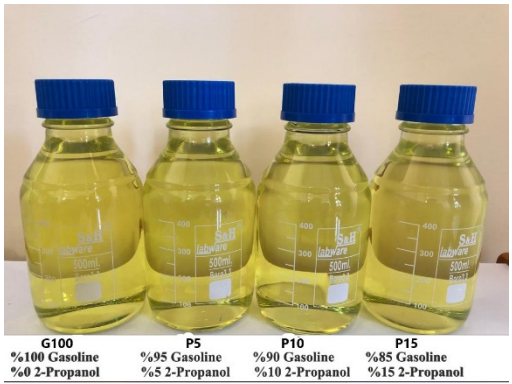

Figure 1. Test fuels

In addition, with this study, unlike other studies in the literature, the number of tests was reduced by using the Taguchi method, and the effects of 2-Propanol and engine speed values on each emission parameter were obtained as mathematical functions. Apart from this, the test intervals were visualized with contour graphics and it was determined at which ratios of 2-Propanol use was more appropriate according to the engine speed. This study comprehensively covers the effects of 2-Propanol and engine speed on emissions and forms a reference for future research.

6. MATERIAL AND METHOD

6.1. Fuel blends and Test Setup

Fuel blends were obtained by blend 2-Propanol supplied by Sigma Aldrich with 5% (P5), 10% (P10), and 15% (P15) gasoline by volume. In addition, 95 octane gasoline was used as a fuel for comparison. Fuel properties are given in Table 1 [3,9]. Test fuels are shown in Figure 1. During the experiment, the fuels were mixed continuously with a mechanical mixer. As a result, phase separation is prevented.

Table 1. Fuel properties [3,9]

Property	Gasoline	2-Propanol
Density (g/ml)	0.775	0.786
Flash Point (°C)	<-40	12
Autoignition Temperature (°C)	>250	425
Boiling Point	>32	82.6
Octane Number	95	95
Lower Heating Value (kJ/kg)	43430	31000

The tests were carried out under partial load using a 1.2 TSI direct injection, 4-stroke, and 4-cylinder gasoline engine, using the BT-190 FR hydraulic dynamometer at 1500, 2500, and 3500 rpm. Dynamometer properties are given in Table 2. The properties of the test engine are given in Table 3, and the experimental setup is given in Figure 2.

Table 2. Hydraulic dynamometer specifications

Feature	Capacity
Maximum Braking Power	100 kW
Maximum Speed	6000 rpm
Maximum Torque	750 Nm
Brake Water Working Pressure	0-2 kg/cm^2
Water Requirement for Maximum Power	2.3 m^3/h
Maximum Brake Water Outlet Temperature	80 °C
Torque Measurement	Electronic Load-Cell
Rotation Direction	Right and Left

Table 3. Test engine technical specifications

Feature	Property
Volume	1197 cm^3
Number of Cylinders	4
Compression Rate	10:1
Cylinder Diameter	71 mm
Stroke	75.6 mm
Maximum Power Output	77 kW (@5000 rpm)
Maximum Torque	175 Nm (@1500-3500)
Emission Standard	Euro 5
Control Unit	Continental Simos 10.1

For the measurement of exhaust emissions, the Bosch BEA350 model emission meter was used in the experiments. The specification values of the emission meter are given in Table 4.

Table 4. Emission meter specifications

Emission	Measure Range	Precision
CO	0 – 10 (%) volumetric	0.001%
CO_2	0 – 18 (%) volumetric	0.01%
HC	0 – 9999 ppm volumetric	1 ppm
NO_X	0 – 5000 ppm volumetric	1 ppm
O_2	0 – 22 (%) volumetric	0.01%

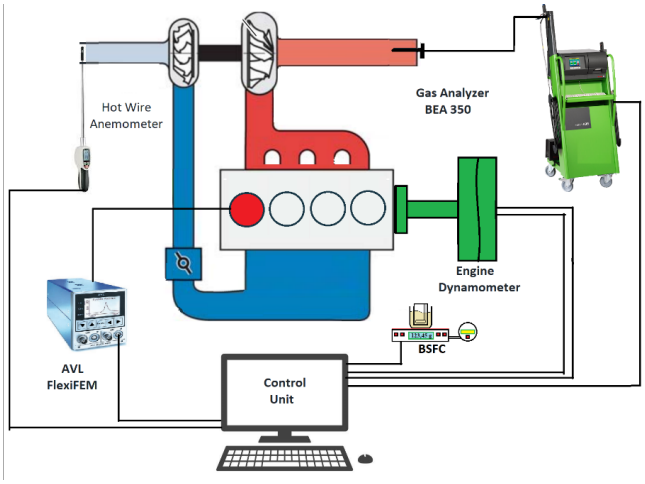

Figure 2. Experimental setup

6.2. Taguchi Experimental Design

Experimental design techniques (DoE), reducing costs by reducing the number of tests, determining input values at different levels (small, medium, most prominent, etc.) instead of performing tests in the whole range, only to investigate the effect of these values on the response values and to analyze the results mathematically depending on the estimation functions and used to express. Taguchi's experimental design technique is one of the DoE methods developed by Dr. Genichi Taguchi. In this study, 2-Propanol and engine speed were determined as input parameters, while CO, CO_2, HC, NO_X, and O_2 values were determined as output parameters. In table 4, the levels of input parameters are given.

Table 4. Taguchi method factors and level

Factors	Level 1	Level 2	Level 3
A-Engine Speed (rpm)	1500	2500	3500
B-2PR (% volume)	5	10	15

Unlike other statistical designs, the Signal/Noise (S/N) ratio is used in the Taguchi design. This parameter is calculated depending on the effect of the output values on the design (lowest best, highest best, nominal best). Since all output values were wanted to be the lowest in this study, the S/N ratio was calculated as given in Equation 1, with the Y output value, the I level, and n is the number of combinations at the O Level. In addition, the L9 orthogonal sequence was used depending on the levels of parameters and parameters, and a total of 9 measurements were made consisting of 3 levels of each input parameter and combinations of these levels. The measurement values were compared with the gasoline fuel values.

$$\frac{S}{N} = -10 log\left(\frac{1}{n}\sum_{i=1}^{n} y_i^2\right) \quad (1)$$

Different from traditional statistical mathematical approaches to obtain mathematical function of a test procedure as the test procedure to predict output values for input values that are not included in the prediction function y, β constant-coefficient, k the number of input factors, X to represent the input value and the standard error is given by equation 2, it is stated that[11]. Functions that cannot be explained linearly are expressed as I linear; J is given in equation 3 to represent the polynomial coefficient [12].

$$y = \beta_0 + \beta_1 X_1 + \beta_2 X_2 + \beta_k X_k + \in \quad (2)$$

$$y = \beta_0 + \sum_{i=1}^{k} \beta_i X_i + \sum_{i=1}^{k} \beta_{ii} X_i^2 + \Sigma \sum_{i<j}^{k} \beta_{ij} X_i X_j + \in \quad (3)$$

7. RESEARCH RESULTS AND DISCUSSION

Analysis of variance (ANOVA) ensures that non-repetitive combinations of output variables are associated with input parameters due to regression. ANOVA analysis includes factors such as R_2, R_{adj}^2, Test value F (F-value), probability value (P-value), as well as statistical factors such as exponential values of factors (A^2, B^2, A*B). In cases where the P-value is less than 0.05, the result is statistically significant. In addition, the fact that the F-value is significant increases statistical significance. R^2 values, a measure of the explainability of response values with input values, are above %97 for all emissions. In addition, in cases where there are two or more input parameters, R_{adj}^2 is used for benchmarking, and Anova results are given in Table 5 for all output values.

Table 5. ANOVA Table (A: Engine Speed (rpm) B:2-Propanol Rate (% Vol))

Parameter	CO		CO_2		HC		O_2		NO_X	
	P-Value	F- Value	P- Value	F- Value	P- Value	F- Value	P- Value	F- Value	P- Value	F- Value
A	0.0056	51.10	0.0033	73.40	0.0005	273.78	0.0146	26.02	0.0030	78.25
B	0.0506	10.03	0.0098	34.69	0.0000	1160.18	0.0000	1352.46	0.0079	40.20
A^2	0.9796	0.00	0.3213	1.40	0.0741	7.26	0.4388	0.79	0.9214	0.01
A*B	0.1283	4.35	0.5588	0.43	0.3751	1.08	0.1174	4.75	0.8892	0.02
B^2	0.0004	289.26	0.2881	1.66	0.0187	21.66	0.0006	227.05	0.5971	0.35
R^2	0.9916		0.9738		0.9997		0.9981		0.9753	
R_{adj}^2	0.9776		0.9301		0.9993		0.9950		0.9343	

In this study, the 2nd order functions obtained depending on the input parameters for CO, CO_2, HC, O_2, and NO_X are respectively (4), (5), (6), (7), and (8) are given in equations.

$$CO = -0.533639 - 0.019075 * 2PR + 0.000965833 * ES + 0.0000133333 * 2PR^2 + 0.00000355 * 2PR * ES - 2.04667E - 7 * ES^2 \quad (4)$$

$$CO_2 = 13.0219 - 0.0176667 * 2PR - 0.000256667 * ES - 0.00306667 * 2PR^2 + 0.000006 * 2PR * ES + 8.33333E - 8 * ES^2 \quad (5)$$

$$HC = 216.597 - 0.0833333 * 2PR - 0.0583333 * ES - 0.0733333 * 2PR^2 + 0.0001 * 2PR * ES + 0.00000316667 * ES^2 \quad (6)$$

$$O_2 = 4.56306 - 0.0504167 * 2PR - 0.002425 * ES + 0.000866667 * 2PR^2 + 0.0000075 * 2PR * ES + 3.66667E - 7 * ES^2 \quad (7)$$

$$NOx = 1456.71 - 9.83333 * 2PR - 0.00466667 * ES + 0.04 * 2PR^2 - 0.0002 * 2PR * ES - 0.0000055 * ES^2 \quad (8)$$

Test studies show a decrease in all emission values in proportion to the increased amount of 2-Propanol. In tests conducted at 1500 rpm, CO emissions decreased by 41.99% compared to gasoline, while CO_2, HC, NO_x, and O_2 emissions decreased by 7,09%, 20,91%, 8.64%, and 20.34%, respectively. 2500 rpm test, CO, CO_2, HC, O_2, and NO_x reductions in emissions, respectively 16.60%, 2.09%, 17.39%, 10.64%, and 27.14% 3500 rpm, while the rate of decrease of the emission test values, respectively 25.30%, 4.88%, 29.09%, 9.72%, and 37.09% has been found in. Test results are given in Table 6.

In Figure 3, contour graphs obtained for all emission values are given. Contour charts are essential for determining the most suitable conditions of use for output values. CO emission is an important parameter that shows the chemical energy formed in incomplete combustion and cannot be converted into heat energy. In cases where there is not enough air-fuel mixture in the combustion zone, the efficiency of the combustion event decreases, and CO is formed as a combustion product. When the CO graph is examined, it is seen that as the 2-Propanol ratio in the fuel blend increases, the CO values decrease. Due to the presence of oxygen in the structure of 2-propanol, the amount of oxygen taken into the cylinder increases. Therefore, combustion is considered to be more efficient. The results reported by Keskin and Guru, Mourad et al. [8,9] are similar to the results of the studies.

CO_2 gas is a colorless, harmless, and scentless gas. CO_2 emission is a parameter that's revealed during combustion and shows complete combustion. If there is enough O_2 in the combustion chamber, the fuel oxidizes, and the C atom in the fuel combines with O_2 to form CO_2 gas. When the CO_2 graph is investigated, it is seen that there is a decrease in CO_2 emission values due to the increase in the 2-Propanol ratio in the blend. Since 2-Propanol has fewer C atoms in its structure than gasoline, it is thought that CO_2 emissions are lower than gasoline [13].

HC emissions occur in combustion products because the fuel cannot oxide or the ignition temperature is unavailable [10]. HC emission exhibited behavior similar to the CO_2 emission value at lower engine speeds. The lowest HC emission values were obtained in P15 fuel at an engine speed of 3500 rpm.

O_2 emission exhibited behavior similar to CO_2 emission value at lower engine speeds. The lowest values for O_2 emission value were obtained in P15 fuel at 3500 rpm engine speed. O_2 emission is a vital parameter to see the oxygen consumed during combustion. In affluent mixing areas, O_2 further improves combustion. The measurement of O_2 emission shows at what rate the amount of oxygen is used during combustion [13]. An increase in the turbulence in the combustion chamber with the increase in engine speed, providing an ideal fuel-air blend, and thus better combustion, is seen as the reason for this decrease in O_2 emissions. In addition, it is seen that the O_2 emissions of the blends with 2-Propanol fuel are lower than the use of gasoline. Using these fuels is normal for the O_2 values to decrease due to the increase in

Table 6. Test results

Engine Speed (rpm)	Fuel	CO (% Vol)	CO_2 (% Vol)	HC (ppm)	NO_x (ppm)	O_2 (% Vol)
1500	Gasoline	0.412	12.97	153	1422	1.72
	P5	0.382	12.72	135	1396	1.6
	P10	0.335	12.37	129	1327	1.41
	P15	0.239	12.05	121	1299	1.37
2500	Gasoline	0.554	12.42	92	1419	0.70
	P5	0.545	12.86	89	1356	0.63
	P10	0.497	12.53	86	1312	0.59
	P15	0.462	12.16	76	1268	0.51
3500	Gasoline	0.328	13.11	55	1347	0.62
	P5	0.317	13.02	51	1317	0.47
	P10	0.262	12.97	46	1284	0.42
	P15	0.245	12.47	39	1216	0.39

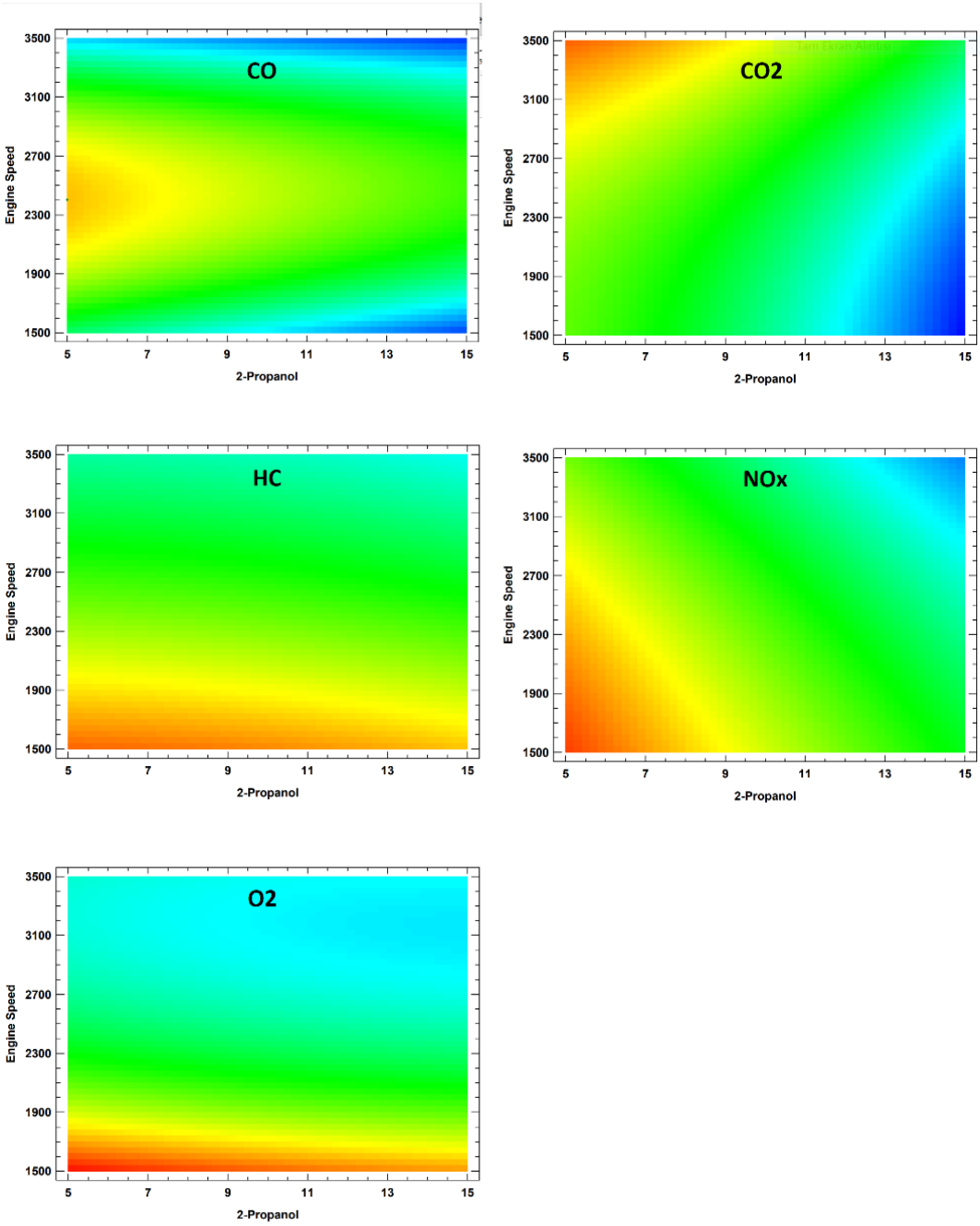

Figure 3. Contour charts for all emission values

the CO_2 value.

NO_X emissions occur when the nitrogen in the air is ionized and combined with oxygen as the temperature in the combustion chamber increases. Temperature, oxygen ratio, and combustion time are important parameters affecting NO_X emissions [2]. When the NO_X graph is examined, it is seen that NO_X values decrease as the engine speed increases. As the engine speed increases, the combustion event accelerates and the intake time shortens, and sufficient oxygen cannot be taken into the cylinders. Therefore, it can be expressed as the reason that NO_X formation decreases. In addition, the amount of NO_X emission decreases with the increase of the 2-Propanol ratio in the blended fuels. As seen in Table 1, the lower heating value of 2-Propanol is lower than that of gasoline. As a result, it leads to a lower combustion end temperature in the cylinder [2,14]. As a result of this situation, it is thought that there is a decrease in the number of NO_X emissions. While NO_X emission is at its highest value up to 2700 rpm engine speed and approximately 9% 2-Propanol, it decreases with increasing engine speed and 2-Propanol ratio. NO_X emission reaches its lowest value at 3500 rpm engine speed and P15 fuel.

8. CONCLUSION

In this study, the effect of gasoline fuel mixtures containing 5%, 10%, and 15% 2-Propanol on exhaust emissions at 1500, 2500 and 3500 rpm engine speeds using 1197 cc, 1.2 TSI engine was investigated experimentally and statistically. Taguchi method was used for experimental designs. Engine speed (rpm) and 2-Propanol (%) ratios were determined as input parameters and emission values as output param-

eters. Nine tests were performed for every three levels of input parameters, and these tests were compared with 100% gasoline. As a result of the study, emission values in 2-Propanol-gasoline fuel blends decreased at all engine speeds. 2-Propanol has a lower heating value compared to gasoline, lowers the combustion temperature, and reduces emission. In addition, the OH group in its chemical structure is connected to water molecules in the fuel by hydrogen bonding, and the methyl groups are connected to gasoline by dipole bonds, forming an excellent blend and contributing to the reduction of CO_2, CO, and HC emissions. With increasing engine speed, the amount of O_2 per unit fuel decreases proportionally. This study obtained mathematical functions depending on the input parameters for all emission values and shown with contour graphs. The Taguchi approach in internal combustion engine tests is of great economic benefit by reducing the number of experiments, time, and material used. In addition, as a result of the study using the Taguchi approach, an approximate estimation of unknown input parameters is possible by obtaining prediction functions.

Symbols and Abbreviations

G Gasoline

P5 95% Gasoline + 5% 2-Propanol

P10 90% Gasoline + 10% 2-Propanol

P15 85% Gasoline + 15% 2-Propanol

2PR 2-Propanol

HC Hydrocarbon (ppm)

CO Carbon monoxide (% by volume)

CO_2 Carbon dioxide (% by volume)

NO_x Nitrous oxide (ppm)

O_2 Oxygen (% by volume)

REFERENCES

[1] Tosun, E., Ozgur, T., Ozgur, C., Ozcanli, M., Serin, H., Aydin, K., (2017), Comparative analysis of various modeling techniques for emission prediction of diesel engine fueled by diesel fuel with nanoparticle additives. European Mechanical Science 1(1): 15–23, Doi: 10.26701/ems.320490.

[2] Tosun, E., Özcanlı, M., (2021), Hydrogen enrichment effects on performance and emission characteristics of a diesel engine operated with diesel-soybean biodiesel blends with nanoparticle addition, Engineering Science and Technology, 24: 648-654, Doi: 10.1016/j.jestch.2020.12.022.

[3] Imdadul, H.K., Masjuki, H.H., Kalam, M.A., Zulkifli, N.W.M., Alabdulkarem, A., Rashed, M.M. Teoh, Y.H., How, H.G., (2016), Higher alcohol-biodiesel-diesel blends: An approach for improving the performance, emission, and combustion of a light-duty diesel engine. Energy Conversion and Management 111: 174–185, Doi: 10.1016/j.enconman.2015.12.066.

[4] Atmanli, A., (2016), Comparative analyses of diesel-waste oil biodiesel and propanol, n-butanol or 1-pentanol blends in a diesel engine. Fuel 176: 209–215, Doi: 10.1016/j.fuel.2016.02.076.

[5] Yusoff, M.N.A.M., Zulkifli, N.W.M., Masjuki, H.H., Harith, M.H., Syahir, A.Z., Kalam, M.A., Mansor, M.F., Azham, A., Khuong, L.S., (2017), Performance and emission characteristics of a spark-ignition engine fuelled with butanol isomer - gasoline blends. Transportation Research Part D: Transport and Environment 57, 23 – 38, Doi: 10.1016/j.trd.2017.09.004.

[6] Şimşek, D., Oral, F., Çolak, N., (2019), The effect on engine performance and emissions of gasoline-propanol-hexane fuel blends on single-cylinder spark-ignition engines, Journal of Thermal Science and Technology, 39 (1), 81-89.

[7] Şimşek, D., Çolak, N.Y., Oral, F., (2018), Buji Ateşlemeli motorlarda kullanilan n -propanol ve izo-propanol / benzin yakit karişimlarinin performans ve emisyonlara etkisi, Bitlis Eren Üniversitesi Fen Bilimleri Dergisi, 7 (2): 409–416.

[8] Mourad, M., Mahmoud, K.R.M., (2018), Performance investigation of passenger vehicle fueled by propanol/gasoline blend according to a city driving cycle, Energy 149: 741–749, Doi: 10.1016/j.energy.2018.02.099.

[9] Keskin, A., Gürü, M., (2011), The effects of ethanol and propanol additions into unleaded gasoline on exhaust and noise emissions of a spark-ignition engine. Energy Sources, Part A: Recovery, Utilization and Environmental Effects 33(23): 2194–2205, Doi: 10.1080/15567030903530558.

[10] Altun, Ş., Öner, C., Firat, M., (2010), Exhaust emissions from a spark-ignition engine operating on isopropanol and unleaded gasoline blends, Technology, 13(3), 183-188.

[11] Anderson-Cook, C.M., Borror, C.M., Montgomery, D.C., (2009), Rejoinder for "Response surface design evaluation and comparison", Journal of Statistical Planning and Inference 139(2): 671–674, Doi: 10.1016/j.jspi.2008.04.009.

[12] Montgomery, D.C., (2006), Design and Analysis of Experiments, Publisher: John Wiley & Sons, Inc.111 River Street Hoboken NJ United States, ISBN:978-0-470-08810-4.

[13] Uludamar, E., Yildizhan, Ş., Aydin, K., Özcanli, M., (2016), Vibration, noise and exhaust emissions analyses of an unmodified compression ignition engine fuelled with low sulfur diesel and biodiesel blends with hydrogen addition. International Journal of Hydrogen Energy 41(26): 11481–11490, Doi: 10.1016/j.ijhydene.2016.03.179.

[14] Akar, M.A., Bas, O., Ozgur, T., Ozcanli, M., (2018), Effect of bioethanol blending with gasoline on emissions characteristics with spark plug alteration for SI engine. Journal of Biotechnology 280: S90, Doi: 10.1016/j.jbiotec.2018.06.296.

EUROPEAN MECHANICAL SCIENCE
e-ISSN: 2587-1110

Research Paper

Investigation of the Influence of Cold-Treatment on Properties of Advanced High Strength Automotive Steels

Büşra Karaoğlu[1], Ramazan Kaçar[2*], Hayriye Ertek Emre[3], Samet Nohutçu[4]

[1]Graduate School of Natural and Applied Science/Karabuk University /Turkey
[2-4]Karabuk University/Manufacturing Engineering Department/Turkey

Abstract

Due to the moderate formability of high strength low alloy steels (HSLA), the steels called transformation induced plasticity (TRIP) have been developed. They are especially used in the production of automobile shock absorbers and the beam supporting parts. The microstructure of these steels consists of the distribution of ferrite, bainite and (5 - 10%) residual austenite phases. The strength and formability of steels are generally provided by bainite, ferrite and the residual austenite phases in the structure. During shaping, the residual austenite turns into martensite and gives high strength to the steel. Considering the literature studies, it is pointed out that there is a lack of information about the effect of cold treatment on TRIP steels. For this reason, in the study, cold treatment performed to the TRIP800 steel for two hours at various temperatures. Thus, the mechanical properties and microstructure of the samples were examined in detail.

Key words: TRIP steels, Cold treatment, Mechanical properties, Microstructure

1. INTORDUCTION

The formability of commercial low ductility high strength steels decreases almost linearly due to the increased strength. However, advanced high strength steels are characterized by their combination of strength and formability. Due to their sought and desired properties, these steels to be use in a wide range of industries [1,2]. One of the advanced high strength steel varieties developed for industrial applications and especially for automotive production is TRIP steels, which means plasticity caused by transformation [3-5]. Much research and improvements are being conducted in the automobile industry to improve their safety and fuel consumption performance [6,7]. As a result of these researches and developments, it is important that cars are designed and manufactured to be durable and safe when exposed to static, impact and variable loads [8-10]. TRIP steels are used in a wide range in the production of shock absorber and beam supporting parts of automobiles due to their high strength and formability [11]. De Cooman [12], reported that two types of high strength steels (< 1000 MPa and > 1200MPa) are needed for safety-based car body design. These are dual-phase (DP) and TRIP steels with a high energy absorption potential tensile strength below 1000 MPa, for dynamic loading occurring during car crashes or collisions [12,13]. When it comes to protecting vehicle passengers, the type of sheet material used as a load transfer barrier is specified as martensitic steels with a tensile strength over 1200MPa [12,13]. In summary, these advanced high strength steels are preferred and used for applications where high strength and ductility as well as excellent formability and weight savings are required [14,15].

In recent years, the effects of low-temperature processes on the properties of materials are remarkable. Low-temperature processes are called cold process (cold heat treatment or cold treatment) up to -80 °C (processes in dry ice), and those performed at liquid nitrogen temperature are called deep cryogenic processes. As stated in the study "Microstructure of cryogenically treated M2 tool steels" conducted by Huang et.al.[16]; many researchers point out that the cryogenic process increases the wear resistance of steels by providing the complete transformation of residual austenite to martensite. Another group of researcher claims that the cryogenic process improves the wear resistance by facilitating the formation of η-type carbides in martensite [17,18]. It is known that applications at low temperatures (cryogenic temperatures) significantly affect the mechanical properties of austenitic stainless steels by martensitic transformation. Powell et al. [19] and Hecker et al. [20] investigated the effects of strain rate and stress condition on strain-based martensite formation and mechanical properties on austenitic stainless steel. The effect of temperature and strain on the martensi-

* Corresponding author
Email: rkacar@karabuk.edu.tr

European Mechanical Science (2021), 5(3): 183-188
doi: https://doi.org/10.26701/ems.830012
Received: November 23, 2020
Accepted: February 23, 2021

tic transformation was indicated by Powell [19] while, the martensite ratio under multiaxial loading was determined by Hecker et.al. [20] Yoo et al. [21], investigated the dynamic loading structural analysis of advanced high strength materials performed at low temperatures and simulated the temperature and strain rate change of TRIP steels in low temperature applications. They pointed out that advanced high strength materials also show extreme sensitivity depending on the stress rate and temperature [21]. Additionally, the experimental results simulated with the proposed numerical model revealed that TRIP steels exhibit nonlinear material properties at low temperature [21].

Literature research points out to a lack of knowledge about the effect of low service temperatures on the properties of TRIP steels. For this reason, in the study; TRIP800 steels were cold heat treated at various temperatures for two hours. Then, microstructure and mechanical properties of samples were examined in detail after bringing them to room temperature.

2. MATERIAL AND METHOD

2.1. Material:

The chemical content (% weight) of TRIP800 steel, which is commercially supplied in 1000 x 1500 x 1.5 mm dimensions, is given in Table 1.

Table 1. Chemical composition of TRIP800 grade steel

Element (% weight)	C	Si	Mn	P	S	Cr	Mo	Al	Fe
TRIP800	0,22	1,576	1,619	0,013	0,003	0,016	0,014	0,036	Remain

2.2. 2.2 Preparation of Experimental Test Samples:

The tensile test specimens in accordance with the TS EN ISO 6892-1 standard were obtained by using the press cutting die for determining mechanical properties.

In order to assess effect of the cold treatment on mechanical properties of TRIP800 steel, the test samples were kept in groups of different temperatures at 0 °C, -20 °C and -50 °C for two hours, respectively. The tensile tests were applied after the samples were brought to room temperature in open atmosphere conditions. A group of samples were also tested at room temperature (25 °C) without any cold treatment for comparison. Tensile tests were carried out in a device of SHIMAZDU with a capacity of 50 kN at a strain rate of 2 mm/min. To minimize the experimental errors, a set of three tensile test samples were tested for each condition. In addition, hardness measurement was carried out by applying a load of 500 g in the Vickers microhardness tester.

Metallography samples were molded with cold resin and then prepared by using classical metallography methods for structural evaluation. The samples were etched with 2% nitric acid solution. Carl Zeiss Ultra Plus Fe-SEMs brand scanning electron microscope (SEM) and EDS analysis system were used to examine the microstructure and fracture surfaces.

3. RESULTS AND DISCUSSION

3.1. Tensile Tests:

The mean yield and tensile strength, elongation amount and breaking point are given in Table 2 for TRIP800 steel, which is cold processed for two hours at various temperatures. The mean stress-strain curves are shown in Figure 1.

Table 2. Mechanical properties of TRIP800 steel cold heat treated at various temperatures.

Holding temperature (°C)	Yield strength (N/mm²)	Tensile strength (N/mm²)	Elongation (%)	Breaking point
-50	570	867	33	
-20	560	870	32	
0	555	872	32	
25	540	903	30	

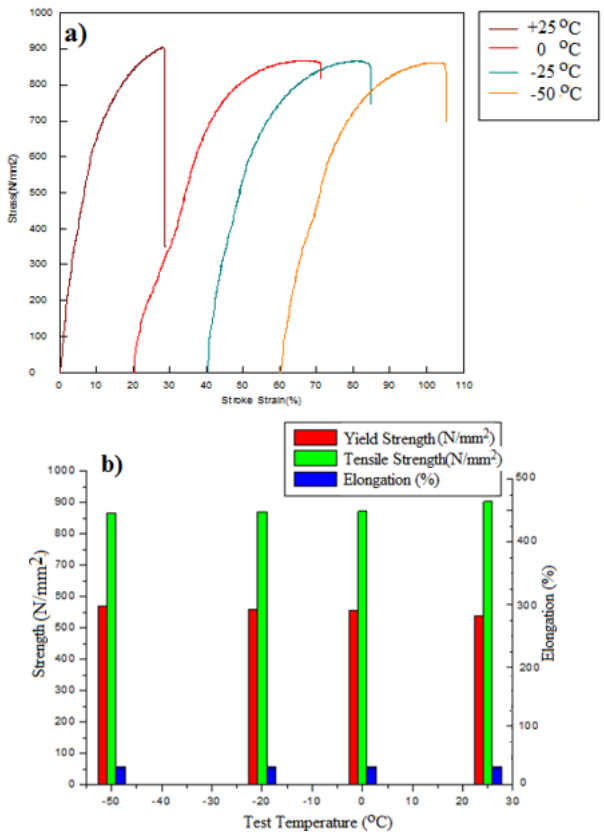

Figure 1. Cold heat treatment of TRIP800 steel at various temperatures; a) stress-strain curves, b) The graphical representation of yield, tensile strength, and elongation versus cold treatment temperature.

As seen from Table 2 and Figure 1; the mechanical proper-

ties of TRIP800 steel, the yield strength, tensile strength and elongation of the TRIP800 steel were determined. It has been found that cold treatment has no significant effect on the tensile strength and formability of TRIP800 steel. However, the cold treatment causes an increase in the yield strength of the steel depending on decreasing the temperature. It was determined that the yield strength of TRIP800 steel was 540N / mm^2 at room temperature and increased to 570N / mm^2 in the sample that was cold processed at -50 °C. The yield strength of steels is significantly affected by temperature [22]. In this study, the yield strength of TRIP800 steel samples increased approximately 30N / mm^2 with the decreasing cold treatment temperature.

The relationship between yield strength and cold treatment temperature can be explained by the change in a volumetric ratio of phases in the microstructure of TRIP steel. The general structure of TRIP steel has the majority of ferrite and bainite phases (about 85%) and the minority of the residual austenite phase (about 15%) as well as martensite transformed by residual austenite. Increasing on the yield strength of the TRIP800 steel by decreasing cold treatment temperature can attribute to strain induced martensitic transformation and the dominant role of ferrite and bainite phases in the structure. In a study, Wang et al. [23] investigated the relationship between yield and tensile strength and temperature of TRIP steel at temperatures between 20 °C and –40 °C. It has been reported that the yield strength of steel increases with decreasing temperature down to -5 °C, then decreases down to -20 °C, and increases again as it goes down to temperatures lower than -20 °C. This anomalous event at -5 °C is explained as the transition point from stress-induced martensitic transformation to strain-induced martensitic transformation. In the temperature range between -5 °C and -20 °C, it is reported that the onset of martensitic transformation due to tensile stress in the elastic region leads to regional softening in residual austenite and causes a decrease in yield strength [23]. However, it is noted that below -20 °C yield strength increases with decreasing temperature, with the same tendency as the temperature range of 20 °C to -5 °C. This effect is attributed to the dominant role of ferrite and bainite phases in the structure [23].

Moreover, martensite formation under stress has been reported to produce more effective strain stiffness than ordinary shear in the face center cubic austenite phase [24]. From the above analyzes, it is stated that the martensitic transformation in TRIP steel causes stress redistribution by the strain hardening and uniform elongation effect. It is also believed that the martensitic transformation from residual austenite can relax the stress accumulated in ferrite and bainite around the austenite. This stress relief may be responsible for the slight change in hardness at cold treatment temperatures.

In the study, fracture surface images of tensile test samples of TRIP800 steel tested at ambient temperature after cold treatment at various temperatures were examined. The fractured surface image of the samples tested at room temperature and -50 °C temperature are shown in Figure 2 and Figure 3, respectively.

Dimples on the surface indicates the ductile fracture while, planar regions indicate brittle fracture modes. As seen Fig.2 and 3, the fracture surfaces of the test specimens show that the damage is generally caused by the semi ductile-semi brittle fracture behavior. The formations of secondary phase

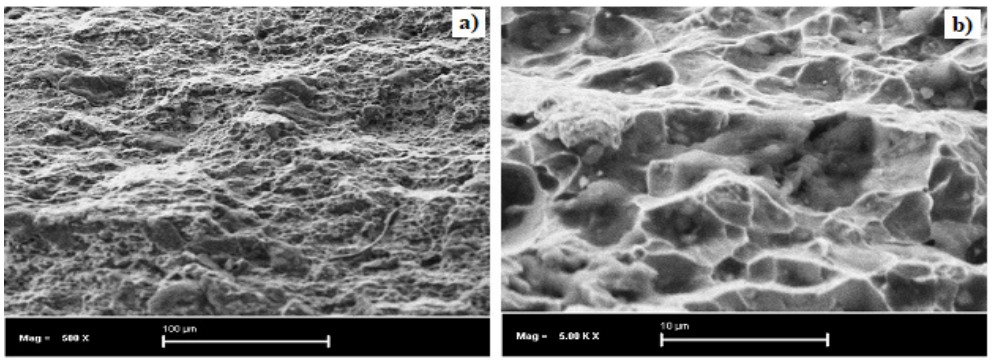

Figure 2. Fracture surface image of TRIP800 steel tested at 25 °C a) lower magnification b) higher magnification

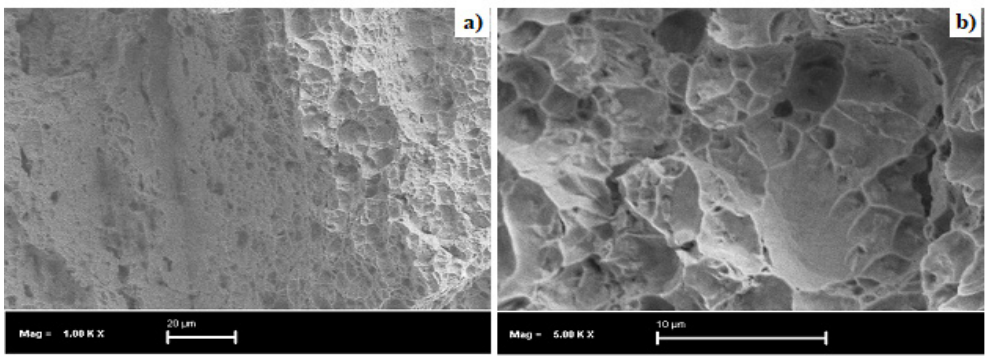

Figure 3. Fracture surface image of TRIP800 steel cold-treated at -50 °C a) lower magnification b) higher magnification.

particles, which are thought to be metal carbides inside the dimples, are responsible for the onset of fracture has been tried to be determined. For this purpose, point EDS analysis were taken from the fracture surfaces of the sample tested at room temperature and the result is shared in Figure 4.

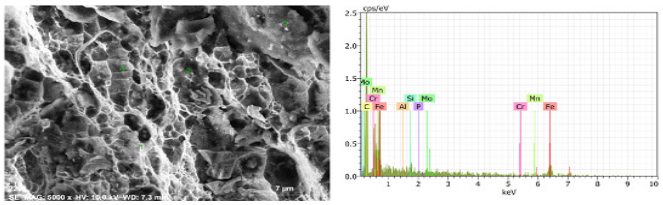

Mass percent (%)

Spectrum	C	Al	Si	P	Cr	Mn	Fe	Mo
1	20.80	0.35	1.79	0.00	0.00	1.53	75.46	0.07
2	51.07	0.29	1.41	0.13	0.04	1.14	44.85	1.07
3	94.78	2.65	0.31	0.04	0.00	0.41	1.82	0.00
4	21.20	0.00	0.95	0.00	0.00	1.89	75.97	0.00
Mean value:	46.96	0.82	1.11	0.04	0.01	1.24	49.52	0.29
Sigma:	34.89	1.23	0.64	0.06	0.02	0.64	34.97	0.52
Sigma mean:	17.44	0.61	0.32	0.03	0.01	0.32	17.49	0.26

Figure 4. EDS analysis result of TRIP800 steel fracture surface tested at 25 °C

As seen from Figure 4, the higher amount of Fe, Mo and C elements presence in EDS analysis results indicate the possibility of carbide formation in TRIP 800 steels. As a result of analysis, (Fe and Mo) C carbide formations in TRIP800 steel form the precursor for the initiation of fracture. It is reported that Fe_4M_2 (M = W, Mo, Cr, V) C carbide formations occur in steels with or without cryogenic treatment [16].

3.2. Hardness Measurement:

In the study, the results of hardness measurement performed on samples that were cold treated for two hours at various temperatures are graphically shown in Figure 5.

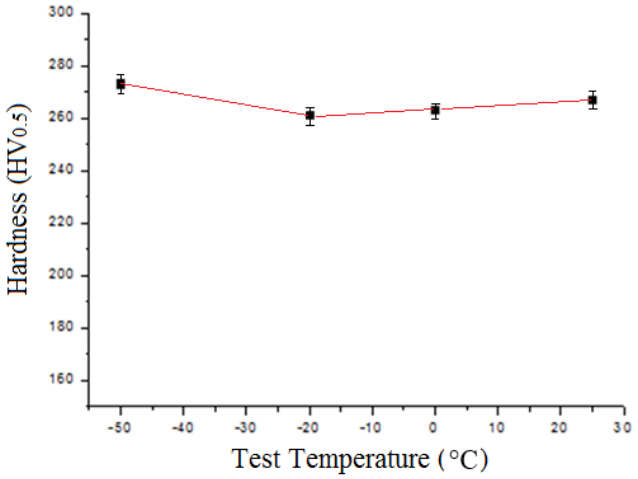

Figure 5. Hardness profile of TRIP800 steel cold treated at various temperatures.

As seen in Figure 5; the hardness of TRIP800 steel which is consisting of bainite and residual austenite phases in a ferrite matrix was measured in the range of 261±2 - 273±2 $HV_{0.5}$ on average. The lowest hardness was measured in the cold treated sample at the temperature of -20 °C while, the highest hardness was measured in the cold treated sample at the temperature of -50 °C. The close results indicate that the hardness of TRIP800 steel is not significantly affected by cold treatment. As mentioned earlier, residual stress that occur in the ferrite and bainite phases arising from the production process in TRIP800 steel may be responsible for the slight change in hardness at cold treatment temperatures.

3.3. Microstructure Evaluation:

The microstructure images of TRIP800 steel, which was cold heat treated for two hours at various temperatures, are shown in Figure 6.

Its microstructure consists of bainite and residual austenite phases dispersed in the ferrite matrix. Responsible for the higher strength, formability, and uniform elongation of TRIP800 steel are the bainite, ferrite phases and martensite phase formed by the transformation of the residual austenite, respectively.

As seen from Figure 6d; because of cold treatment at -50°C, no significant structural change was detected in the microstructure of TRIP800 steel. However, the following situation should not be ignored. The structural transformation of steels with martensite transformation finishing temperature below room temperature is completed, especially with the increase in martensite volume ratio. For this reason, it is thought that the decrease in the volume ratio of residual austenite phases in the ferrite matrix in the structure of steel is replaced by an increase in the amount of martensite.

In recent years, it has been stated that cryogenic heat treatment application suppresses dynamic recovery in aluminum alloys and increases dislocation density, which are responsible for development of ultra-fine grain structure in the material thus increases the strength [25]. However, considering the cold treatment temperature and application time applied to TRIP800 steel in this study, ultra-fine grains formation cannot be expected in the structure. In addition, the slight change in TRIP800 steel hardness at the specified temperatures may be related to factors such as loosening of residual stresses, coarsening of martensite, reduction of dislocation density, segregation of carbon and alloying element atoms and carbide precipitate formation.

There is uncertainty as to how cold treatment affects carbide formation in martensite. However, it is stated by Huang et al. [16] that two issues come to the fore in this regard. In the first one, lowering the M_S initial temperature for the transformation from austenite to martensite, and the second, waiting for sufficient time at this temperature are specified as requirements for high carbide formation. Crystal discontinuity such as dislocation and twinning cause microscopic residual stresses during cooling. These stresses cause changes in microstructure. It is stated that this leads to different thermal shrinkage and the transformation of residual austenite to martensite [16]. The martensite must be cooled below a certain temperature to create residual stress and sufficient crystalline defects. It is stated that the long holding time at the specified temperature may cause local diffusion process, causing the carbon and alloy atoms to cluster and

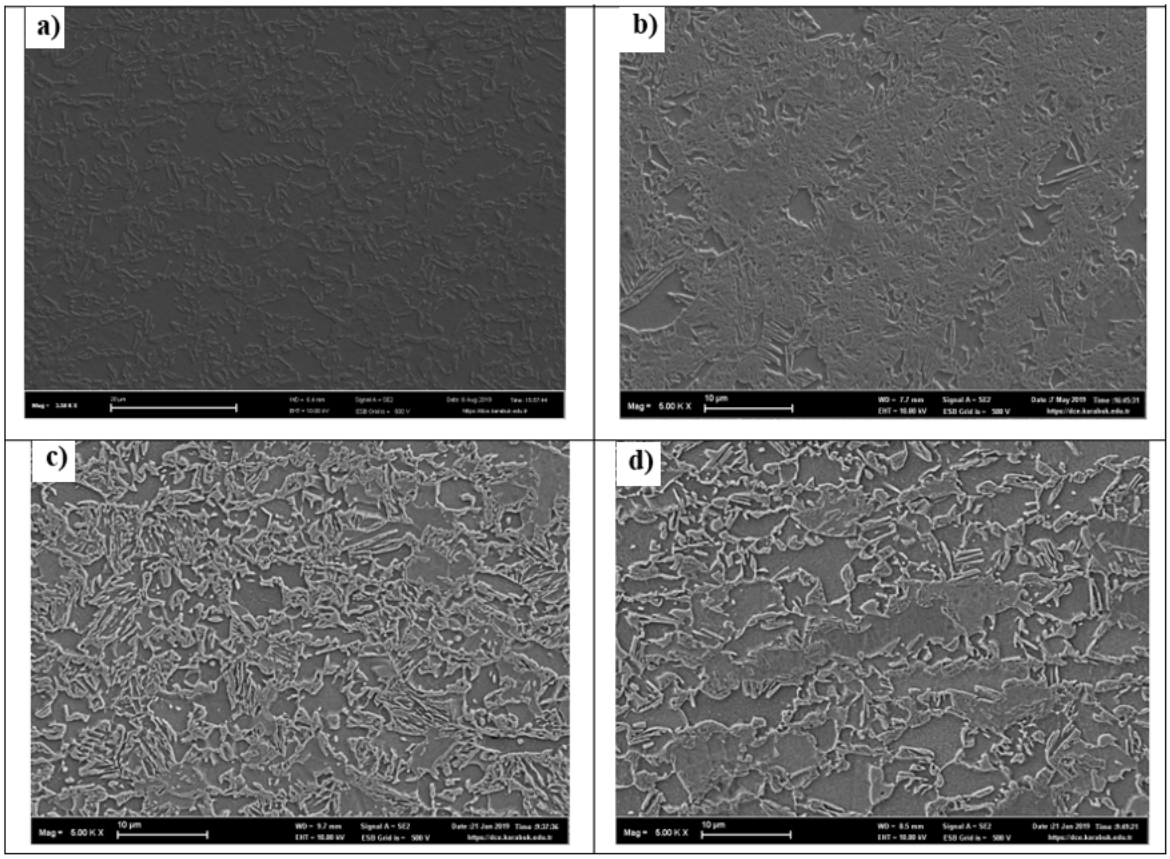

Figure 6. Microstructure of cold heat treated TRIP800 steel at different temperatures a) +25°C, b) 0°C, c) -20°C, d) -50°C.

cause crystal defects. With decreasing temperature, martensite reaches oversaturation, causing increased distortion and thermodynamic instability in the crystal lattice [16]. These two conditions cause the segregation of carbon and alloy atoms as well as defects. This aggregation of carbon and alloy atoms enables carbide nucleation and growth during the subsequent reheating or tempering process to room temperature [16].

The crystal defects density in the structure consisting of martensite is also very high. It is very difficult to observe in practice the segregation of carbon and alloy atoms as well as defects during the cryogenic process. However, neutron diffraction analysis in Huang's study indicates that the lattice parameters "a" and "c" differ during the cooling and reheating of the martensite phase [16]. The lattice parameter "a" varies almost linearly with temperature. The same graphic formation during heating and cooling indicates pure thermal elastic effect. However, the lattice parameter "c" decreases first during cooling, but it increases very slowly while warming [16]. This situation leads to the conclusion that carbon atom segregation is in the cold treatment. The carbon atom is generally in octahedral or tetrahedral places in the martensite phase. It has been reported that the segregation of carbon atoms from octahedral or tetrahedral locations to places with crystal defects mainly affects the "c" lattice parameter [16].

It is thought that the two hours cold treatment at the temperatures of -20 °C and -50 °C can cause clustering and segregation of carbon and alloy atoms in TRIP800 steel, which contains enough residual stress due to the production process. In addition, it is believed that cold treatment causes more crystal defects such as dislocation and twinning. It is thought that the carbides that will form when the TRIP800 steel is warming up to room temperature after the cold treatment applied, reduce the amount of carbon and alloying elements in the matrix and causes a slight change in hardness because of stress relief.

4. CONCLUSION

The effects of cold heat treatment applied at various temperatures on the properties of TRIP800 steels were investigated. The findings obtained from the samples tested at ambient temperature after cold treatment can be summarized as follows.

- It was determined that the decreasing cold treatment temperature of TRIP800 steel did not create a significant change in tensile strength and ductility but its increased yield strength.
- The fracture surfaces examination of the tensile test specimens indicates semi ductile-semi brittle fracture behaviour. The formations of secondary phase particles, which are metal carbides, inside the dimples are thought to be responsible for the onset of fracture.
- The hardness of TRIP800 steel, which consists of bainite and residual austenite phases in a ferrite matrix, was measured in the range of 261-273 HV0.5. The lowest

hardness was found in the sample cold treatment at -20 °C, the highest hardness was measured in the cold treated sample at -50 °C. The residual stress may be responsible for the slight change in hardness. It is believed that the carbides that form when the TRIP800 steel is warming up to room temperature after the cold treatment applied, reduce the amount of carbon and alloying elements in the matrix thus causes a slight change in hardness as a result of stress relief.

- TRIP800 steel consists of bainite and residual austenite phases dispersed in ferrite matrix. Because of cold treatment up to -50°C, no significant microstructural change was detected in the microstructure of TRIP800 steel. However, it is thought that the decrease in the volume ratio of residual austenite phases in the ferrite matrix in the structure of steel is replaced by an increase in the amount of martensite.

ACKNOWLEDGEMENTS

This study was supported by the Scientific Research Projects Unit of Karabük University with the project code number FYL-2019-2021. We would like to thank for their support.

REFERENCES

[1] Chiyatan T., Uthaisangsuk V. (2020). Mechanical and fracture behavior of high strength steels under high strain rate deformation: Experiments and modelling Materials Science and Engineering A, 779, 27, 139125, DOI: 10.1016/j.msea.2020.139125.

[2] Spena PR, Cortese L., Nalli F., Májlinger K. (2019). Local formability and strength of TWIP-TRIP weldments for stamping tailor welded blanks (TWBs). The International Journal of Advanced Manufacturing Technology,101, 757–771, DOI:10.1007/s00170-018-2946-1.

[3] Krizan D. (2006). TRIP Steels: Advanced high strength multiphase steels for automotive applications. 14th International Scientific Conference CO-MAT-TECH, Trnava, Slovak Republic.

[4] Kapustka, N., Conrardy, C., Babu, S., Albright, C. (2008). Effect of GMAW process and material conditions on DP 780 and TRIP 780 welds. Welding Journal, 87(6):135-148.

[5] Yinghui, Z., Yonli, M., Yonglin, K., Hao Y. (2006). Mechanical properties and microstructure of TRIP steels produced using TSCR process. Journal of University of Science and Technology, 13(5):416-421, DOI: 10.1016/S1005-8850(06)60084-4.

[6] Piccinia, J., Svobodaa, H. (2012). Effect of the plasma arc welding procedure on mechanical properties of DP700 steel. 11th International Congress on Metallurgy & Materials SAM/CONAME, Procedia Materials Science, p.50 – 57.

[7] Wu, D., Zhuang, L., Hui-sheng, L. (2008). Effect of controlled cooling after hot rolling on mechanical properties of hot rolled TRIP steel. Journal of Iron and Steel Research International, 15 (2):65-70, DOI: 10.1016/S1006-706 X (08)60034-5.

[8] Schmitt, JH., Iung, T. (2020). New developments of advanced high-strength steels for automotive applications. Comptes Rendus Physique 19 (8): 641-656, DOI: 10.1016/j.crhy.2018.11.004.

[9] Nayaka, S.S., Baltazar Hernandeza, V.H., Okitaa, Y., Zhou, Y. (2012). Microstructure–hardness relationship in the fusion zone of TRIP steel welds. Materials Science and Engineering A, 551:73– 81, DOI: 10.1016/j.msea.2012.04.096.

[10] Ding, H., Song, D., Tang, Z., Yang, P. (2011). Strain hardening behavior of a TRIP/TWIP steel with 18.8% Mn. Material Science and Engineering A, 528(3): 868-873, DOI: 10.1016/j.msea.2010.10.040

[11] Pal, T.K., Chattopadhyay, K. (2010). Resistance spot weldability and high cycle fatigue behavior of martensitic (M190) steel sheet. Fatigue and Fracture of Engineering Materials and Structures, 34(1):46-52, DOI: 10.1111/j.1460-2695.2010.01489.x

[12] De Cooman, B.C. (2004). Structure-properties relationship in TRIP steels containing carbide-free bainite. Current Opinion in Solid State and Materials Science, 8(4):285-303, DOI: 10.1016/j.cossms.2004.10.002.

[13] Kuziak, R., Kawalla, R., Waengler, S. (2008). Advanced high strength steels for automotive industry. Archives of Civil and Mechanical Engineering, 8(2): 103–117. DOI:10.1016/s1644-9665(12)60197-6

[14] Hilditch, T.B., De Souza, T., Hodgson, P.D. (2015). Properties and automotive applications of advanced high-strength steels (AHSS). Welding and Joining of Advanced High Strength Steels (AHSS), 9–28. DOI:10.1016/b978-0-85709-436-0.00002-3.

[15] Kučerová, L., Bystrianský, M. (2017). Comparison of thermo-mechanical treatment of C-Mn-Si-Nb and C-Mn-Si-Al-Nb TRIP steels. Procedia Engineering, 207:1856–1861, DOI: 10.1016/j.proeng.2017.10.951.

[16] Huang, J.Y., Zhu, Y.T., Liao, X.Z., Beyerlein, I.J., Bourke, M.A., Mitchell, T.E. (2003). Microstructure of cryogenic treated M2 tool steel. Materials Science and Engineering A, 339(1): 241-244, DOI:10.1016/S0921-5093(02)00165-X.

[17] Meng, F.J., Tagashira K., Azuma R., Sohma H. (1994). Role of etacarbide precipitations in the wear resistance improvements, ISIJ International 34, 205.

[18] Y. Dong, X.P. Lin, H.S. Xiao (1998). Deep cryogenic treatment of high speed steel and its. Mechanism, Heat Treatment of Metals 3, 55-59.

[19] Powell, G.W., Marshall, E.R., Backofen, W.A. (1958) Strain hardening of austenitic stainless steel. ASM Transactions Quarterly, 50:478–497.

[20] Hecker, S.S., Stout, M.G., Staudhammer, K.P., Smith, J.L. (1982). Magnetic measurements and mechanical behavior. Metallurgical and Materials Transactions A 13(4): 619–626, DOI: 10.1007%2FBF02644427.

[21] Yoo, S.W., Lee, C.S., Park, W.S., Kim, M.H., Lee,, J.M. (2011). Temperature and strain rate dependent constitutive model of TRIP steels for low-temperature applications. Computational Materials Science, 50(7):2014–2027, DOI: 10.1016/j.commatsci.2011.02.002.

[22] Wang, W., Liu, B., Kodur, V. (2013). Effect of temperature on strength and elastic modulus of high-strength steel. J. Mater. Civ. Eng. 25:174-182, DOI: 10.1061/(ASCE)MT.1943-5533.0000600

[23] Wang, X.D., Huang, B.X., Rong, Y.H., Wang L. (2006). Microstructures and stability of retained austenite in TRIP steels. Materials Science and Engineering A, 438-440:300-305, DOI: 10.1016/j.msea.2006.02.149.

[24] Kulin, S.A., Cohen, M., Averbach, B.L (1952). Effect of Applied stress on the martensitic transformation, Trans. AIME, 4:661-668, DOI:10.1007/BF03397742.

[25] Nageswararao, P., Kaurwar, A., Singh, D., Jayaganthan, R., (2014). Enhancement in strength and ductility of Al-Mg-Si alloy by cryo-rolling followed by warm rolling. Procedia Engineering, 75:123–128, DOI: 10.1016/j.proeng.2013.11

EUROPEAN MECHANICAL SCIENCE
e-ISSN: 2587-1110

Research Paper

Design and Manufacturing of a Pneumatic Driven Compression Spring Fatigue Machine

Fatih Özen[1*], Ufuk Dam[2], Muhammet Kaan Çobanoğlu[2], Erdinç İlhan[3], Salim Aslanlar[4]

[1]Department of Metallurgical and Materials Engineering, Faculty of Technology, Sakarya University of Applied Sciences, Batman, Turkey
[2]Atasan Metal San. Tic. Ltd. Şti., 1. Organized Industrial Zone, 2. Street, No:15, Arifiye, 54580, Sakarya, Turkey
[3]Department of Machinery and Metal Technologies, Sakarya Vocational School, Sakarya University of Applied Sciences, 54290, Sakarya, Turkey
[4]Department Department of Metallurgical and Materials Engineering, Faculty of Technology, Sakarya University of Applied Sciences, Sakarya, Turkey

Abstract

The fatigue life of springs is an issue that has not been studied in detail and is of high importance. Damage to the springs during operation can cause major irreversible damages. Since the microstructural properties and multiple parameters affects fatigue life of the springs to a high degree, fatigue analysis with FEM and numerical analysis methods cannot give a clear result. It should be experimented with specially designed fatigue machines. In this study, a helical compression spring fatigue device simulating the real fatigue conditions was designed and produced. A compression tray have been designed in which 12 compression springs could be fasten together in order to achieve the average fatigue values under the same conditions. Machine design and pneumatic elements was determined in view of design calculations. Electrical control circuits and pneumatic system design was also studied in detail. Then, manufacturing of the designed machine was implemented.

Keywords: Compression springs, fatigue, spring fatigue.

1. INTORDUCTION

Springs are widely used in machinery, tools and equipment for many purposes such as energy storage and vibration damping. Prolonged vibration or oscillation and cycles induces crack propagation from the weak points on the spring. These crack initiations begin with the notch effect created by the external surface or the irregularities within the microstructure. As a result of the spring fatigue or unexpectedly ending its life, the machine can undergo irreversible damage to its dynamic structure [1].

Various techniques are used to calculate fatigue life of the springs during design. Some of them have been tried to calculate the spring life using the FEM (finite element method) method [2]. Other methods are various mathematical and numerical models that have been put forward [3, 4]. Although numerical models are used, there are various differences among these thecniques [5]. The main reason for the differences is due to outer and intrinsic factors such as microstructure characterization, surface hardness, surface roughness, application temperature and application frequencies [6, 7]. For this reason, simulating the fatigue of the springs in a real environment will give the most realistic result. Thus, irreversible damages can be prevented by determining the service life of the springs with the most accurate way [8].

Helical compression springs are among the most used spring types in the industry. This type of springs can be used in high-stress ranges where operating conditions are critical such as engines, pumps and valves [9]. The fatigue life of helical compression springs depends on many factors including the condition of the outer surface, surface roughness, internal structure of the material, discontinuities in the material, working load, capacity, and frequency [10]. Therefore, compression springs should be tested under real conditions.

There are many spring fatigue machine designs in the industry. However, no study has been encountered that determines the life of compression springs produced from high strength wires driven with a pneumatic system. Fatigue testing applied to multiple compression springs was not also coincided in the literature. In this study, a fatigue machine simulating the working conditions of compression springs was designed and produced. The operation and design of the mechanical, electrical, pneumatic systems of the machine were carried out. The working efficiency of the fatigue

* Corresponding author
Email: fatih.ozen@batman.edu.tr

European Mechanical Science (2021), 5(4): 189-193
doi: https://doi.org/10.26701/ems.869585
Received: January 28, 2021
Accepted: June 21, 2021

machine manufactured within the framework of the determined designs was examined.

2. MODELLING AND DESIGN

2.1. Compression spring design for fatigue tests

Before designing the compression spring fatigue machine, spring dimensions and working ranges to be used for the experiment should be specified. In Figure 1, the dimensions of a compression spring that can be used in the fatigue machine are determined. L_0 represents uncompressed spring length, L_1 represents first compression length, and L_2 represents second compression length.

After the compression springs are produced in length L_0, it is expected to generate force between working intervals of L_1 and L_2 through its minimum the working life. At the end of fatigue life, the main goal is to have no or very low loss of compression force. Therefore, a device must be arranged to compress the springs between L_1 and L_2 lengths.

In addition, by increasing the number of samples, the most statistically accurate fatigue life can be determined. Therefore, the most accurate design can be made by compressing many springs between two plates at the same intervals.

Force plates should be designed according to the size and capacity of the springs to be used in the spring fatigue machine. For this reason, it is necessary to standardize the dimensions of the springs that will be subjected to spring compression. The other purpose of this standardization is that the movements of the springs must be restricted by design in order to simulate them with a healthy way. Our spring samples must be in certain size intervals in order to be limited in terms of design. For this reason, the most used spring for experiments in Figure 1 has been chosen as the dimensional reference. Also, the compression lengths L_1 and L_2 are the same as the real-life compression spacing at the workplace.

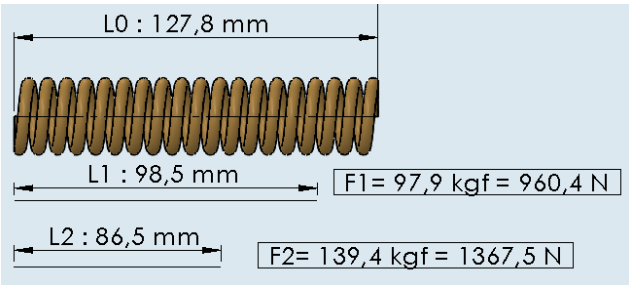

Figure 1. Compression spring sample design that to be tested.

In order to measure the forces between the lengths of L_0 - L_1 and L_0- L_2, the spring coefficient must be calculated. The spring coefficient can be determined by the force under two arbitrary shortening. Accordingly, a force of 139.4 kgf was obtained from the compression of the spring used as test reference to 98.5 mm, 97.4 kgf and 86.5 mm compression. If we convert the spring coefficient (1) into formula (2) according to the standard size and material;

$$F = k.x \tag{1}$$

$$k = \frac{F2 - F1}{L2 - L1} \tag{2}$$

$$k = \frac{139.4 - 97.9}{98.5 - 86.5}$$

$$k = 3.4 \text{ Kgf / mm}$$

According to the spring coefficient obtained, the forces obtained in L0 and L1 and L2 compression lengths are specified in (5) and (6).

$$F_1 = (L0 - L1) \cdot k = (127.8 - 98.5) \times 3.4 = 99.9 \text{ kgf} \tag{5}$$

$$F_2 = (L0 - L2) \cdot k = (127.8 - 86.5) \times 3.4 = 140.8 \text{ kgf} \tag{6}$$

Figure 2 shows the fastening mechanism that ensures the fatigue of 12 springs at the same time. Care should be taken to ensure that the diameter of the springs is larger than the maximum compressed diameter. Otherwise, the same working condition cannot be achieved. A pin passing through the center was also added to the design to prevent the springs from dislodging and deflection.

The spring fatigue machine design is shown in Figures 3 and 4. The springs placed between the upper and lower compression plates with number of 4 and 8 respectively are provided

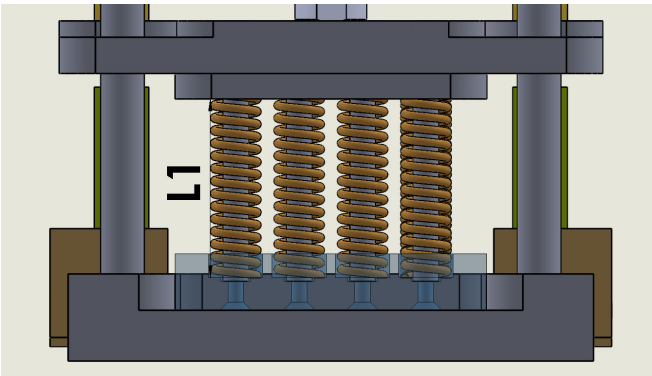

Figure 2. Positioning, design and the layout of the compression spring assembly.

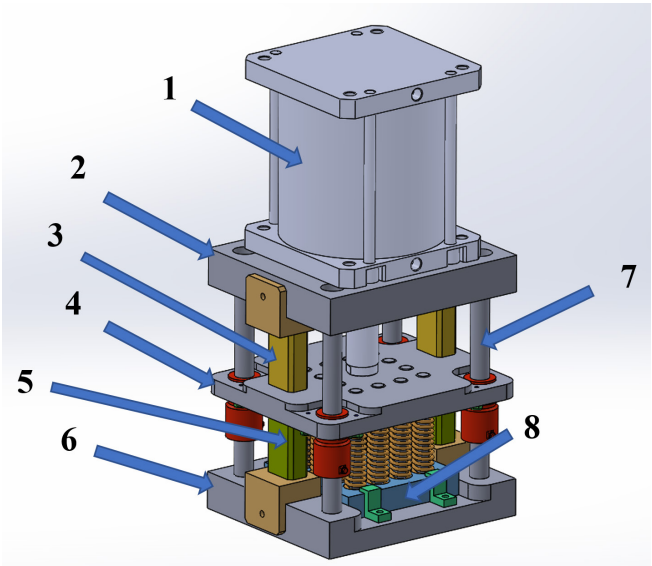

Figure 3. Compression spring fatigue machine design from isometric view.

with axial bearing with 4 column-bushing pairs number of 7. This bearing system is designed as dry bearing. Spring compression action is provided by a pneumatic cylinder. Stop block with number of 3 and 5 are used to restrict pneumatic cylinder movement. It is possible to test different lengths by changing the length of the stop blocks according to different compression conditions.

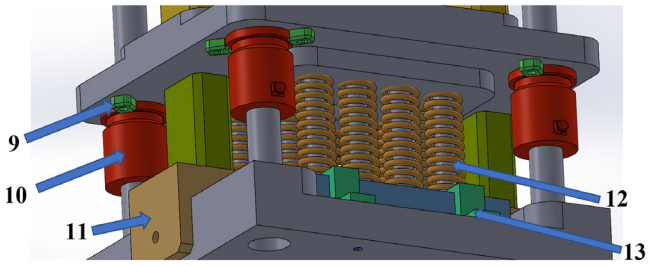

Figure 4. Compression spring fatigue machine design from detail view.

Table 1. The assembly list for the compression spring fatigue machine.

No	Part name	Piece
1	Pneumatic cylinder	1
2	Upper plate	1
3	Upper stop block	2
4	Support plate	1
5	Lower stop block	2
6	Lower plate	1
7	Column	4
8	Spring seat plate	1
9	Bush holder	8
10	Bronze guide bush	4
11	Stop block holders	4
12	Spring guide shaft	12
13	Spring holder	2

2.2. Sizing of pneumatic drive piston

In the design, the drive force to be applied to the compression springs is designed to be carried out from a pneumatic cylinder with the appropriate force. The force applied by the pneumatic cylinder is directly proportional to the cylinder surface area and the applied air pressure. The standard air pressure used in factory systems is used as 6 ± 0.5 bar (600.000 Pa). To ensure the compression of the spring, a force greater than the compression force of the springs must be obtained. The cylinder diameter to be driven is selected as 200 mm. In addition, the double-acting cylinder was selected to return again by air power. The control of whether the selected diameter is greater than the applied force is made in (6).

$A = \prod x\ r^2 = \prod x\ 0{,}1^2 = 0.0314\ m^2$

$F = P\ .\ A;\ \ F = 600.000\ x\ 0.0314$

$F_{Cylinder} = 18840\ N = 1920.489\ kgf$

$F_{total\ comp} = n\ .\ F_{comp\ single};\ F_{total\ comp} = 12\ .\ 140.8 = 1689.6\ kgf$

$F_{Cylnder} > F_{toatal\ comp}$

1920.489 kgf >1689.6 kgf with this result, It is concluded that the pneumatic cylinder is suitable.

2.3. Electrical equipment design

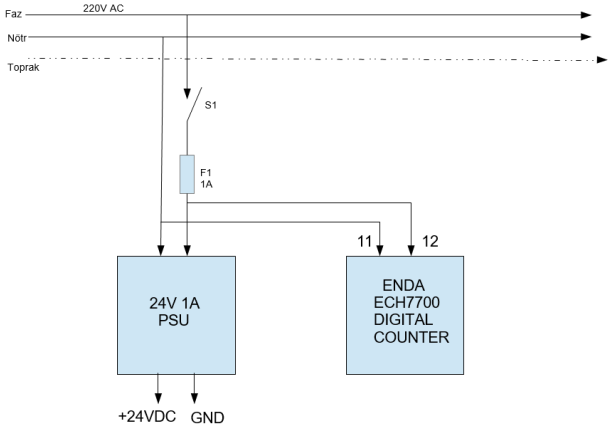

Figure 5. Scheme received from the 220V electric source.

The electrical equipment of the spring fatigue device is shown in Figures 5 and 6. Figure 5 shows that the power taken from the 220 V mains supply feeds the 24 V power supply and the ENDA 7700 digital counter. In addition, a 2 A fuse has been installed in order to protect the device in case the power drawn from the network is overloaded.

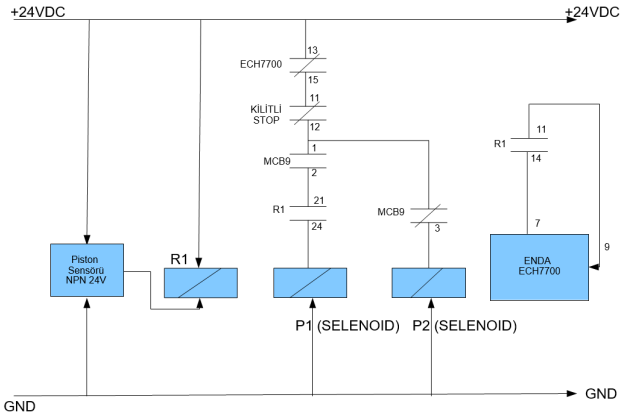

Figure 6. The main electrical scheme of compression spring fatigue machine.

Figure 6 shows the electrical diagram of compression spring fatigue machine fed by 24 V supply. Accordingly, the RZT1 position sensor mounted on the pneumatic piston was positioned at the off position. When the sensor generate signals, it indicates that the piston springs are in the maximum compression position and the cylinder is completely down. The resulting signal controls the R1 switch. R1 switch is also connected to P1 solenoid. The MCB9 timer relay is set to 0.5 seconds. The MCB9 timer relay is connected to both solenoids. The MCB9 timer relay activates solenoid P1 if it is on and solenoid P2 is off. However, the completion of the circuit depends on the allowance of the emergency stop and the counter. Since the counter is activated with the R1 switch, it will operate under normal conditions. However, the counter will not work when R1 is not turned on. Thus, possible unforeseen errors are prevented. Emergency stop is normally off and connected to the main solenoid control line. It operates normally open like a counter, it cuts the circuit communication when the emergency stop button is pressed, and ensures the test is stopped. The electrical equipment used in

the device is shown in Table 2.

Table 2. Electrical equipment used in the compression spring fatigue machine.

No	Electrical equipment	Piece
1	5/2 24V double coil pneumatic valve	1
2	MCB-9 multifunction time relay	1
3	24V relay	1
4	24V power supply	1
5	2 A fuse	1
6	Emergency stop button	1
7	Ech7700 counter	1
8	RZT1 sensor	1

2.4. Machine design and manufacturing

The assembled version of the designed compression spring fatigue machine is as in Figure 7. All plates are made of Ck45 steel. Care has been taken to keep the parallelism tolerance below 0.01 mm in order to prevent deflection during the operation. For this reason, the bottom and surfaces of the plates were grinded in Ra 0.8 quality. Punch with countersunk head made of 1.2210 material, which is a ready-to-assemble mold element, is used for the pins that ensure that the springs are centered and not removed during operation. It was assembled with the manufactured plates and other ready-to-assemble equipment, then, it was assembled into a base designed with aluminum profiles. The machine control unit and pneumatic valve are installed in an enclosure box. Emergency stop button and counter are mounted on the enclosure box with an easily accessible manner.

Figure 7. Compression spring fatigue machine.

The highest speed is 60 compression cycles per minute, as the maximum operating speed is controlled by the multi-function time relay. This speed must run for 27.7 hours to complete 100 000 fatigue cycles. The most important reason for the low working speed is also related to the closing time of the pneumatic cylinder and limit of air pressure line.

3. CONCLUSION

In this study, a fatigue device is designed to simulate fatigue behavior of compression springs. In the design, it has been designed in a way to make the fatigue of 12 springs together in order to be statistically correct. The working system has been designed successfully and it has been observed that there is no problem in its operation. Since it imitates the same life values encountered in real life, it is assumed to draw the closest possible result. It is practical and convenient to use. However, further development of the system in terms of speed and instantaneous force measurement, inability to monitor S-N and strength values of the springs simultaneously constitute its main deficiencies.

REFERENCES

[1] Kong, Y.S., Abdullah, S., Schramm, D., Omar, M.Z., Haris, S.M., Bruckmann, T. (2017). Mission profiling of road data measurement for coil spring fatigue life. Measurement: Journal of the International Measurement Confederation. 107: 99–110. doi: 10.1016/j.measurement.2017.05.011.

[2] Zhang, P., Wang, D., Guo, Y., Cheng, P., Shao, C., Lang, N., et al., (2020). Fatigue failure analysis and finite element assessment of the twins torsion spring. Engineering Failure Analysis. 122(July 2020): 105187. doi: 10.1016/j.engfailanal.2020.105187.

[3] Mohammad Hashemi, Y., Kadkhodaei, M., Mohammadzadeh, M.R., (2019). Fatigue analysis of shape memory alloy helical springs. International Journal of Mechanical Sciences. 161–162(July). doi: 10.1016/j.ijmecsci.2019.105059.

[4] Drummen, I., Storhaug, G., Moan, T. (2008). Experimental and numerical investigation of fatigue damage due to wave-induced vibrations in a containership in head seas. Journal of Marine Science and Technology. 13(4): 428–45. doi: 10.1007/s00773-008-0006-5.

[5] Pyttel, B., Brunner, I., Kaiser, B., Berger, C., Mahendran, M. (2014). Fatigue behaviour of helical compression springs at a very high number of cycles - Investigation of various influences. International Journal of Fatigue. 60: 101–9. doi: 10.1016/j.ijfatigue.2013.01.003.

[6] Močilnik, V., Gubeljak, N., Predan, J., Flašker, J. (2010). The influence of constant axial compression pre-stress on the fatigue failure of torsion loaded tube springs. Engineering Fracture Mechanics. 77(16): 3132–42. doi: 10.1016/j.engfracmech.2010.07.014.

[7] Li, W., Sakai, T., Wakita, M., Mimura, S., (2014). Influence of microstructure and surface defect on very high cycle fatigue properties of clean spring steel. International Journal of Fatigue. 60: 48–56. doi: 10.1016/j.ijfatigue.2013.06.017.

[8] Bi, S., Li, Y., Zhao, H., (2019). Fatigue analysis and experiment of leaf-spring pivots for high precision flexural static balancing instruments. Precision Engineering. 55(October 2018): 408–16. doi:

10.1016/j.precisioneng.2018.10.009.

[9] Berger, C., Kaiser, B., (2006). Results of very high cycle fatigue tests on helical compression springs. International Journal of Fatigue. 28(11): 1658–63. doi: 10.1016/j.ijfatigue.2006.02.046.

[10] Akiniwa, Y., Stanzl-Tschegg, S., Mayer, H., Wakita, M., Tanaka, K., (2008). Fatigue strength of spring steel under axial and torsional loading in the very high cycle regime. International Journal of Fatigue. 30(12): 2057–63. doi: 10.1016/j.ijfatigue.2008.07.004.

EUROPEAN MECHANICAL SCIENCE
e-ISSN: 2587-1110

Research Paper

Efficiency of the Gaver-Stehfest Method Transient Response of a Spiral Fin

Bilal Sungur[1*], Ibrahim Keles[2]

[1,2]Department of Mechanical Engineering, Samsun University, 55420, Samsun, Turkey

Abstract

In this study, a practical combined approach was applied by the Gaver-Stehfest method to examine the impermanent reaction of a spiral fin whose tip is isolated with the base tip exposed to changes in fluid temperature. The heat transmission of the fin under the stable temperature effect of the base is examined. The environment temperature is saved stationary, and no heat source or sink is available. Results are improved for minor- and major -time worth when the base is exposed to the unit step variation form in temperature. The changes in heat flux and temperature at the base formed depending on the parameters that make up the spiral fin are graphically shown. The available numerical results show that it is fully consistent when compared with the literature.

Keywords: Laplace transform, Transient response, Spiral fin, Heat transfer, Gaver-Stehfest method

1. INTRODUCTION

Many engineers and researchers have done a lot of work to increase the response problem in the fins and heat dissipation from a hot surface using fins in industrial applications. One of the methods used to raise the amount of heat transfer with the developing technology is the fins used to expand the heat transfer surfaces. Spiral fins are widely used in industrial applications and are used to ensure optimum temperature distribution in turbines, generators, power plants, and electronic devices [1].

Chu et al. [1–3] analyzed the impermanent responses of both external flat and annular fins as well as unidimensional circular fin and compound flat fins using the Fourier sequences and overturn method. Using the natural convection correlations available for plates, the efficiency of circular fins of distinct profiles exposed to local heat transmission constant as a function of local temperature was investigated by Mokheimer et al. [4]. The impact of conduction heat transmission in different shapes of annular fins [5], current conduction effect in multidimensional sizes [6], fins exposed to temperature-addicted heat flux [7], and dispersed transportation effect along the curly plaque consisting of circular slices [8] have been studied by the researchers. Also, problems related to the optimization of fins and spines have been investigated [9,10]. Yu and Chen [11] recommended the Taylor transform and limited difference approach to examine the non-linear temporary heat transmission problematic of the rectangular profile circular fin, taking into account the step temperature change occurring in the radiation wing tip and infinite base by convection. By choosing the heat transmission constant temperature as the power function type and using the power values representing changed heat transmission machines for example independent convection, completely industrialized boiling and radiation, the longitudinal and annular fins and spines have been presented by Laor and Kalman [12]. Zubair et al. [13] analyzed a one-dimensional fin with a variant shape that can be abridged to a rectangular shape. Bouaziz et al. [14] examined the temperature-dependent efficacy of longitudinal fins by thermo-physical features. The symbolic mathematical equation for the tip temperature and fin efficacy of circular blades, depending on the thermo-geometric blade parameters and radius ratio, was obtained by Campo and Stuffle [15]. Wang et al. [16] analytically presented the temporary reply of a spiral fin whose bottom was subjected to variant heat flow.

Suppose the solution of mathematical, physics, chemistry and engineering problems defined by differential equations is resolved in the Laplace space. In that case, it may be hard or even unbearable to gain an analytical translation into the time domain. Numerical methods for numerical overturn of the inverse Laplace transform to generate resolutions in the time area have been used in science and engineering since the 1930s. The Gaver-Stehfest method is one of these

* Corresponding author
Email: bilal.sungur@samsun.edu.tr

European Mechanical Science (2021), 5(4): 194-200
doi: https://doi.org/10.26701/ems.899389
Received: July 3, 2020
Accepted: September 8, 2020

numerical methods that is used efficiently and successfully. Since the introduction of the method, the Gaver-Stehfest procedure has been successfully implemented in many fields such as geophysics [17], probability [18,19], actuarial mathematics [20], and scientific finance [21], chemical [22], and economy [23].

In this study, the solutions of the temporary reply of the end insulated spiral fin are analyzed for unit step temperature change subject to change by the base in fluid temperature with easy-to-calculate Laplace transformations for short time intervals. After the general equations that make up the problem are obtained in the Laplace space, the results of the temperature change obtained by transporting them to the time space by the Gaver-Stehfest method are presented in graphs. It can be said that the results given in Ref.[16] and the results obtained here match exactly.

2. TRANSIENT RESPONSE MATHEMATICAL MODEL OF A SPIRAL FIN

Fig. 1 demonstrated a spiral fin's schematic diagram with livery thickness z=2δ, internal radius ri, outside radius ro, field P, and thermal conductivity *k*. The end of the fin, $r= r_o$ is supposed well isolated. Besides, a one-dimensional analysis assumption is made. At first, the fin and the surrounding fluid temperature (T_∞) are in thermal equilibrium. The bottom temperature is instantly increased to T_f and related to heat flux q_0^*, since then, the spiral fin dissolute heat to the perimeter via convection mechanism. The properties *h*, h_f, and *c*, *ρ*, *k* of the fin materials are all accepted as constant. In additional boundary condition, $r=r_i$, by ignoring the thermal resistor and capacity of the physical in internal wall pipe, the convective boundary condition is assumed.

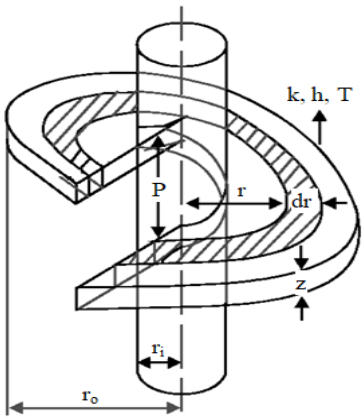

Figure 1. Schematic view of the spiral fin [16]

Using the conservation of energy equation, the differential equation of the spiral fin temperature can be written as[16]:

$$\frac{\partial}{\partial r}\left\{\sqrt{\left(\frac{P}{2\pi}\right)^2+r^2}\,\frac{\partial T}{\partial r}\right\}-\frac{h}{k\delta}\sqrt{\left(\frac{P}{2\pi}\right)^2+r^2}\,[T-T_\infty]=\frac{1}{\alpha}\sqrt{\left(\frac{P}{2\pi}\right)^2+r^2}\,\frac{\partial T}{\partial r},\quad t>0,\ r_i<0<r_o \tag{1}$$

where, $\alpha = k/\rho c$ is the thermal diffusivity and $B_i = h_f r_i / k_f$ is the Biot number.

After the explanation of non-dimensional parameters,

$$\xi=\frac{r}{r_i},\phi=\frac{T-T_\infty}{T_f-T_\infty},\alpha=\frac{\alpha t}{r_i^2},P_i=\frac{P}{2\pi r_i},R=\frac{r_o}{r_i},N^2=\frac{hr_i^2}{k\delta}$$

The non-dimensional governing equation becomes as follows:

$$\frac{\partial}{\partial\xi}\left\{\sqrt{P_i^2+\xi^2}\,\frac{\partial\phi}{\partial\xi}\right\}-N^2\sqrt{P_i^2+\xi^2}\,\phi=\sqrt{P_i^2+\xi^2}\,\frac{\partial\phi}{\partial\tau},\ \tau>0,\quad 1<\xi<R \tag{2}$$

The environmental temperature is assumed that at a fixed temperature, and it was also assumed that there was no heat source or heat sinks. The non-dimensional initial and boundaries can be explained as follows:

$$\phi(\xi,0)=0,\ 1<\xi<R \tag{3}$$

$$-\frac{\partial\phi}{\partial\xi}+B_i\phi=B_i,\quad \xi=1,\quad \tau>0 \tag{4}$$

$$-\frac{\partial\phi}{\partial\xi}(R,t)=0,\quad \tau>0 \tag{5}$$

Eq.2 is subjected to Laplace transform, and by applying the initial condition given in Eq.3, the final state of the equation is as follows:

$$-\frac{\partial\phi}{\partial\xi}\left\{\sqrt{P_i^2+\xi^2}\,\frac{\partial\bar{\phi}}{\partial\xi}\right\}-\left\{\sqrt{P_i^2+\xi^2}\left[N^2+s\right]\right\}\ \bar{\phi}=0 \tag{6}$$

In this equation, s symbolized the transformed variant. Integrals in the exponential constant can be neglected, and then the Keller and Keller's solution of Eq.6 becomes as follows:

$$\bar{\phi}(\xi,s)=D_2\left\{-\left[N^2+s\right]\left[P_i^2+\xi^2\right]\right\}^{-1/4}\cdot\cosh\left[\sqrt{N^2+s}\,(R-\xi)\right] \tag{7}$$

In this equation, D_2 is a fixed to be identified by the boundary condition (4). The boundary condition (4) can be expressed as follows by using Laplace transformation:

$$-\frac{\partial\bar{\phi}}{\partial\xi}+B_i\bar{\phi}=\frac{B_i}{s},\quad \xi=1 \tag{8}$$

The constant D_2 can be expressed as follows by substituting Eq.7 into Eq.8,:

$$D_2=\frac{2B_i\left[-\left(N^2+s\right)\right]^{1/4}\left[P_i^2+1\right]^{3/2}}{\left\{2\left[P_i^2+1\right]^{5/4}\cdot\sqrt{N^2+s}\cdot s\cdot\sinh\left[\sqrt{N^2+s}\,(R-1)\right]+s\left[P_i^2+1\right]^{1/4}\cdot\cosh\left[\sqrt{N^2+s}\,(R-1)\right]\left[2B_i\left(P_i^2+1\right)+1\right]\right\}} \tag{9}$$

Thus, Eq.7 becomes

$$\bar{\phi}(\xi,s)=\frac{2\left[P_i^2+1\right]^{5/4}}{s\left[P_i^2+\xi^2\right]^{1/4}}\cdot\frac{\cosh\left[\sqrt{N^2+s}\,(R-\xi)\right]}{\left\{2\left[P_i^2+1\right]\cdot\sqrt{N^2+s}\cdot s\cdot\sinh\left[\sqrt{N^2+s}\,(R-1)\right]+\left[2B_i\left(P_i^2+1\right)+1\right]\cdot\cosh\left[\sqrt{N^2+s}\,(R-1)\right]\right\}} \tag{10}$$

Defining the dimensionless heat flux at the fin base as:

$$q_0^*=q_b r_i/4k\left[\delta\pi r_1\right]T_f-T_\infty \tag{11}$$

After using the dimensionless constraints, the heat flux can be written as:

$$q_0^*=-\sqrt{P_i^2+1}\,\frac{\partial\phi}{\partial\xi}(1,\tau),\quad \tau>0 \tag{12}$$

3. THE GAVER-STEHFEST INVERSE LAPLACE METHOD

Researchers have successfully applied the Gaver-Stehfest method(GSM) to many different fields and different prob-

lems and based on a simple algorism for numerical overturn of the Laplace transform [24–26].

With this method, the Laplace space is transformed into the time domain as follows [27];

$$f(t)=\frac{\ln 2}{t}\sum_{k=1}^{M}V_k F\left(k\frac{\ln 2}{t}\right) \tag{13}$$

where V_k is expressed as follows;

$$V_k=(-1)^{k+\frac{M}{2}}\sum_{j=\left(\frac{k+1}{2}\right)}^{\min\left(k,\frac{M}{2}\right)}\frac{j^{\frac{M}{2}}(2j)!}{\left(\frac{M}{2}-j\right)!j!(j-1)!(k-j)!(2j-k)!} \tag{14}$$

Here the parameter M is expressed as the number of Stehfest. The precision of the calculation depends on the M value, so this value must be an even integer because the inversion is based upon the sum of M weighted values. In theory, choosing a large value for M would suggest a more correct resolution, but if M is too big, results may deteriorate because of rounding mistakes. Therefore, it is important to choose an appropriate M value to reach the best solution [28]. Most researchers suggest a changed worth of the M constraint to get the best solution. Cheng and Sidauruk [29] suggested that the M value should be between 6 and 20. In this study, the M value was chosen as 16.

4. RESULTS

Dimensionless distribution of temperature of the spiral fin found from Eq. 7 is given in Fig. 2-5 for distinct worthies of B_i, τ, R and P_i. It can be seen from these figures, in all cases, the temperature distribution, ϕ, rises with the increasing time. Additionally, while the effect of the increase in time is more effective at the beginning, it gradually decreases afterward. This means the throughput heat flux in base of spiral fin will be reduced and the internal temperature of spiral fin will be increased with the time elapsed. Also, the increase in pitch values P_i increased the temperature distribution at the similar values of τ, R, B_i, and N excepting for the high values of N and low values of τ.

When we examine the Fig. 2 and Fig. 3, at the larger value of B_i, the maximum temperature distribution obtained at the similar values of N, P_i, τ and R. Increasing the B_i number means that the heat transmission from the fin base will increase, and in this case, it is one of the important parameters affecting the temperature distribution. In order to compare the effect of the N value, it will be useful to analyze Fig. 3 and Fig. 4. These figures demonstrated that the higher values of N, means the lesser temperature distribution at the similar values of τ, P_i, R and B_i. The effect of the R values is shown from Fig. 3 and Fig. 5. It can be said that similar trends were obtained as N value, while the R rises, the temperature distribution declines at the similar value of τ, B_i, P_i and N.

As shown in Fig. 2-5, in all cases, it has been determined that the numerical calculation results were in well arrangement with the analytical consequences obtained from the literature [16].

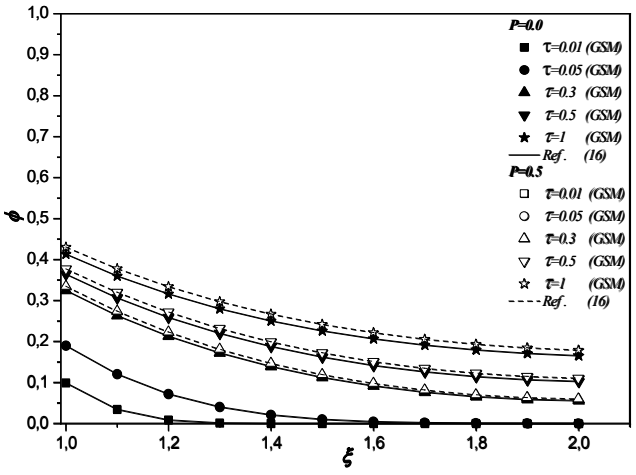

Figure 2. Distributions of temperature for varying τ with $R=2$, $N=1$ and $B_i=1$

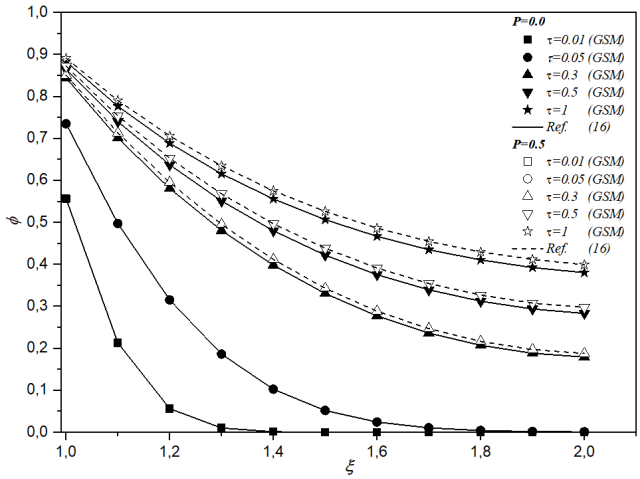

Figure 3. Distributions of temperature for varying τ with $R=2$, $N=1$ and $B_i=10$

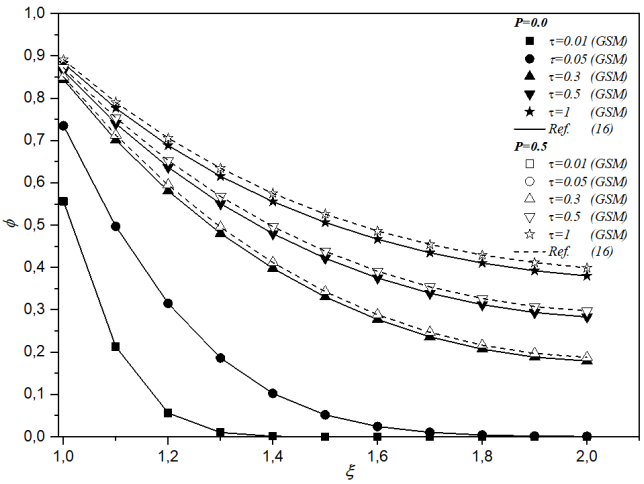

Figure 4. Distributions of temperature for varying τ with $R=2$, $N=5$ and $B_i=10$

The heat flux at the fin base, q_0^*, with distinct constraints of τ, B_i, P_i and N are given in Fig. 6 and Fig.7. As shown from these figures, increasing the N number increased the heat flux values in all cases. Also, increasing the B_i number increased the heat flux values in all cases. After a certain time

(τ≈1), the effect of time becomes almost negligible. Additionally, increasing the P_i, increased the heat flux values for all Bi and N numbers.

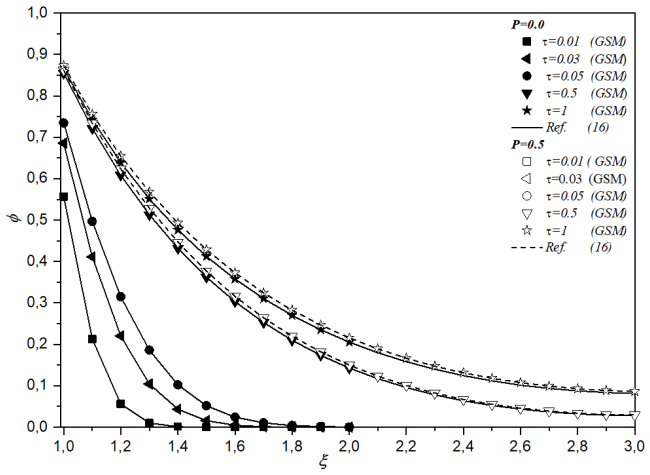

Figure 5. Distributions of temperature for varying τ with *R=3, N=1* and B_i*=10*

The variation of temperature distribution with time is given in Fig. 8 and Fig. 9 for different B_i, and N numbers. As can be seen, there are very similar trends in both graphs and the effect of P_i to the temperature distribution is very small in these conditions. Increasing the B_i number increased the heat transfer and for this reason, it is seen that the temperature progresses faster with at higher B_i numbers. Also, the higher N number means the higher heat transfer rate and temperature distribution. However, with the increase in the number of Bi, the effect of the N number gradually decreased, and the curves got closer to each other.

5. CONCLUSIONS

Numerical model of the transient response of the end insulated spiral fin for temperature and heat flux distributions are obtained and solved by GSM. When the efficiency and adequacy of the current method are compared with the analytical results, it is seen that they overlap [16] one to one. The solution technique and procedure are simple, efficient, and well structured and provide low-cost accuracy. When the numerical results in this study are evaluated, the results are briefly summarized below:

- The technique applied is more effective than the conservative techniques.
- The results show that the temperature change is affected depending on the *N*, P_i, *R* variables.
- The larger the *N* value, the greater the heat conversion creates the spiral blade and the greater the tem-

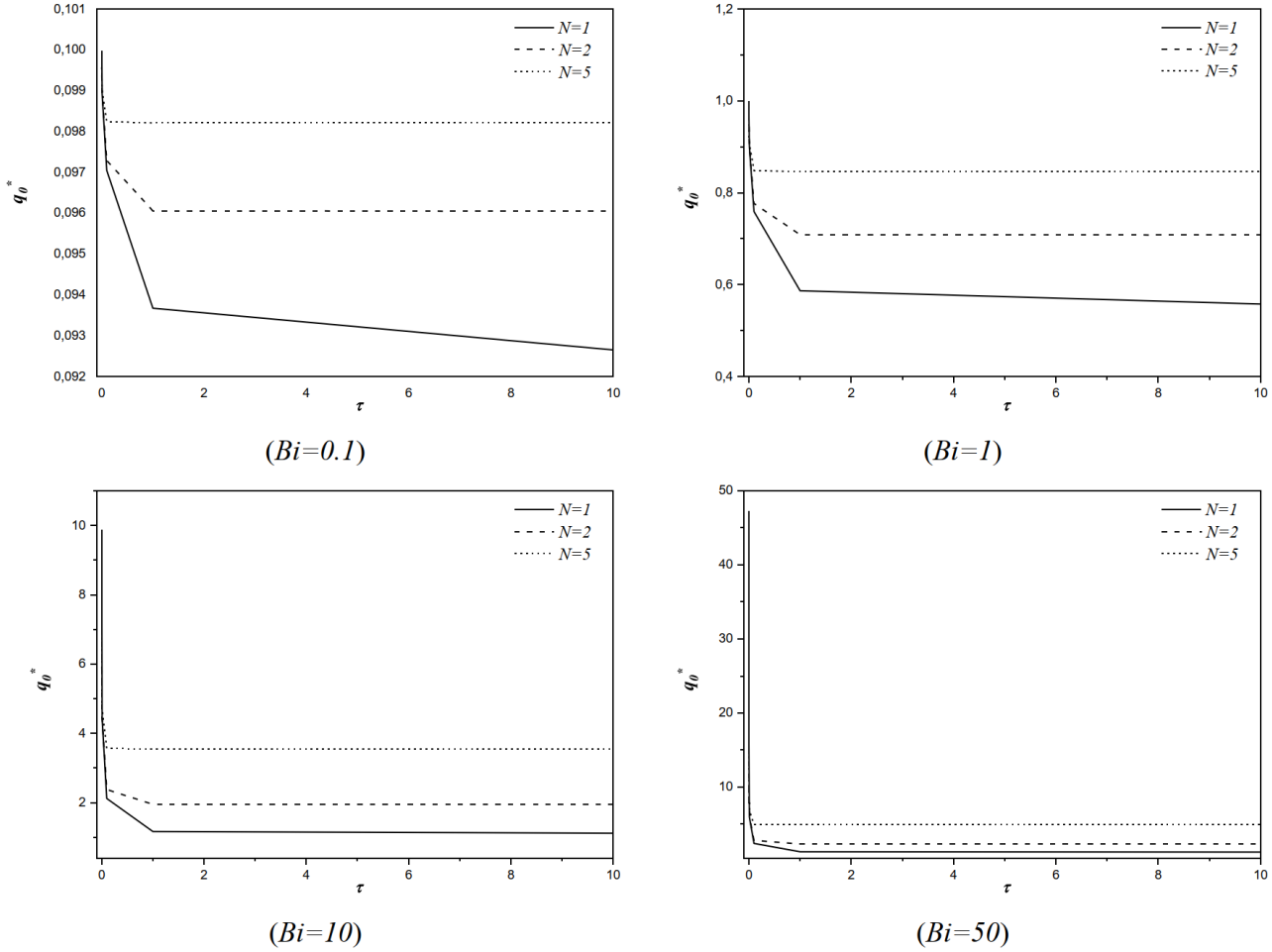

Figure 6. Distributions of heat flux for varying *N* with *R=2*, and P_i*=0*

doi: https://doi.org/10.26701/ems.899389

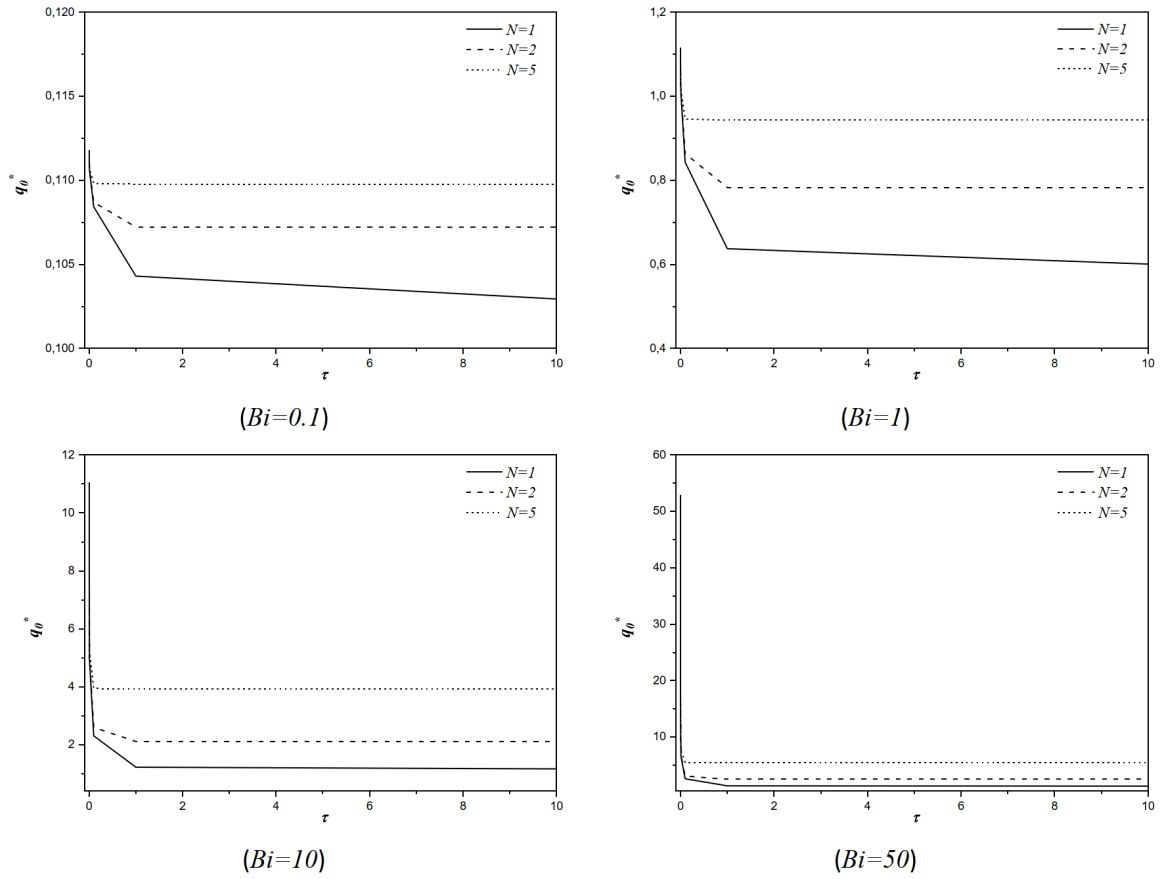

Figure 7. Distributions of heat flux for varying *N* with *R=2*, and P_i *=0.5*

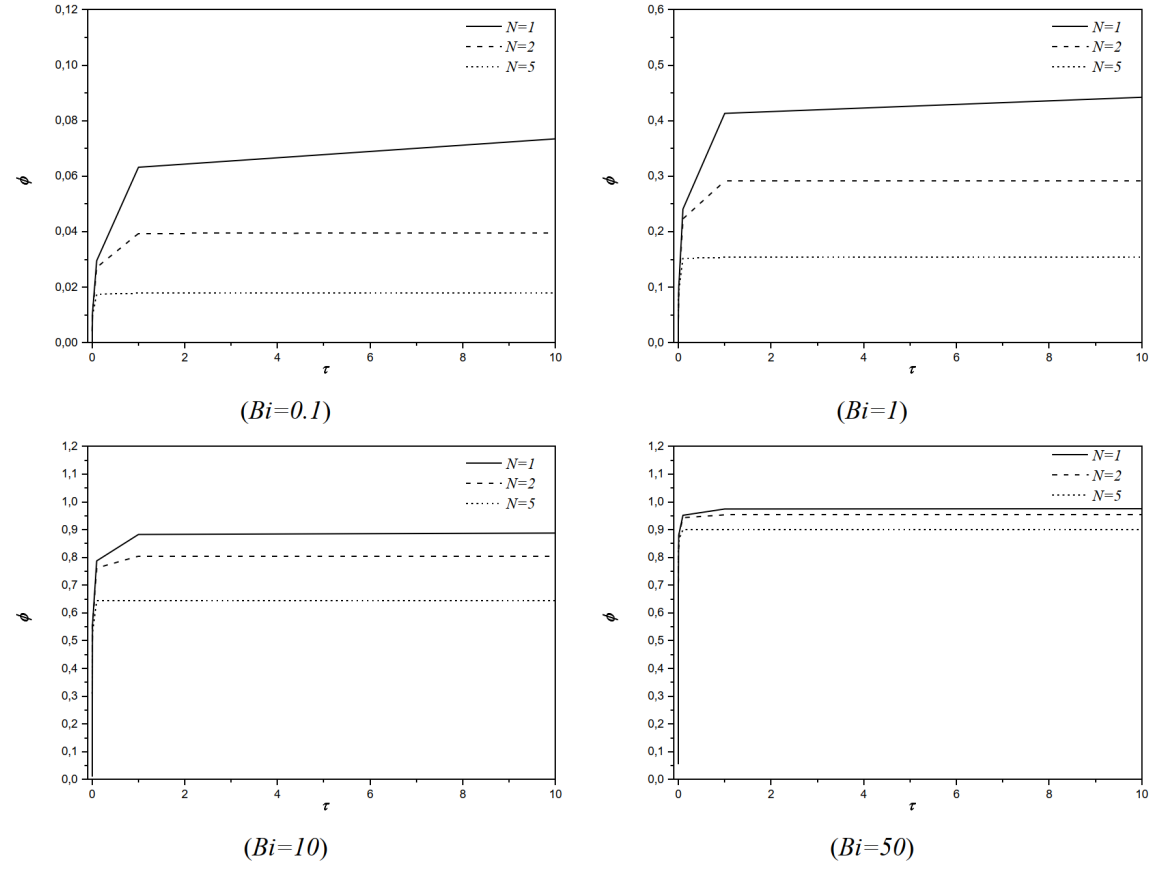

Figure 8. Distributions of temperature for varying *N* with *R=2*, and P_i =0

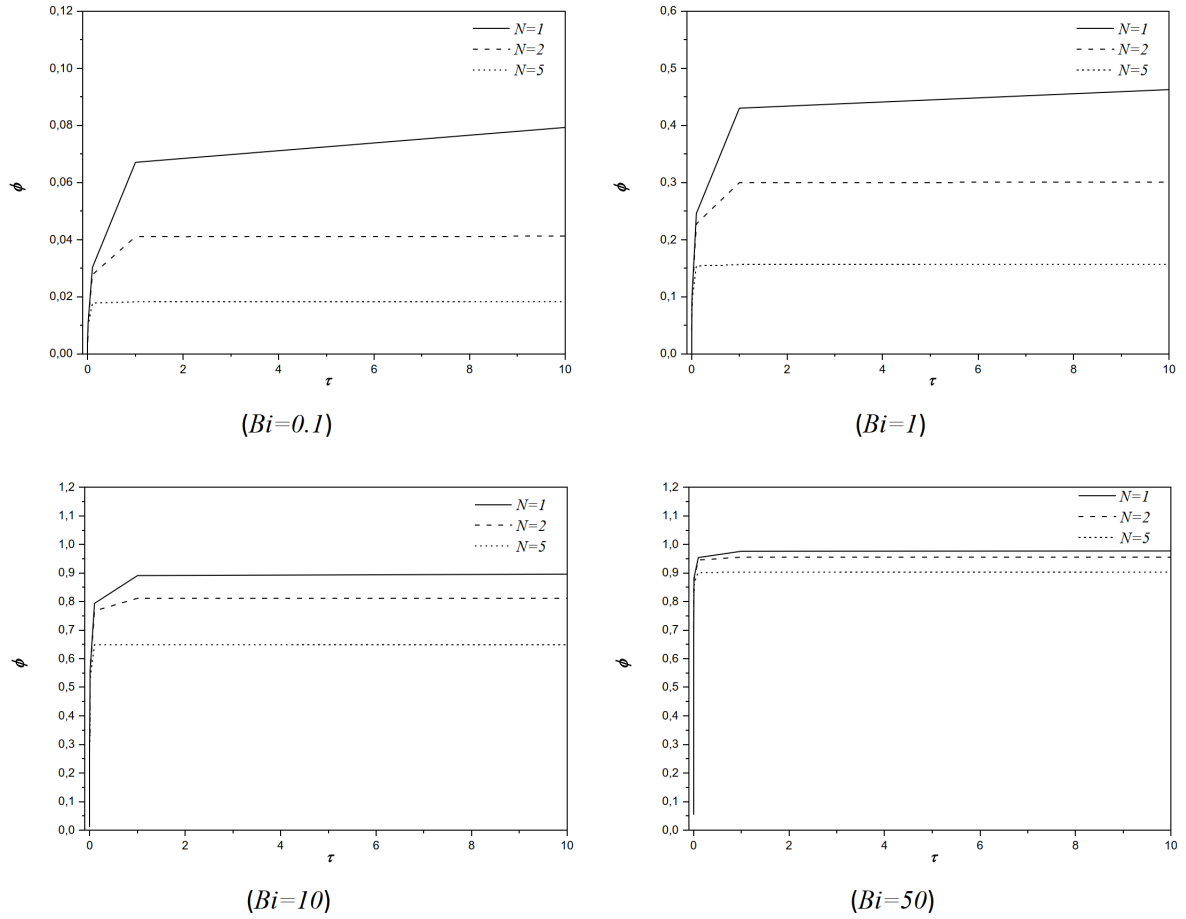

Figure 9. Distributions of temperature for varying N with R=2, and P_i =0.5

perature distribution.

- For the heat flux distribution q_0^* in the spiral fin base, the variable N and P_i are the important variables, and the variable P_i affects q_0^* much more as the N variable increases.
- The results obtained in this study can be used as a basis in the application of spiral fins to the industry.

REFERENCES

[1] Chu, H.-S., Chen, C.-K., Weng, C.-I., (1982). Applications of Fourier series technique to transient heat transfer problem. Chemical Engineering Communications. 16(1–6): 215–25. https://doi.org/10.1080/00986448208911098

[2] Chu, H.S., Chen, C.K., Weng, C.I., (1983). Transient response of circular pins. Journal of Heat Transfer. 105(1): 205–8. doi: 10.1115/1.3245547.

[3] Chu, H. Sen., Weng, C.I., Chen, C.K., (1983). Transient Response of Composite Straight Fin. Advances in the Astronautical Sciences. 50(pt 1): 539–49. https://doi.org/10.1115/1.3245579

[4] Mokheimer, E.M.A., (2002). Performance of annular fins with different profiles subject to variable heat transfer coefficient. International Journal of Heat and Mass Transfer. 45(17): 3631–42. https://doi.org/10.1016/S0017-9310(02)00078-9

[5] Cheng, C.-Y., (1994). Transient response of annular fins of various shapes subjected to constant base heat fluxes. Journal of Physics D: Applied Physics. 27(11): 2302. https://doi.org/10.1088/0022-3727/27/11/009

[6] Lee, Y.-M., Haji-Sheikh, A., Fletcher, L.S., Peterson, G.P., (1994). Effective thermal conductivity in multidimensional bodies. Journal of Heat Transfer. 116(1):17-27. https://doi.org/10.1115/1.2910853

[7] Liaw, S.P., Yeh, R.H., (1994). Fins with temperature dependent surface heat flux—I. Single heat transfer mode. International Journal of Heat and Mass Transfer. 37(10): 1509–15. https://doi.org/10.1016/0017-9310(94)90152-X

[8] Wang, C.Y., (1994). Diffusive transport across a wavy plate composed of annular sectors.

[9] Yeh, R.-H., (1994). Optimum spines with temperature dependent thermal parameters. International Journal of Heat and Mass Transfer. 37(13): 1877–84. https://doi.org/10.1016/0017-9310(94)90328-X

[10] Yeh, R.-H., (1994). Optimization of longitudinal fins with temperature-dependent thermal parameters. Heat Transfer Engineering. 15(3): 25–34. https://doi.org/10.1080/01457639408939828

[11] Chen Cha'O-Kuang, L.-T.Y., (1999). Application of the Taylor transformation to the transient temperature response of an annular fin. Heat Transfer Engineering. 20(1): 78–87. https://doi.org/10.1080/014576399271736

[12] Laor, K., Kalman, H., (1996). Performance and optimum dimensions of different cooling fins with a temperature-dependent heat transfer coefficient. International Journal of Heat and Mass Transfer. 39(9): 1993–2003. https://doi.org/10.1016/0017-9310(95)00296-0

[13] Zubair, S.M., Al-Garni, A.Z., Nizami, J.S., (1996). The optimal dimensions of circular fins with variable profile and temperature-dependent thermal conductivity. International Journal of Heat and Mass Transfer. 39(16): 3431–9. https://doi.org/10.1016/0017-9310(96)00011-7

[14] Bouaziz, M.N., Rechak, S., Hanini, S., Bal, Y., Bal, K., (2001). Étude des transferts de chaleur non linéaires dans les ailettes longitudinales. International Journal of Thermal Sciences. 40(9): 843–57. https://

doi.org/10.1016/S1290-0729(01)01271-6

[15] Campo, A., Stuffle, R.E., (1997). Symbolic mathematics for the calculation of thermal efficiencies and tip temperatures in annular fins of uniform thickness. International Journal of Heat and Mass Transfer. 40(2): 490–2. https://doi.org/10.1016/0017-9310(96)00093-2

[16] Wang, J.S., Luo, W.J., Hsu, S.P., (2008). Transient Response of a Spiral Fin with its Base Subjected to the Variation of Heat Flux. Journal of Applied Sciences. 8(10): 1798–811. https://doi.org/10.3923/jas.2008.1798.1811

[17] Knight, J.H., Raiche, A.P., (1982). Transient electromagnetic calculations using the Gaver-Stehfest inverse Laplace transform method. Geophysics. 47(1): 47–50. https://doi.org/10.1190/1.1441280

[18] Abate, J., Whitt, W., (1992). The Fourier-series method for inverting transforms of probability distributions. Queueing Systems. 10(1): 5–87. https://doi.org/10.1007/BF01158520

[19] Kou, S.G., Wang, H., (2003). First passage times of a jump diffusion process. Advances in Applied Probability.: 504–31. https://doi.org/10.1239/aap/1051201658

[20] Badescu, A., Breuer, L., Da Silva Soares, A., Latouche, G., Remiche, M.-A., Stanford*, D., (2005). Risk processes analyzed as fluid queues. Scandinavian Actuarial Journal. 2005(2): 127–41. https://doi.org/10.1080/03461230410000565

[21] Schoutens, W., Van Damme, G., (2011). The β-variance gamma model. Review of Derivatives Research. 14(3): 263–82. https://doi.org/10.1007/s11147-010-9057-y

[22] Montella, C., (2008). LSV modelling of electrochemical systems through numerical inversion of Laplace transforms. I–The GS–LSV algorithm. Journal of Electroanalytical Chemistry. 614(1–2): 121–30. https://doi.org/10.1016/j.jelechem.2007.11.010

[23] Kawakatsu, H., (2005). Numerical inversion methods for computing approximate p-values. Computational Economics. 26(3–4): 103–16. https://doi.org/10.1007/s10614-005-9011-5

[24] Egonmwan, A.O., (2012). The numerical inversion of the Laplace transform. LAP Lambert Academic Publishing

[25] Valkó, P.P., Vajda, S., (2002). Inversion of noise-free Laplace transforms: towards a standardized set of test problems. Inverse Problems in Engineering. 10(5): 467–83. https://doi.org/10.1080/10682760290004294

[26] Mashayekhizadeh, V., Dejam, M., Ghazanfari, M.H., (2011). The application of numerical Laplace inversion methods for type curve development in well testing: a comparative study. Petroleum Science and Technology. 29(7): 695–707. https://doi.org/10.1080/10916460903394060

[27] Zhang, J., (2007). Some innovative numerical approaches for pricing American options.

[28] Hassanzadeh, H., Pooladi-Darvish, M., (2007). Comparison of different numerical Laplace inversion methods for engineering applications. Applied Mathematics and Computation. 189(2): 1966–81. https://doi.org/10.1016/j.amc.2006.12.072

[29] Cheng, A.H.D., Sidauruk, P., Abousleiman, Y., (1994). Approximate inversion of the Laplace transform. Mathematica Journal. 4(2): 76–82.

EUROPEAN MECHANICAL SCIENCE
e-ISSN: 2587-1110

Research Paper

A Battery Powered on-Chip Peristaltic Pump for Lab-On-A-Chip Applications

Sinan Gucluer[1*]

[1]Department of Mechanical Engineering, Aydın Adnan Menderes University, Turkey

Abstract

In this work, a low-cost and practical peristaltic pump is demonstrated using 3D printing and an open-sourced microcontroller platform. The peristaltic pump is designed to be compatible with polydimethylsiloxane (PDMS) microfluidic chips which are also fabricated through replica molding method using 3D printed molds. A thin layer of PDMS which was bonded on top of the microfluidic chip is designed to have a circular-shaped channel to be aligned with the circular arrangement of steel ball bearings. The entire system is designed to be portable and capable of producing metered fluid flow in small-scale devices. The developed device is characterized to provide adjustable fluid flow control between 1.7 µL/s to 23 µL/s which is suitable for many on-chip applications. Overall, a low-cost, portable and simple-to-fabricate peristaltic pump is presented.

Keywords: microfluidics, peristaltic pump, fluid manipulation, 3D printing

1. INTRODUCTION

In the last two decades, miniaturization has become the driving force to engineer more practical and low-cost systems in medical and technological applications [1]. Especially with the advancement of micro and nanotechnologies, and their simplified and more commonly available fabrication methods, microelectromechanical systems have emerged in many applications of automobile, telecommunication, biomedical instrumentation, and robotics industries [2,3]. There has been also a significant advancement in materials research that is investigating more reliable and low-cost materials for a wide range of applications [4,5]. Both with the new materials and advanced microfabrication tools, miniaturized systems including microfluidics have become available. Microfluidics is a sub-field of the microelectromechanical systems in which the standard micro and nanofabrication tools of the semiconductor industry such as photolithography and wet/dry etching procedures are adopted [6]. After the introduction of the soft-lithography and replica molding techniques, the field of microfluidics has spawned numerous on-chip devices for performing various tasks including sample processing and disease diagnostics [7]. Flow rate control in microfluidic systems is an important requirement for these applications. While the motivation and the goal of this new field are to reduce the cost of testing, analysis and diagnostics in biomedical research, and eliminate the dependence on central facilities, the requirement of peripheral elements such as pumps and flow regulators to drive the microfluidic lab-on-a-chip devices hinders their wide-spread implementation.

Various technologies have been developed to provide fluid manipulation on small scale for lab-on-a-chip applications [8,9]. In a general sense, the microfluidic pumping devices are divided into two groups, namely active and passive pumping platforms [10]. In the passive fluid manipulation scheme including surface tension and capillary-based approaches, no external power sources are required which is one of the main advantages of these types of microfluidic pumps [11]. However, it is not possible to provide any fluid rate control with the passive devices which are also application-specific and do not provide very precise fluid flow control. On the other hand, the active microfluidic pumps use external forces to control the fluid flow which provides fluid flow rate [12]. There are various types of active pumps including magnetic field-driven pumps, acoustofluidic pumps, electric field-driven pumps, laser power pumps, and peristaltic pumps [13]. In the magnetic pumps, an external magnetic field is applied to rotate an internal structure or particle which in turn can actuate fluid in microfluidic channels [14]. Another type of magnetic pump is magnetically actuated cilia that are implementing magnetic cilia beating motion to induce fluid actuation [15]. While it is easy to control the rate and direction of fluid flow in most of the magnetic field-driven pumps, these types of pumps require an exter-

* Corresponding author
Email: sgucluer@adu.edu.tr

European Mechanical Science (2021), 5(4): 201-205
doi: https://doi.org/10.26701/ems.876597
Received: February 8, 2021
Accepted: March 31, 2021

nal magnetic field strong enough to couple with the internal structure and generate rotation/actuation. Besides, the cilia-based magnetic pumps are not very effective to generate a uniform flow rate. Similarly, an electric field is labored in microfluidic fluid pumping by implementing external electric fields, but peripheral systems to generate the external electric field are generally bulky and expensive [16]. Laser beams are utilized in microfluidic platforms to drive fluid motion with precision owing to the resolution and high power of the laser systems [17]. While the laser beam-driven fluid pumps enable such high dexterity in terms of precision, they depend on very complex and costly optical setups which are very problematic for lab-on-a-chip systems that are meant for point-of-care and low-cost applications. A different type of active pump technology, acoustofluidic pumps rely on external equipment such as signal generators and power amplifiers to drive piezo actuators which are coupled to a microfluidic channel to enable fluid pumping [10]. In addition to the external field driven microfluidic pumps, peristaltic microfluidic pumps have also been widely explored as an active means of microfluidic fluidic pumping [18–23]. These devices commonly use a pneumatic actuation of arrays of chambers in a microfluidic channel to drive fluid flow. These devices generally require multilayer microfabrication steps due to their complex geometries [13]. Besides, their corresponding pneumatic actuation mechanisms are usually well-regulated pressurized inert gas supplies. Based on the limitations and shortcomings of the existing microfluidic fluid pumping approaches, there is still a demand for a simple-to-fabricate and easy-to-actuate microfluidic pump which can be adopted in lab-on-a-chip platforms.

Herein, a low-cost microfluidic peristaltic pump is demonstrated. To eliminate the complex fabrication requirements of lithographic mold preparation, the microfluidic molds are printed using a commercial-grade 3D printer. 3D printing significantly reduced the cost of the system which is critical to enable the end product to low-resourced researchers. Polydimethylsiloxane (PDMS) microfluidic channels are prepared with the soft-lithography process. Fluid actuation is enabled by a battery-powered stepper motor which in turn rotates 3.15 mm diameter ball-bearings housed in a 3D printed holder. Overall, the presented microfluidic pump is simple, open-sourced, and versatile in fluid flow rate and direction control. This device can be potentially adopted in numerous lab-on-a-chip applications for enabling battery-powered microfluidic fluid control.

2. MATERIALS AND METHODS

To fabricate the peristaltic pumping device, motor holder, microfluidic chip holder, bearing ball assembly and the entire electronic housing parts (Figure 1a) are designed and printed in a commercial-grade fuse deposition modeling (FDM) type 3D printer (i3 Mega, Anycubic, China). FDM printers are commonly available to consumers due to their relatively low-cost. As for the printing material, polylactic acid which is also referred to as PLA filament with 1.75 mm diameter is used. PLA is an easy to print and relatively safer biodegradable material. An open-sourced slicing software, Cura, is used to generate G-codes for the printer. 100 % infill, 205 °C nozzle temperature, 0.4 mm nozzle diameter, 60 °C print bed temperature, 100 % cooling, 50 mm/s print speed, 0.1 mm layer height, and zig-zag filling pattern are used as the printing parameters. For the microfluidic chip, a master mold is printed using PLA (Figure 1b). Polydimethylsiloxane (PDMS) is mixed with a 10:1 ratio and poured into the PLA mold. After curing at 45 °C for 12 hours, the PDMS microfluidic channel is pealed from the mold, and the inlet and the outlet are punched using a reusable biopsy punch. Then, a 1 mm thick PDMS layer is bonded on top of the PDMS channel using a home-made hand-held high-frequency plasma generator. After the plasma treatment and contact bonding process, the PDMS closed channel is baked at 60 °C for 12 hours for better bonding.

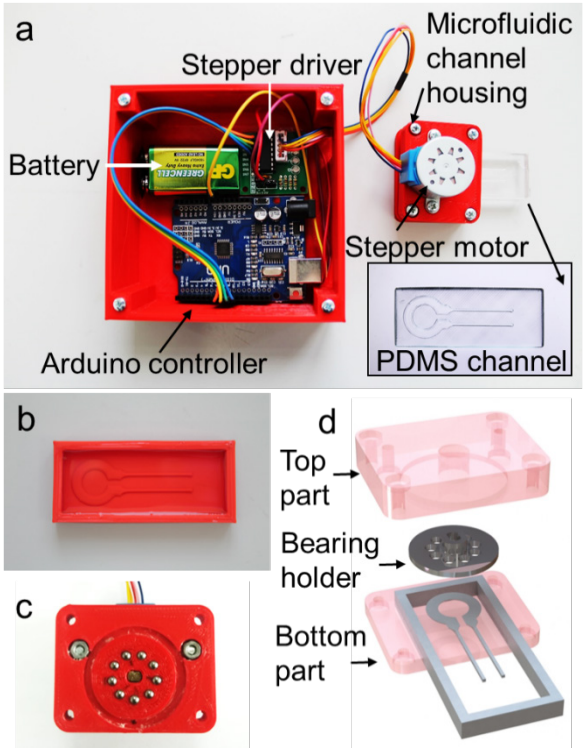

Figure 1. Developed peristaltic pump assembly and schematic. a) Electronic controller unit and the peristaltic pumping sections are shown. The inset is the polydimethylsiloxane (PDMS) channel. b) PLA mold for the PDMS is shown. c) ball bearing housing assembly is shown. d) Microfluidic chip holder and ball bearing housing assembly are schematically depicted.

To drive the fluid, nine 3.15 mm diameter stainless steel ball bearings are placed into a 3D printed housing assembly which is inserted into the shaft of the stepper motor on the reverse side (Figure 1c). The PDMS chip holder and bearing ball housing assembly are designed to be aligned so that the ball bearings have coincided with the circular section of the microfluidic channel (Figure 1d). the microfluidic channel dimensions are given in Figure 2. The circular section of the microfluidic channel is designed to be wider than

the diameter of the ball bearings to include the thickness of the thin PDMS membrane. The main components and the work-flow diagram of the peristaltic pump are shown in Figure 3. The system is composed of an electronic control unit, a stepper motor (28BYJ-48), and a microfluidic chip. The stepper motor is chosen due to its lower cost compared to the other stepper motors including Nema series motors. 28BYJ-48 Stepper motor has 4096 and 2048 steps per revolution for half and full step modes, respectively. In this work, it is used in the half-step mode which results in a 0.0879° step angle. The flatted shaft of the motor made it easier to couple to the 3D printed ball-bearing housing. The stepper motor is controlled by a ULN2003 stepper motor driver controlled by an Arduino Uno board. Arduino boards have become the power-house of open-source hardware and development kits in the last decade due to their low-cost and simple programming requirements. The entire system can be supplied with a 9-volt battery to obtain a portable system. For the characterization of the peristaltic pumping system in the experimental conditions, an adjustable DC power supply is used.

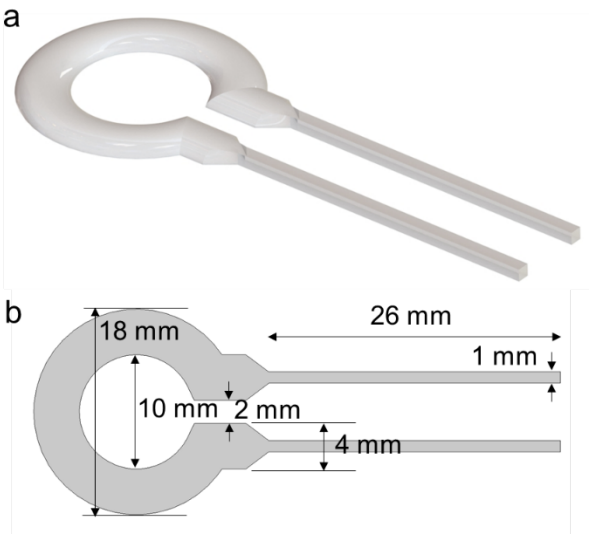

Figure 2. Microfluidic channel dimensions. a) A 3D rendered schematic of the fluidic path. b) actual dimensions of the fluidic channel.

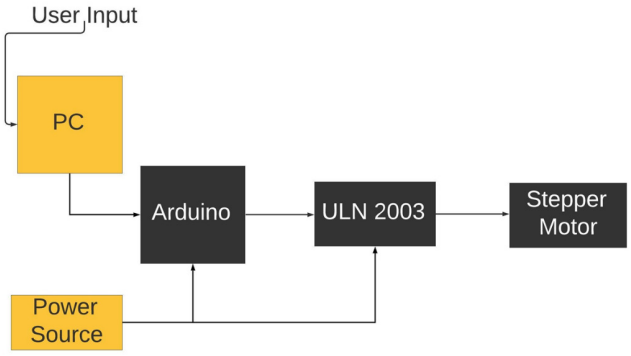

Figure 3. Primary elements and the work-flow of the peristaltic pump.

3. RESULTS AND DISCUSSION

In the working principle of the peristaltic pump, the rotation rate (RPM) of the stepper motor is used as the externally controlled variable to adjust the flow rate. Flow rate direction can also be controlled by reversing the motor rotation direction. RPM and motor rotation direction is controlled by the Arduino board. The programming requirement for these tasks is very simple and easy to adjust for specific needs. Figure 4 includes the simple code for the Arduino for a specific RPM input. The RPM input of this specific style of the stepper motor is adjusted by the rotation step parameter. In the Arduino code, first a commonly used stepper library called "AccelStepper" is included to incorporate the required definitions and commands into the Arduino environment. After that, motor pins are defined concerning the pins of the Arduino board. Arduino and the motor interface type are selected to drive the stepper motor in half-step mode by the predefined interface type 8 in the library. Then, the motor rotation speed (RPM) is defined by the step count per unit time in the "setspeed" command. By changing the step count, stepper motor RPM values from 28 to less than 2 RPM are obtained.

```
// Include the AccelStepper library:
#include <AccelStepper.h>
// Motor pin definitions:
#define motorPin1 8 // IN1 on the ULN2003 driver
#define motorPin2 9 // IN2 on the ULN2003 driver
#define motorPin3 10 // IN3 on the ULN2003 driver
#define motorPin4 11 // IN4 on the ULN2003 driver
// Define the AccelStepper interface type; 4 wire motor in half step mode:
#define MotorInterfaceType 8
// Initialize with pin sequence IN1-IN3-IN2-IN4 for using the AccelStepper library
with 28BYJ-48 stepper motor:
AccelStepper stepper = AccelStepper(MotorInterfaceType, motorPin1, motorPin3,
motorPin2, motorPin4);
void setup() {
// Set the maximum steps per second:
stepper.setMaxSpeed(2000);
}
void loop() {
// Set the speed of the motor in steps per second:
stepper.setSpeed(500);
// Step the motor with constant speed as set by setSpeed():
stepper.runSpeed();
}
```

Figure 4. An example Arduino Uno code to control the stepper motor RPM.

The wiring of the Arduino Uno, stepper motor driver, and stepper motor is also arranged to be compatible with the code. The wiring diagram is shown in Figure 5. In the wiring, IN1, IN2, IN3, and IN4 of the driver is connected to pin 8, 9, 10, and 11 of the Arduino, respectively. The stepper driver and the Arduino board are supplied with a positive voltage (from 5 V to 12 V) and a negative ground terminal. It is also possible to power the Arduino with the PC USB connection, but Arduino one of the ground pins is still required to be connected to the same ground of the stepper driver. Powering both the Arduino and the stepper driver with a portable power source is more desirable for lab-on-a-chip applications in remote sites with limited resources as well as for point-of-care diagnostics. The system presented in this study targets a minimalistic and low-cost approach to enable simplicity and dexterity in fluid manipulation on small scale. Therefore, the components, their assembly, and operation are crafted to serve the needs of developing countries.

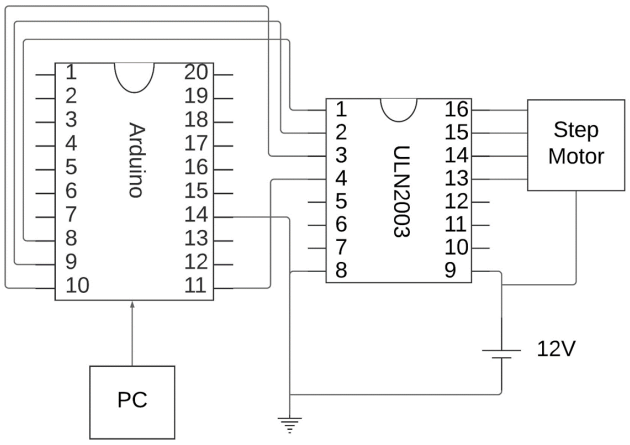

Figure 5. wiring diagram of the electronic components and the stepper motor of the control system.

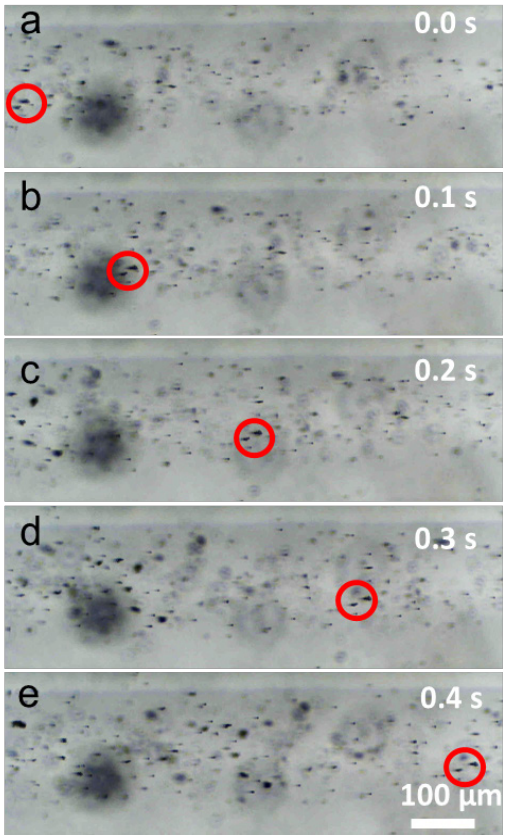

Figure 6. Characterization of flow rate via tracing suspended inclusions in the water medium. a-e) A cluster of polymer particles is tracked within the visible section of the microfluidic channel to calculate the fluid velocity and corresponding volumetric flow rates.

After completing the electronic control unit and the entire system assembly, the peristaltic pump is tested with water and polystyrene bead solution. Polystyrene beads with 5-micrometer diameters are introduced into the water medium to obtain flow characterization markers. The device characterization is completed using 3 different microfluidic chips. For each case, RPM values of the stepper motor are used as the controlled variable to obtain gradually increasing flow rates. The experiments with each RPM value are repeated at least three times for every microfluidic chip. For calculating the volumetric flow rates, polystyrene beads are tracked in collecting videos, and the bead velocities are calculated by dividing the travel distance by the time duration. Finally, the velocity of the fluid flow is multiplied with the inner cross-sectional area of the microfluidic channel to obtain the volumetric flow rate in microliters/seconds. For each RPM value, at least 6 beads are tracked, and the standard deviation of all the repeated experiments is used as the error bars in the data presented. An example of particle tracking and flow characterization is shown in Figure 6. As it is observed from the figure a polymer particle cluster is traced as a function of time. In this example, the calculated flow rate is 1.7 µL/s which corresponds to around 1.5 RPM stepper motor rotational speed.

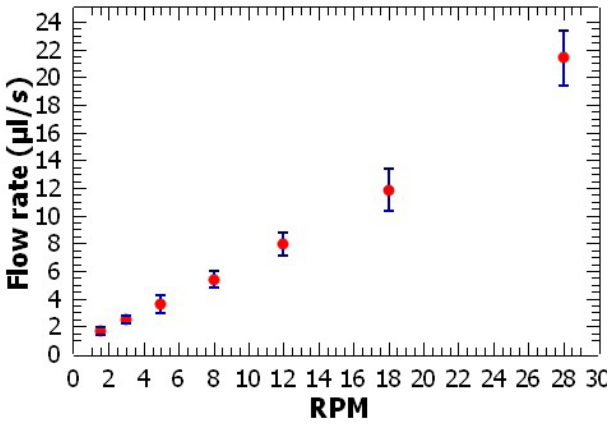

Figure 7. Volumetric flow rate versus rotational speed of the stepper motor. The standard deviations represent at least 18 repeated measurements for each RPM value.

4. CONCLUSION

In this study, a portable and low-cost peristaltic microfluidic pump is presented for providing controllable fluid flow manipulation for lab-on-a-chip applications. Considering the increasing need for more affordable and accessible medical care and disease testing, point-of-care devices and on-chip sample processing are becoming even more important in today's world where global outbreaks and pandemics are rising. To achieve, the goal of rapid testing and diagnostics using the lab-on-a-chip approaches, the fundamental necessity is to provide flow-controlled fluid manipulation in these on-chip devices. The peristaltic pump presented in this work does not rely on complex cleanroom microfabrication methods which are critical for enabling wide-spread adaptation of this device for the researchers in the developing world where resources are limited. A simple 3D printing tool, which is commonly available even as a house-hold item, is implemented to fabricate various parts of the system from a low-cost material. Furthermore, the master mold for the PDMS soft-lithography process is also 3D printed as a single-layer architecture. The PDMS membrane is simply poured into a petri dish and cured. Overall, the entire device fabrication can be done in any laboratory with commonly found items and tools. Besides, the control and the actuation of the peristaltic pump are provided by an Arduino Uno

board and a low-cost stepper motor, respectively. Arduino Uno has wide-spread usage and is adopted by even middle school students to be applied in coding and project building. Finally, the system presented here can be powered by a simple 9 V battery to obtain a portable system that does not rely on peripheral devices or other infrastructures. Characterization of the pumping performance of the device yielded a flow rate interval between 1.7 µL/s to 23 µL/s which is adequate for enabling on-chip bioanalysis and disease testing. With its low-cost, simplicity, and flow control dexterity, this peristaltic pumping system can potentially be adapted to many lab-on-a-chip applications.

REFERENCES

[1] Franke, T.A., Wixforth, A., (2008). Microfluidics for miniaturized laboratories on a chip. Chemphyschem : A European Journal of Chemical Physics and Physical Chemistry. 9(15): 2140–56. doi: 10.1002/cphc.200800349.

[2] Ozcelik, A., (2019). Atomic Layer Deposition (ALD) of Vanadium Oxide Thin Films. Turkish Journal of Electromechanics and Energy. 4(2): 13–8.

[3] Kaynak, M., Ozcelik, A., Nama, N., Nourhani, A., Lammert, P.E.P.E., Crespi, V.H.V.H., et al., (2016). Acoustofluidic actuation of in situ fabricated microrotors. Lab Chip. 16(18): 3532–7. doi: 10.1039/C6LC00443A.

[4] Yıldızhan, Ş., Çalık, A., Özcanlı, M., Serin, H., (2018). Bio-composite materials: a short review of recent trends, mechanical and chemical properties, and applications. European Mechanical Science. 2(3): 83–91. doi: 10.26701/ems.369005.

[5] Serin, H., Yildizhan, S., Ozcanli, M., Akar, M.A., (2018). Micro hardness and water absorption properties of Cotton/Epoxy Bio-Composite. Journal of Biotechnology. 280: S91. doi: 10.1016/j.jbiotec.2018.06.299.

[6] Ayan, B., Ozcelik, A., Bachman, H., Tang, S.-Y.S.-Y., Xie, Y., Wu, M., et al., (2016). Acoustofluidic coating of particles and cells. Lab Chip. 16(22): 4366–72. doi: 10.1039/C6LC00951D.

[7] Zhang, P., Bachman, H., Ozcelik, A., Huang, T.J., (2020). Acoustic Microfluidics. Annual Review of Analytical Chemistry. 13(1): 17–43. doi: 10.1146/annurev-anchem-090919-102205.

[8] Zhang, C., Xing, D., Li, Y., (2007). Micropumps, microvalves, and micromixers within PCR microfluidic chips: Advances and trends. Biotechnology Advances. 25(5): 483–514. doi: 10.1016/J.BIOTECHADV.2007.05.003.

[9] Akkoyun, F., Ozcelik, A., (2020). A Simple Approach for Controlling an Open-Source Syringe Pump. European Mechanical Science. 4(4): 166–70. doi: https://doi.org/10.26701/ems.769837.

[10] Ozcelik, A., Aslan, Z., (2021). A practical microfluidic pump enabled by acoustofluidics and 3D printing. Microfluidics and Nanofluidics. doi: 10.1007/s10404-020-02411-w.

[11] Walker, G.M., Beebe, D.J., (2002). A passive pumping method for microfluidic devices. Lab on a Chip. 2(3): 131–4. doi: 10.1039/b204381e.

[12] Wu, Z., Cai, H., Ao, Z., Nunez, A., Liu, H., Bondesson, M., et al., (2019). A Digital Acoustofluidic Pump Powered by Localized Fluid-Substrate Interactions. Analytical Chemistry. 91(11): 7097–103. doi: 10.1021/acs.analchem.9b00069.

[13] Au, A.K., Lai, H., Utela, B.R., Folch, A., (2011). Microvalves and micropumps for BioMEMS. Micromachines. 2(2): 179–220. doi: 10.3390/MI2020179.

[14] Chen, Z., Noh, S., Prisby, R.D., Lee, J.B., (2020). An implanted magnetic microfluidic pump for in vivo bone remodeling applications. Micromachines. 11(3): 1–10. doi: 10.3390/mi11030300.

[15] Zhang, S., Wang, Y., Lavrijsen, R., Onck, P.R., den Toonder, J.M.J., (2018). Versatile microfluidic flow generated by moulded magnetic artificial cilia. Sensors and Actuators, B: Chemical. 263: 614–24. doi: 10.1016/j.snb.2018.01.189.

[16] Studer, V., Pépin, A., Chen, Y., Ajdari, A., (2002). Fabrication of microfluidic devices for AC electrokinetic fluid pumping. Microelectronic Engineering. 61–62: 915–20. doi: 10.1016/S0167-9317(02)00518-X.

[17] Maruo, S., Inoue, H., (2007). Optically driven viscous micropump using a rotating microdisk. Applied Physics Letters. 91(8): 1–4. doi: 10.1063/1.2768631.

[18] Sönmez, U., Bekin, M., Trabzon, L., (2018). Design and Fabrication of Integrated Microchannel and Peristaltic Micropump System for Inertial Particle Separation. MATEC Web of Conferences. 153: 08002. doi: 10.1051/matecconf/201815308002.

[19] SOBH, A.M., (2008). Interaction of couple stresses and slip flow on peristaltic transport in uniform and nonuniform channels. Turkish J. Eng. Env. Sci. 32(2): 117–23.

[20] Srinivasacharya, D., (2008). The effects of wall properties on peristaltic transport of a dusty fluid. Turkish Journal of Engineering and Environmental Sciences. 32(6): 357–65.

[21] Hayat, T., Abbasi, F.M., (2010). Peristaltic Mechanism in an Asymmetric Channel with Heat Transfer. Mathematical and Computational Applications. 15(4): 621–37.

[22] Elangovan, K., Dar, A.A., (2017). Impact of an inclined magnetic field, heat generation/absorption and radiation on the peristaltic flow of a Micropolar fluid through a porous non-uniform channel with slip velocity. New Trends in Mathematical Science. 3(5): 227–44. doi: 10.20852/ntmsci.2017.198.

[23] Yang, Y.N., Hsiung, S.K., Lee, G. Bin., (2009). A pneumatic micropump incorporated with a normally closed valve capable of generating a high pumping rate and a high back pressure. Microfluidics and Nanofluidics. 6(6): 823–33. doi: 10.1007/s10404-008-0356-7.

EUROPEAN MECHANICAL SCIENCE
e-ISSN: 2587-1110

Research Paper

Hybrid Taguchi Based Grey Algorithm for Multi Objective Optimization of Gas Metal Arc Welded DP1000 Steel

Murat Karataş[1], Melih Bayramoğlu[2], Uğur Eşme[3*], Necdet Geren[4]

[1]Gedik Welding Company, Turkey
[2,4]Cukurova University, Department of Mechanical Engineering, Adana, Turkey
[3]Tarsus University, Department of Mechanical Engineering, Mersin, Turkey

Abstract

Euro-6 norms for reduction of CO_2 emissions and ECE-R66-01 regulation for safer passenger transportation became legislative obligations for bus builders. These two adaptations increase the weight of a bus as nearly 600kg which also increases the fuel consumption nearly 1.5-3%. Dual phase (DP) steels can compensate these increases by decreasing the thickness of the components. Because, ferrite provides the steel with good formability and martensite increases the hardness and ultimate tensile strength in DP steels. This study focused on the multi response hybrid optimization of gas metal arc welding (GMAW) of DP1000 steel to determine the optimal parametric combination which gives the maximum ultimate tensile strength (UTS, MPa) and joint efficiency (JE) under minimum heat input (Q, kj/mm). Nine experimental trials which is based on the orthogonal array suggested by Taguchi method was carried out to investigate objective functions for optimization in the experimental range of GMAW parameters such as voltage (U, volt), welding speed (V, mm/min) and wire feed rate (f, m/min). The Taguchi method continued with Grey Relational Analysis (GRA) to overcome the multi-objective optimization model. Finally, Analysis of variance (ANOVA) method has been used to determine the significance of the welding parameters on the responses of UTS, JE and Q. This shows flexible applicability of Taguchi based GRA to find out the effect of each GMAW process parameters onto individual responses.

Keywords: DP1000 steel, Taguchi method, Gas Metal arc welding, Grey relation optimization

1. INTRODUCTION

The passenger safety, comfort and the fuel consumption are the most significant commercial factors for bus builders. While the global demand for fuel consumption is increasing, some standards such as Euro-6 norms for reduction of CO2 emissions and ECE-R66-01 regulation for safer passenger transportation become legislative obligations for bus builders [1]. These two adaptations increase the weight of a bus structure as nearly 600kg which also increases the fuel consumption nearly 1.5-3%. The most effective methods to compensate this increase in fuel consumptions without any loss on passenger safety and comfort can be improved by redesigning bus body aerodynamics, chemical changes on the consumed fuel, engine efficiency improvement, and reduction on the structure weight. Among these applications, reducing the vehicle weight is the most effective and applicable method for fuel economy [1].

Reducing the weight includes redesigning the bus body structure and use of higher strength to weight ratio steels. Unfortunately, geometrical design changes on bus structure have limited potential to compensate the weight increase which is caused by the legislative obligations. Thus, the best way to compensate the weight increase is decreasing the thickness of the parts by using higher strength structural steels.

Gas metal arc welding (GMAW) process produces an electric arc between a consumable wire electrode and the workpieces to melt and join base materials. The filler metal is fed automatically from the wire feeder mechanism, through a liner, then out of a contact tip in the torch. In this process, CO_2 or mixture gas (combinations of Ar, He, CO_2 and O_2) are used to prevent oxidation and diffusion of H_2 and N_2 to the molten metal. GMAW process can be applied semi-automatic or fully automatic. Figure 1 shows the basic schematic representation of GMAW process.

The GMAW process is mostly performed on lower grades of DP steels such as DP480 and DP600, however, it can also be used to weld higher strength grades (DP780, DP1000).

* Corresponding author
Email: esme@tarsus.edu.tr

European Mechanical Science (2021), 5(4): 206-213
doi: https://doi.org/10.26701/ems.941934
Received: May 24, 2021
Accepted: August 31, 2021

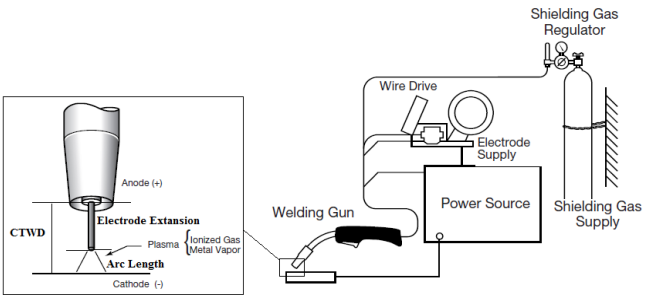

Figure 1. A general schematic representation of a GMAW system [2]

But, martensite tempering percentage and decrease in UTS increase with higher grade DP steel usage at the same heat input. However, GMAW is the mostly applied technique in bus building industry, because it is the fastest and most applicable welding method for joining of rectangular cross-sectional profiles [1]. Literature survey shows that there are various studies in the literature dealing with modeling and optimization of GMAW using different kind of workpiece materials and optimization techniques. Martinez et al. [3] developed a framework for the prediction of weld bead and penetration geometry in GMAW process using deep learning and machine learning techniques. Huang et al. [4] proposed ensemble empirical mode decomposition with adaptive noise and extreme learning machine for online control the weld quality diagnosis of GMAW process. Sivasakthivelet. al. [5] developed a back propagation neural network model for the prediction of bead geometry in gas metal arc welded stainless steel plates. Chauhan et al. [6] used Taguchi technique in GMAW process for optimization of gas metal arc welded AISI 1018 mild steel plates. Aghakhani et al. [7] optimized GMAW process by Taguchi method on weld dilution. Kumar et al. [8] implemented the Taguchi method followed by grey relation analysis to optimize gas metal arc welding process parameters for multi performance characteristics of bead width and height, weld penetration and heat affected zone using AISI 1020 steel. Rizvi et al. [9] investigated the optimization for SS304H steel using Taguchi based grey relational analysis. Arya et al. [10] showed the influence of welding parameters in metal inert gas welding process using Taguchi based grey relation analysis. Esme et al. [11] optimized quality characteristics of the tungsten inert gas welding parameters such as weld bead, weld height, penetration, heat affected zone and ultimate tensile strength using Taguchi combined grey relational analysis method. Srivastava et al. [12] used Box Behnken design technique of Response Surface Methodology to optimize gas metal arc welding for IS 2062 mild steel. Singla et al. [13] developed a mathematical model for the parametric optimization of gas metal arc welding by using factorial design approach. Ambekar et al. [14] presented a study by using Taguchi orthogonal array of $L_{16}$for optimization of process parameters gas metal arc welding on AISI 410 steel. Yadav et al. [15] made parametric optimization tensile strength in GMAW by performing Taguchi method. Sreeraj et al. [16] made an optimization study for gas metal arc welding parameters using central composite rotatable design and particle swarm method. Shao et al. [17] developed a mathematical model using design of experiments and polynomial regression method for modeling and optimization of gas metal arc welding method. Kshirsagar et al. [18] used Hybrid Nelder Mead-Evolutionary algorithms to develop a model for optimization purpose and comparison of this method with the others.

The Taguchi method proposed by Genichi Taguchi in 1950s is very famous and fast tool to improve and solve optimization of in all kind of manufacturing process [11,19]. This technique offers an opportunity to design the experiments called orthogonal design matrix with a minimum number of trials. The approach also uses the signal to noise ratio (S/N) to serve the objective role within the experimental range to be optimized (maximized). On the other hand, Taguchi method alone cannot solve the multi objective optimization problem. Taguchi method combined with GRA may overcome this problem and solve the multi-response designed problems in a wide range of engineering applications. Taguchi technique successfully uses orthogonal arrays to build the experiments in optimization.

In the present study, it is aimed to determine the optimum process parameters such as welding voltage (U, volt), welding speed (V, mm/min) and wire feed rate (f, m/min)in GMAW process to generate required weld quality in respect of ultimate tensile strength (UTS, MPa), joint efficiency (JE) and heat input Q (kj/mm). Hybrid combination of grey relation analysis and Taguchi approach for multi objective optimization has been performed to determine the optimum process condition for GMAW process. Finally, the analysis of variance (ANOVA) and confirmation test were applied in order to examine the contribution of each welding factors and to check the optimum results.

2. GREY RELATIONAL ANALYSIS APPROACH AND TERMINOLOGY

Although the black region of the grey relational analysis (GRA) contains no information, the white region contains information completely. The grey system, on the other hand, denotes the degree of detail between white and black. In other words, while some information is known in the grey system, but some is unknown. GRA is one of the subtitles of grey modeling. The each factor in the system compared with reference sequence to determine the relationship degree between the factors [19].

First, experimental data is normalized starting from zero to one according to the normalization criterions: i. *smaller-the-better*, ii. *Larger-the-better* and iii. *ideal-the-better*. This is named as Grey relational generation. Grey relational coefficient (GRC) for each experimental level is then determined using normalized values in order to find the relationship in between actual and desired data. Averaging the corresponding GRC for the selected response yields the overall Grey relational grade (GRG). So, GRG which is also performance characteristic of the multiple response is converted

Table 1. Mechanical properties and chemical composition (wt.%) of DP1000 steel [20]

Chemical composition (wt. %)	Si	P	C	Mn	Nb	S	Al
	0.50	0.01	0.15	1.50	0.015	0.02	0.04
Mechanical properties	Tensile strength (MPa)		Yield strength (MPa)		Hardness ($HV_{0.5}$)		Elongation (%)
	1000		1000		320		7

into a single response optimization [11,19]. The highest GRG in the system is the optimal parametric combination. Lastly, Taguchi method is applied to maximize the overall GRG for optimal parameter setting.

In Grey relational generation calculation of this work, the *larger-the-better* (LB) criterion is used to calculate the normalized reference sequences for ultimate tensile strength and joint efficiency. LB criterion is expressed as [19]:

$$x_i(k) = \frac{y_i(k) - \min y_i(k)}{\max y_i(k) - \min y_i(k)} \quad (1)$$

Heat input relates to the *smaller-the-better* (SB) criterion. It is expressed as:

$$x_i(k) = \frac{\max y_i(k) - y_i(k)}{\max y_i(k) - \min y_i(k)} \quad (2)$$

hereby, $x_i(k)$ is determined after GRG, $\min y_i(k)$ is the lowest $y_i(k)$ value associated with the k^{th} response, and $\max y_i(k)$ is the highest $y_i(k)$ value related to the k^{th} response. For the responses, the reference series is $x_0(k)$ (k=1,2,3.....,9). In the process of GRG analysis, the concept of the grey relational degree is to demonstrate the degree of the relationship between 9 sequences [$x_0(k)$ and $x_i(k)$, i=1,2,3.....,9]. The relational coefficient of grey (GRC) is measured as [19]:

$$\xi_i(k) = \frac{\Delta_{\min} + \psi\Delta_{\max}}{\Delta_{0i}(k) + \psi\Delta_{\max}} \quad (3)$$

hereby, $\Delta_{0i} = \|x_0(k) - x_i(k)\|$ is the absolute value difference between $x_0(k)$ and $x_i(k)$; ψ is the distinguishing multiplier $0 \le \psi \le 1$; $\Delta_{\min} = \forall j^{\min} \in i \forall k^{\min} \|x_0(k) - x_j(k)\|$ is the lowest value of Δ_{0i}; and $\Delta_{\max} = \forall j^{\max} \in i \forall k^{\max} \|x_0(k) - x_j(k)\|$ is the highest value of . After taking the mean of coefficients of Grey relational analysis, the GRG γ_i is calculated as [19]:

$$\gamma_i = \frac{1}{n}\sum_{k=1}^{n} \xi_i(k) \quad (4)$$

hereby, the number of welding responses is expressed by n. The higher the GRG value, the greater the relation between the given sequence $x_i(k)$ and comparison sequence. The best sequence is the reference sequence $x_0(k)$; hence, a higher GRG indicates that the acquired parameter combination is approaching the optimum value. Both the GRG main effect graph and the average response for the GRG are extremely important in deciding the optimum welding process conditions [19].

3. MOTIVATION AND EXAMINATION RESULTS OF EXPERIMENTS

3.1. Description of Experiments

The purpose of this study is multi objective optimization of GMAW process parameters for improving mechanical properties of DP1000 steel joint [1]. For this aim, the effects of GMAW parameters on mechanical performance and welding quality of 1.2mm DP1000 plates were investigated. The dimensions of the DP1000 plates and welding design were defined depending on TS 6868-1 EN 287-1 standard. Therefore, 300x150 mm dimensions of DP1000 steel plates were used for butt welding. The mechanical properties and chemical composition (wt.%) of the used workpiece material is depicted in Table 1.

An automated GMAW system was designed and built to provide consistent linear welds and to eliminate the welding defects, which can be caused by the welder. In this way, free wire length was kept constant. The components of welding automation system used in this study is shown in Figure 2.

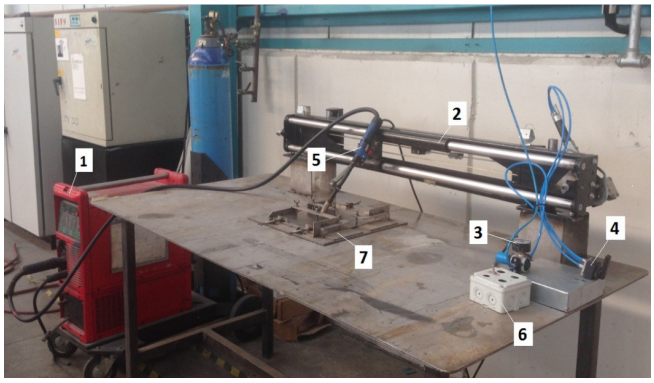

Figure 2. Components of the automated welding system used for experimental work: (1) Fronius Transpuls Synergic 2700 welding power supply, (2) Pneumatic welding automation mechanism, (3) Pneumatic valve to control welding speed, (4) Pneumatic valve to control welding start/stop and direction, (5) GMAW torch, (6) Welding arc start/stop control panel and (7) Welding fixture

Fronius Transpuls Synergic 2700 welding power supply, which had 270A current capacity is employed for welding applications. The welding wire is selected as 0.8mm and ER70S-6 (AWS 5.18) standard.100% CO_2 under the constant flow rate of 8 L/min is used as a shielding gas. Also, direct current electrode positive (DCEP) polarity is utilized for better penetration, arc stability, higher electrode melting rates and lower heat input to workpiece. The welding current start and stop functions are controlled with an adapted on/off switch panel. The welding automation system is propelled using a pneumatic activation system which is used to adjust welding speed (valve-3) and direction (valve-4). In order to prevent lost welding designs due to the welding deformation, a workpiece clamping fixture is produced as shown in Figure 3.

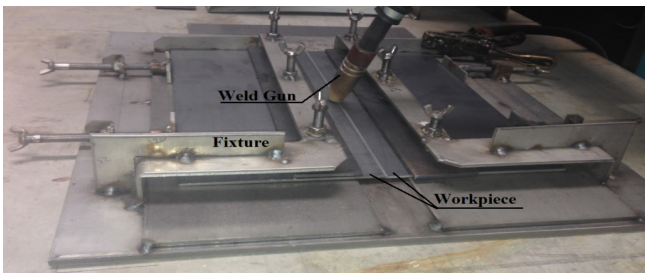

Figure 3. Welding fixture used in the experiments

Samples which is prepared according to transverse tensile test method of EN 895 were taken from the weld zone centered in the gage length. After, they were loaded to tensile test machine to measure the ultimate tensile strength.

3.2. Experimental Procedure and Results

In a full factorial experimental plan, increasing the number of parameters and their levels raises the cost, time and especially experimental runs exponentially [11,19]. In order to avoid these negative effects under a limited number of experimental runs, Taguchi's L_9 orthogonal array, which consists of 9 data sets, was used.

Experimental runs have been carried out in according to the welding parameters illustrated in Table 2 given below. Welding current (I, A) was adjusted according to the wire feed rate level; for f_1=2.20m/min I=45A, f_2=2.40m/min I=53A and for f_3=2.60m/min I=60A.

Table 2. Level of GMAW parameters

Welding parameters	Notation	Unit	Parameter Levels		
			1	2	3
Voltage	U	volt	17.50*	18.50	19.50
Welding speed	V	mm/min	260*	320	380
Wire feed	f	m/min	2.20* (I=45A)	2.40 (I=53A)	2.60* (I=60A)

*Initial GMAW parameter setting

Energy generated by the power source E (kj/mm) can be calculated as [20]:

$$E = \frac{UxIx60}{Vx1000} \quad (5)$$

where U = Voltage (Volt), I = Current (A) and V = Welding Speed (mm/min).

In order to calculate the heat input more accurately, the arc efficiency (η) is taken as 0.8 for the present GMAW welding process. Finally, the following formula is used for calculating the welding heat input (Q, kj/mm) [20];

$$Q = \eta xE \quad (6)$$

The ratio of the strength of a welded joint to the strength of the used base material is known as joint efficiency (JE). L_9 Taguchi's orthogonal array that shows the 9 sets of coded experimental condition corresponding to UTS, JE and Q are shown in Table 3. For the evaluation of the optimum GMAW parameter combination needed to overcome the required weld quality within the studied region, all these data were used for grey relationship analysis.

The welding samples of DP1000 steel were visually inspected according to EN ISO 3834 standard [1]. Therefore, Level-C which has medium tolerances for imperfections was used as a guide on the quality levels of butt welding. Some of the visual inspected workpieces and their categorization is illustrated in Figure 4.

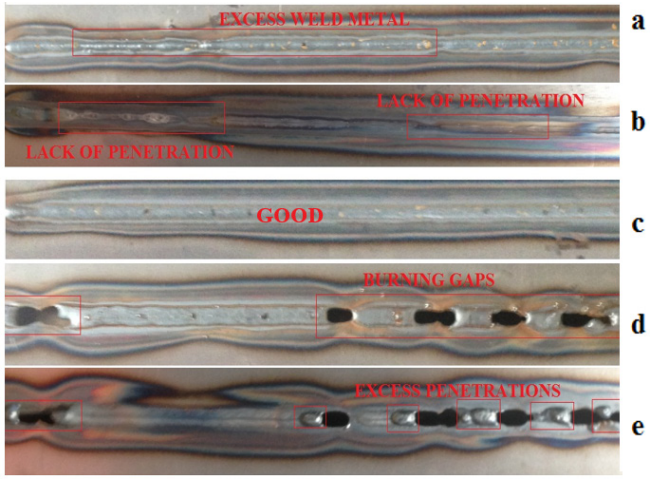

Figure 4. Visual categorization of weld inspection of the samples: (a) Excess weld metal, (b) Lack of penetration, (c) Good, (d) Burning gaps, (e) Excess penetration

4. GRA OPTIMIZATION OF GMAW PARAMETERS

4.1. Evaluation of Optimal Welding Condition

First, measured and calculated data is normalized for grey

Table 3. L_9 Orthogonal array and corresponding experimental and calculated results

Run no	Process parameter levels			Experimental results				
	U	V	f	UTS (MPa)	JE	Q (kj/mm)	Visual weld inspection	
							Cap	Root
1	1	1	1	794.125	0.794	0.145	Good	Good
2	1	2	2	795.785	0.796	0.139	Burning gap	Lack of Penetration
3	1	3	3	797.215	0.797	0.133	Good	Good
4	2	1	2	772.995	0.772	0.181	Burning gap	Good
5	2	2	3	786.235	0.786	0.167	Good	Good
6	2	3	1	808.04	0.808	0.105	Good	Burning gap
7	3	1	3	772.905	0.772	0.216	Burning gap	Excess penetration
8	3	2	1	796.715	0.796	0.132	Burning gap	Excess penetration
9	3	3	2	801.095	0.801	0.131	Good	Good

relation generation by using Eqs. (1) and (2) [11,19]. For each of the responses, the normalized data and the difference in absolute value (Δ_{0i}) were calculated and presented in Table 4 and Table 5, respectively.

Table 4. Normalization of the responses

Exp. run	UTS	JE	Q
	larger-the-better	larger-the-better	smaller-the-better
Reference series	1.000	1.000	1.000
1	0.604	0.611	0.640
2	0.651	0.667	0.694
3	0.692	0.694	0.748
4	0.003	0.000	0.315
5	0.379	0.389	0.441
6	1.000	1.000	1.000
7	0.000	0.000	0.000
8	0.678	0.667	0.757
9	0.802	0.806	0.766

Table 5. Δ_{0i} for each responses

Exp. run	UTS	JE	Q
Reference series	1	1	1
1	0.396	0.389	0.360
2	0.349	0.333	0.306
3	0.308	0.306	0.252
4	0.997	1.000	0.685
5	0.621	0.611	0.559
6	0.000	0.000	0.000
7	1.000	1.000	1.000
8	0.322	0.333	0.243
9	0.198	0.194	0.234

Distinguishing coefficient (ψ) is ranged between 0 and 1. Literature review shows that distinguishing factor does not affect the grey relational grade [8]. In this study it is taken as equal weight of 0.333 for each responses as $\psi_{UTS} = \psi_{E} = \psi_{Q} =$ 0.333. The determined Grey relational coefficients (GRC) for each response using Eq (3) are shown in Table 6.

Table 6. GRC for each responses

Exp. run	UTS	JE	Q
ψ	0.333	0.333	0.333
1	0.457	0.461	0.480
2	0.488	0.500	0.521
3	0.519	0.521	0.569
4	0.250	0.250	0.327
5	0.349	0.353	0.374
6	1.000	1.000	1.000
7	0.250	0.250	0.250
8	0.508	0.500	0.578
9	0.628	0.631	0.587

Then, it is followed by calculation of grey relational grade (GRG) which shows the total representative value of the responses. The multi-criteria optimization problem of the GMAW method is thus reduced to a basic optimization model using the Taguchi combined GRA. In this section, it should be noted that a higher GRG indicates that the factor combination is close to its optimal value. Table 7 shows the calculated GRG and their grade.

Table 7. GRG and their rank

Exp. run	GRG	Ranking
1	0.466	6
2	0.503	5
3	0.536	3
4	0.275	8
5	0.358	7
6	0.999	1
7	0.250	9
8	0.528	4
9	0.615	2

Now, the signal to noise (S/N) related to the larger-the-better criteria for overall GRG for each experiment is calculated using Eq. (7) [19]. Converted GRG into S/N ratio is presented in Table 8.

$$S/N = -10\log\left[\frac{1}{n}\sum_{i=1}^{n}\frac{1}{y_i^2}\right] \quad (7)$$

hereby, y_i is the experimental value i^{th} response in the j^{th} experiment at the k^{th} test, and n denotes the number of measurements.

Table 8. Mean grey grade and corresponding S/N ratios

Exp. run	S/N	Mean grey grade
1	-6.632	0.466
2	-5.969	0.503
3	-5.417	0.536
4	-11.213	0.275
5	-8.922	0.358
6	-0.009	0.999
7	-12.041	0.250
8	-5.547	0.528
9	-4.222	0.615

The highest S/N ratio means the optimum parameter setting for related process is in the experimental domain. Since a high S/N value has a much greater effect on responses than the noise factors of the random effects. Graphical representation of S/N ratio and GRG versus parameter level is given in Figure 5. The average of the GRG and S/N ratio on the plots symbolized as dashed line.

As shown in Figure 4, the optimal parameter combination for GMAW welding of DP1000 steel joint becomes $U_1V_3f_1$. Corresponding each level of average results for GRG and S/N ratios is presented in Table 9.

Delta statistics which is formulated as the maximum value minus minimum value indicates the relative size of each effect. According to delta analysis; welding speed has the highest rank value, wire feed and welding voltage have second and third rank values respectively.

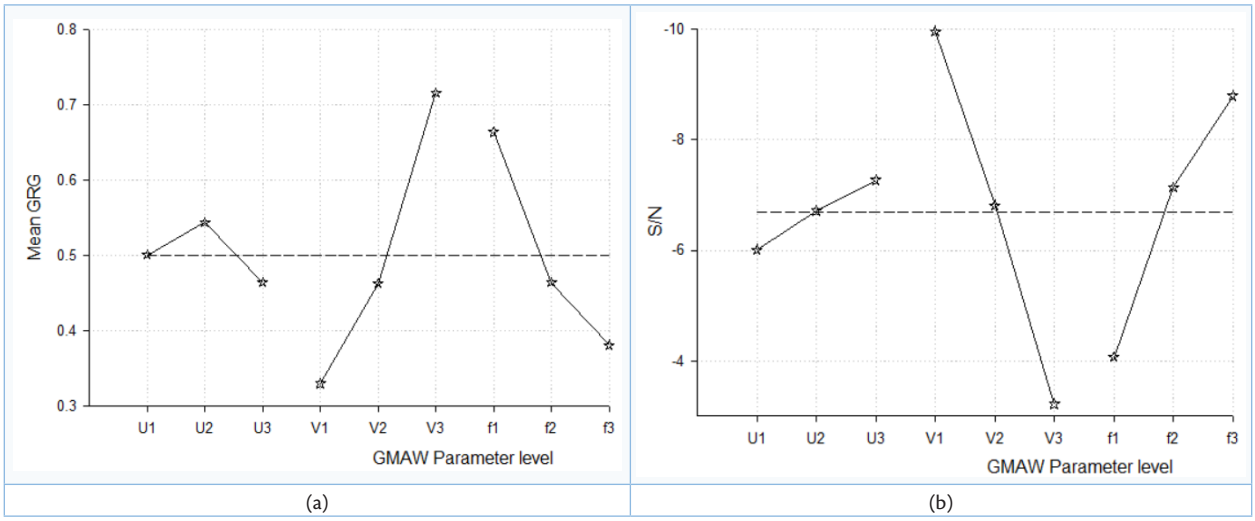

(a) (b)

Figure 5. (a) Mean GRG, (b) S/N

Table 9. Response results for mean GRG and S/N

Factors	Mean GRG				
	Level 1	Level 2	Level 3	Delta=max-min	Rank
U	0.501	0.544	0.464	0.079	3
V	0.330	0.463	0.716	0.386	1
f	0.664	0.464	0.381	0.283	2
Total mean Grey relational grade= 0.50					
Factors	S/N				
	Level 1	Level 2	Level 3	Delta=max-min	Rank
U	-6.006	-6.715	-7.270	1.264	3
V	-9.962	-6.813	-3.216	6.746	1
f	-4.063	-7.135	-8.793	4.731	2
Total mean S/N= -6.70					

4.2. The Analysis of Variance (ANOVA) Method

The analysis of variance (ANOVA) is a useful standard statistical tool carried out to determine which parameters significantly influence on quality characteristics. Percent contribution of factors are also calculated throughout ANOVA analysis [19]. This is accomplished by separating the overall variability of the GRG, determined by the number of the square deviations from the GRG average, between the contributions and the error of each GMAW parameter. Namely;

$$S_T = S_p + S_e \tag{8}$$

where

$$S_T = \sum_{j=1}^{n} (\gamma_j - \gamma_m)^2 \tag{9}$$

and

SS_T	Total sum of mean square deviations
γ_j	Average response related to j^{th} experiment
γ_m	Grand mean of the response
n	Experiment run number
SS_p	Sum of square deviations for each parameters
SS_e	Sum of squared error-related deviations

The F value of Fisher's ratio, which is the ratio of the mean of squares deviations of the parameters to the total mean of the error, was also used to calculate how much the parameter influences the responses. Table 10 illustrates the summary of the calculated statistical results.

Table 10. Analysis of variance results for GMAW parameters

Parameter	Degree of freedom	Sum of square	Mean Square	F	Contribution (%)
U	2	0.00953	0.00477	0.31	2.39
V	2	0.23120	0.11560	7.47	57.99
f	2	0.12698	0.06349	4.10	31.85
Residual	2	0.03095	0.01547		7.76
Total	8	0.39866			100
S=0.124396 R-Sq=92.24% R-Sq (adj)=68.95					

In accordance with the ANOVA analysis, it is evident that welding speed (57.99% contribution), wire feed rate (31.85% contribution) are the most effective parameter while welding voltage (2.39% contribution) is the least effective parameter on ultimate tensile strength, joint efficiency and heat input. Figure 6 shows the percent contribution of GMAW parameters.

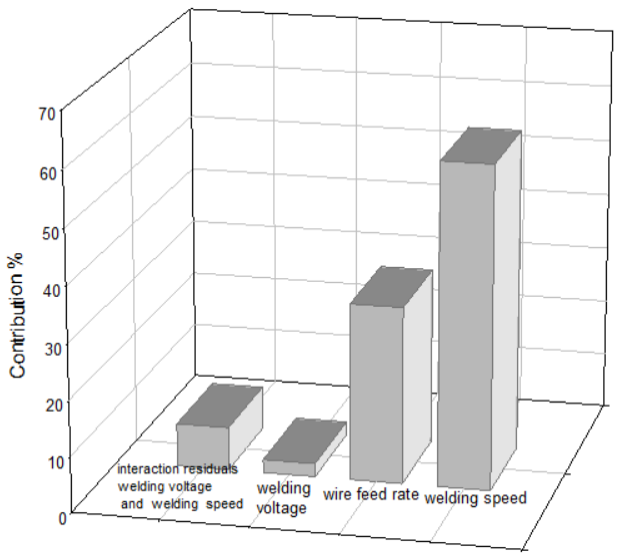

Figure 6. Contribution percentages of GMAW parameters

4.3. Confirmation Test

In this work, the confirmation test is conducted at optimal parameter combination ($U_1V_3f_1$) to verify the enhancement in the process responses and validity of the optimum welding condition. The predicted GRG ($\hat{\gamma}$) can be expressed as [19]:

$$\hat{\gamma} = \gamma_a + \sum_{i=1}^{p} (\bar{\gamma}_o - \gamma_a) \quad (10)$$

where γ_a is the total average GRG, $\bar{\gamma}_o$ is the average GRG at the optimal level, and p is the design parameter number [11,19]. Table 11 shows the confirmation test results.

Table 11. Confirmatory test results

	Initial parameter set up	Optimum parameter condition	
		Predicted	Experimental
Responses	$U_1V_1f_1$	$U_1V_3f_1$	$U_1V_3f_1$
UTS	794.125		816.21
JE	0.79		0.81
Q	0.145		0.099
S/N ratio for overall GRG	-6.63	0.04	-0.10
Overall GRG *Improvement in GRG is 0.53*	0.46	0.88	0.99

From the confirmatory test results, it is clear that improvement in overall GRG is obtained as 0.53.This is the main indicator of the proposed optimization methodology. Also, the method shows that higher UTS, JE and Q was obtained under determined optimum welding condition.

5. CONCLUSIONS

According to aforementioned results, this study also remarked the effectiveness of the Taguchi method on designing experiment and optimization under restricted number of experiments. It is concluded that the Grey relationship analysis based on the hybrid application of Taguchi was successful in solving a multi-criteria optimization problem. The best results for the responses of ultimate tensile strength of 816.21 MPa, joint efficiency of 0.81 and heat input of 0.099 kj/mm are obtained for the DP1000 workpiece using the optimum welding parameters of voltage of 17.50 V, welding speed of 380 mm/min and wire feed rate of 2.20 m/min under current of 45 A. So, ultimate tensile strength, joint efficiency and heat input in gas metal arc welding process is greatly enhanced by using hybrid Taguchi based grey relation method.

REFERENCES

[1] Karatas, M. (2018). Optimization of GMAW Process Parameters for Improving Mechanical Properties of DP1000 Steel Joint, MSc Thesis. Cukurova University Institute of Natural and Applied Sciences.

[2] http://www.lincolnelectric.com (2014). Gas Metal Arc Welding. The Lincoln Electric Company, 22801 Saint Clair Avenue. Cleveland, OH, 44117, U.S.A.

[3] Martinez R.T., Bestard, G.A., Silva, A.M.A., Alfaro, S.C.A. (2021). Analysis of GMAW process with deep learning and machine learning techniques. Journal of Manufacturing Processes 62: 695–703.

[4] Huang, Y., Yang, D., Wang, K., Wang, L., Fan, J. (2020). A quality diagnosis method of GMAW based on improved empirical mode decomposition and extreme learning machine. Journal of Manufacturing Processes 54:120-128.

[5] Sivasakthivel, P.S., Sudhakaran, R. (2020). Modelling and optimisation of welding parameters for multiple objectives in pre-heated gas metal arc welding process using nature instigated algorithms. Australian Journal of Mechanical Engineering, 18: 76-87.

[6] Chauhan, M.J. (2017). Optimization of parameters for gas metal arc welding of mild steel using Taguchi's technique. International Journal of Current Engineering and Scientific Research, 4(8): 1-8.

[7] Aghakhani, M., Mehrdad, E., Hayati, E. (2011) Parametric Optimization of Gas Metal Arc Welding Process by Taguchi Method on Weld Dilution. International Journal of Modeling and Optimization,1(3): 216-220.

[8] Kumar, A., Khurana, M.K., Pradeep, K. Y. (2016). Optimization of Gas Metal Arc Welding Process Parameters. IOP Conf. Series: Materials Science and Engineering, 149: 1-11.

[9] Rizvi, S.A., Wajahat, A. (2020). Multi attribute decision making parametric optimization in weld bead by gas metal arc welding through grey relation analysis: A case study. International Journal of Engineering, Science and Technology, 12(2): 59-66.

[10] Arya, DM., Chaturvedi V., Vimal, J. (2013). Parametric optimization of mig process parameters using Taguchi and grey Taguchi analysis, International journal of research in engineering & applied sciences, 3(6): 2249-3905.

[11] [11] Esme, U., Bayramoglu, M., Kazancoglu, Y., Ozgun, S. (2009). Optimization of Weld Bead Geometry in Tig Welding Process Using Grey Relation Analysis And Taguchi Method. Materiali in Tehnologije, 43(3): 143-149.

[12] Srivastava, S., Garg, R.K. (2017). Process parameter optimization of gas metal arc welding on IS: 2062 mild steel using response surface methodology, Journal of Manufacturing Processes 25: 296–305.

[13] Singla M., Singh, D., Deepak, D. (2010). Parametric Optimization of Gas Metal Arc Welding Processes by Using Factorial Design Approach. Journal of Minerals & Materials Characterization & Engineering, 9(4): 353-363.

[14] Ambekar, S.D., Wadhokar, S.R. (2015). Parametric Optimization of Gas metal arc welding process by using Taguchi method on stainless steel AISI 410. Modern Engineering and Emerging Technology, 3(1): 1-9.

[15] Yadav, R.K., Jain, N., Thakur, K. (2015). Parametric Optimisation of Gas Metal arc Welding Process with the Help of Taguchi Method on Tensile Strength – A Review. International Journal of Engineering Research & Technology, 4(4): 223-226.

[16] Sreeraj, P., Kannan, T., Maji, S., (2013). Optimization of GMAW Process Parameters Using Particle Swarm Optimization. ISRN Metallurgy, 2013: 1-10.

[17] Shao, Q., Xu, T., Yoshino, T., Song, N. (2017). Multi-objective optimization of gas metal arc welding parameters and sequences for low-carbon steel (Q345D) T-joint, Journal of Iron and Steel Research. Journal of Iron and Steel Research, International 21: 511- 555.

[18] Kshirsagar, R., Jones, S., Lawrence, J., Tabor, J. (2020) Optimization of TIG Welding Parameters Using a Hybrid Nelder Mead-Evolutionary Algorithms Method. Journal of Manufacturing and Materials Processing, 4(10): 1-21.

[19] Datta, S., Bandyopadhyay, A., Kumar, P.P. (2008). Grey-Based Taguchi Method for Optimization of Bead Geometry in Submerged Arc Bead-On-Plate Welding. International Journal of Advanced Manufacturing Technology volume 39: 1136-1143.

[20] http://www.ssab.com.tr/products/brands/docol/products/docol-1000dp (2009). Welding of Domex and Docol Advanced High Strength Steels. SSAB Tunnplat AB SE-781 84 Borlange, Sweden [accessed 30 June 2018].

EUROPEAN MECHANICAL SCIENCE
e-ISSN: 2587-1110

Research Paper

Finite Element Simulation of Dent Resistance for Automotive Rear Bumper

İlker Bahar[1*]

[1]TOFAŞ Türk Otomobil Fabrikası A.Ş R&D Center, Bursa, Turkey

Abstract

In automotive industry, there is an increasing demand for weight reduction. On the other hand extraordinary style for automotive exteriors are used in order to increase number of sales. As a result, the usage of different shapes for exterior bumpers is getting increased. Because of that, finite element simulation of dent resistance for automotive bumpers has become a very important step in early steps of automotive design. In this paper, static dent resistance for automotive exterior rear bumper is investigated by using nonlinear finite element method. The thickness change for different areas of bumper is considered from CAD data. In addition, nonlinear mechanical properties such as plastic behavior of rear bumper material are used in the finite element simulations. In addition, the results that are obtained from physical test are also presented here to compare with the results of finite element simulations to see percentage of correlation. This study is mainly focused on the correlation between finite element simulations and physical test results. The finite element simulation results show us that the percentage of correlation with the physical test results is reasonable. Consequently, due to high percentage of correlation between nonlinear finite element results and physical test results, the nonlinear finite element results should be taken into account in early steps of automotive design in order to reach minimum cost and get the most robust solution to eliminate quality problems which may occur in the future.

Keywords: Automotive exterior bumper, denting resistance, hyperelastic material, nonlinear finite element simulation, static analysis.

1. INTRODUCTION

Nowadays, development of automotive industry leans on using more light weighted materials and production processes as well known to decrease emission rates. On the other hand, there is a greatest challenge at this side an automobile should be not only safer, more comfortable but also different style lines in order to get a step forward. According to grip this value commonly, the usage of different type shapes and material in automotive exterior front and rear bumper is increasing [1,2,3].

In open literature, the studies that are related with finite element simulations of dent resistance for automotive panels and correlation studies between simulations and experiments can be found. Dylan et al. compared between experimental results and finite element simulations in terms of static and dynamic denting. They dented panels with various thickness by using a steel ball. They used LS-Dyna and Abaqus for finite element simulations. At the end of study, they shown that is important using correct material data, the best suitable element formulations, hardening effects and mesh quality [4]. Vreede et al. investigated influence of material properties and geometric shape of panel on their study. Also, they compared between finite element simulation results and experimental results [5]. Sakai et al. analyzed the stiffness of an automotive outer surface panel from both aspects of finite element analyses and experimental results in their study. Their study shows that the stiffness is influenced from rigidity areas and the characteristic of denting is stronger in surfaces with small radius [6]. Holmerg and Nejabat studied on automotive side door's stiffness and dent properties. They analyzed side door in two steps by using finite elements simulations. At first step, the stamping effects were not taken into account but, at second step vice versa. They showed the accuracy level of simulations with stamping effect in their study [7]. Heckmann et al. study on approach that reduces sheet thickness and subsequent of weight automotive thin panel sheets by increasing denting resistance of them. They investigated extrinsic stress on the components should be produced in a dedicatedly aligned shape [8]. Jeong developed a design software that uses empirical equations to predict denting stiffness value of panels.

* Corresponding author
Email: ilker.bahar@tofas.com.tr

European Mechanical Science (2021), 5(4): 214-219
doi: https://doi.org/10.26701/ems.875571
Received: February 6, 2021
Accepted: May 17, 2021

By using this, an optimization period is used in early phases development of an automotive [9].

This study shows an objective measurement and consistent correlation level of static dent resistance for exterior rear bumper that used an automotive with new design. The higher percentage of correlation leads virtual analysis team and design team to achieve the robust solution in early steps of design processes. Respectively, an automobile rear bumper has been investigated in terms of targets that defined in physical test and virtual analysis norms. Moreover, mechanical properties of bumper's material were obtained from test results. Because of production and material, same areas have different thickness ratio compared to other. So, all thicknesses were included to create correct finite element model. At the end of the study, physical test results and finite element simulation results were evaluated and compared.

2. MATERIAL AND METHOD

As known from the literature, the FEMs generated in solvers are usually nonlinear and can involve from a few to thousands of variables. In terms of these variables the equilibrium equations obtained by discretizing the virtual work equation can be written symbolically as Eq. (1) below [14]:

$$F^N\left(u^M\right)=0 \tag{1}$$

Where is the force component conjugate to the variable in the problem and is the value of the variable. Many of the simulations are history dependent, so the solution must be developed by a series of "small" increments. Two issues arise: how the discrete few to thousands of variables equilibrium statement Eq. (1) is to be solved at each increment, and how the increment size is chosen. Generally, finite element solvers use Newton's method as a numerical technique for solving the nonlinear equilibrium equations. The motivation for this choice is primarily the convergence rate obtained by using Newton's method compared to the convergence rates exhibited by alternate methods such as modified Newton or quasi-Newton methods for the types of nonlinear problems. The basic formalism of Newton's method is as Eq. (2) follows [13]:

$$x_1 = x_0 - \frac{f(x_0)}{f'(x_0)} \tag{2}$$

This process may be repeated as many times as necessary to get the desired accuracy. In general, for any x-value , the next value given by Eq. (3) below [14]:

$$x_{n+1} = x_n - \frac{f(x_n)}{f'(x_n)} \tag{3}$$

What Newton's method actually does can be seen from Fig. 1-a:

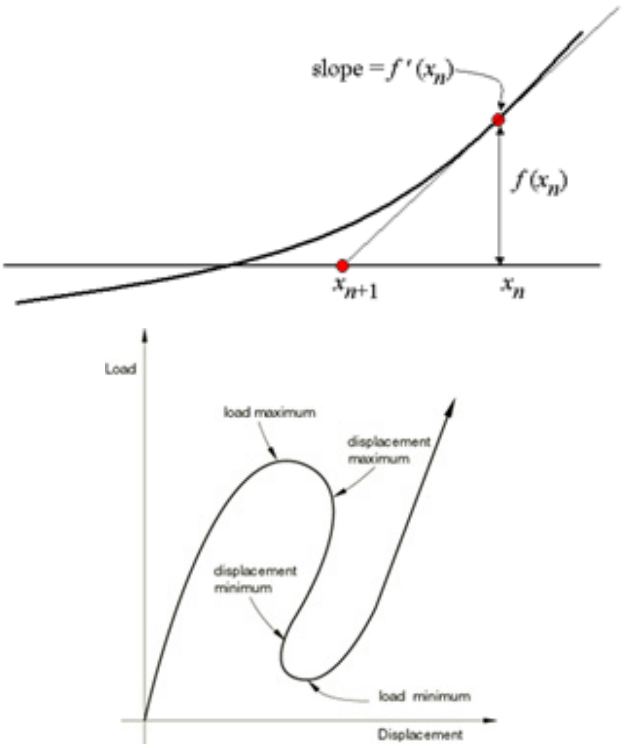

Figure 1. a) Demonstrate of Newton's Method, b) Typical unstable static response

Dent resistance simulations are usually unstable problems due to buckling. It is often necessary to obtain nonlinear static equilibrium solutions for unstable problems, where the load-displacement response can exhibit the type of behavior sketched in **Fig. 1-b**. During periods of the response, the load and/or the displacement may decrease as the solution evolves. The modified Riks method is an algorithm that allows effective solution of such cases It is assumed that the response is reasonably smooth that sudden bifurcations do not occur. The basic algorithm remains the Newton method; therefore, at any time there will be a finite radius of convergence. Further, many of the materials (and possibly loadings) of interest will have path dependent response. For these reasons, it is essential to limit the increment size. In the modified Riks algorithm, along the tangent line to the current solution point and then searching for equilibrium in the plane that passes through the point thus obtained and that is orthogonal to the same tangent line [5]. In this study, the Newton method which is implemented in Abaqus was used.

3. NUMERICAL STUDIES

Loading conditions, constraints, thickness and material properties are critical parameters to be able to solve complicated denting resistance and complicated behavior of buckling. All of them should be defined correct. FCA technical terms that used during the whole study can be found at **Table 1**.

Detailed FEM of rear bumper is created to perform nonlinear buckling analyses mesh detail of rear bumper can be seen easily from **Figure 2**.

Table 1. Technical terms

Technical Terms	Explanation
Buckling	Recoverable, localized reversal of curvature failure
Permanent Dent	Residual visible deformation
Deflection	Maximum deformation at full load application.
Zone B	Zone name for main bumper area.
Zone C	Zone name large-unsupported area of bumper.
Zone D	Zone name for wheel openings of bumper.
Zone E	Zone name for body joints of bumper.
Zone F	Zone name for step pad area of bumper.
Zone I	Zone name for backup & read fog light lens of bumper.

Figure 2. Mesh Structure of Rear Bumper

Generally, FEM of an automotive BIW is modeled with shell elements. Because, almost 95% of an automotive structure created from thin sheet plates. So, they can be modeled by using shell theorem as **Figure 3-a**. Adhesives and other parts which are not suitable for shell theorem are modelled with 3D solid continuum elements (non-reduce) which can be seen from **Figure 3-b**. Morover, fasteners such as spot welds are modeled as point element. They had beam section which is rod attribute with 5mm. Bolt connections are modeled with rigid elements which are constrained in all degree of freedoms from independent nodes.

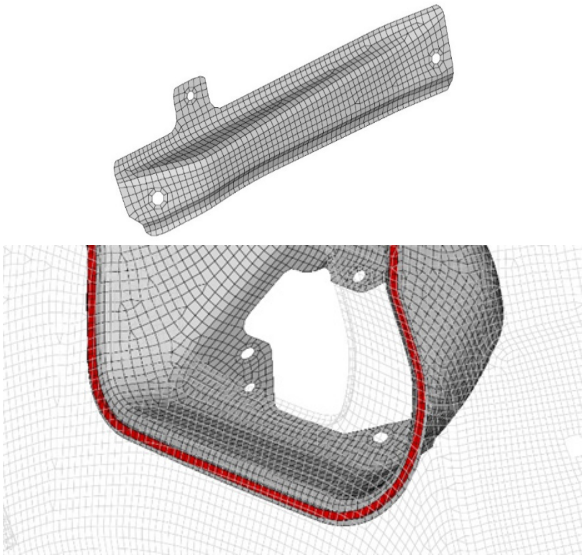

Figure 3. a) 2D Modelling of FE, b) 3D Modelling of FE

The indenter which consist of a cylindrical pusher and a cover is modelled by using 3D solid continuum elements which are hybrids (hyperelastic material) for applying force to bumper surface in tangent direction. The cylindrical pusher has 80 mm. diameter top hat. The indenter cover is 7.5 mm thick and made from high-density foam sheet. Detailed FEM of the indenter can be seen from **Figure 4**.

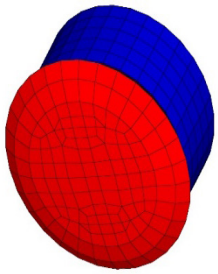

Figure 4. FEM of the Indenter

Element quality is very important for finite element analyses. Especially, it can be main problem for convergence ratio such as buckling analysis which are highly non-linear [15]. It's clear that using quad elements instead of triangle elements always gives better results. So, equality for whole model shown at **Table 2** below.

Table 2. Summary of element quality

	Value	Pass Criteria
Tria Ratio for Comps	4.8	≤ 5.0
Maximum Warpage	19	≤ 20.0
Aspect Ratio	2.8	≤ 3.0
Skewness	42.2	≤ 45.0
Jacobian	0.61	≥ 0.6

Usage of correct material properties for nonlinear analysis is so important in case a target which is defined in terms of number such as deformation [16]. Thus, the rear bumper's material which is PP 48.380 modelled as isotropic behavior with included plastic behavior that extracted from test results. PP 48.380 is a Polypropylene which is filled with mineral (talc). The material of parts for half model are also included with material which have detail behavior for this analysis. All sheet's material properties are extracted form tensile tests and applied for each steel part separately. The used materials are FEP02, FEP04, FEP05, FE180BH, FE210IF, FE 600DP, FE 1000DP which are introduced according to FCA Norms [15].

The indenter's material has a hyperelastic behavior in simulations. So, it is important to usage of correct material for indenter. When the indenter pushed to rigid wall, the behavior of the intender pusher and the indenter of cover act like graph below. Shape change of the indenter under force also can be seen from **Graph 1**. Wireframe with blue color represents initial position of the indenter and red color represents deformed shape of the indenter.

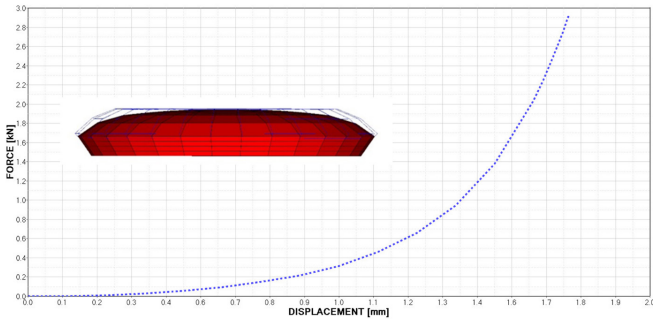

Graph 1. Behavior of the indenter

Dent resistance problems are local issue problems. So that in order to decrease computation time, half FEM is used as **Figure 5-a**. Intersection nodes which lean on cutline are constrained in all degree of freedoms. Loading conditions for indenter are shown at **Figure 5-b**. Indenter is positioned to tangent of bumper surface and load applied in local normal to indenter. Indenter constrained all degree of freedoms except normal direction of surface tangent. When the force reached to target value, the force is removed in axial direction and indenter moved from current position back to initial position.

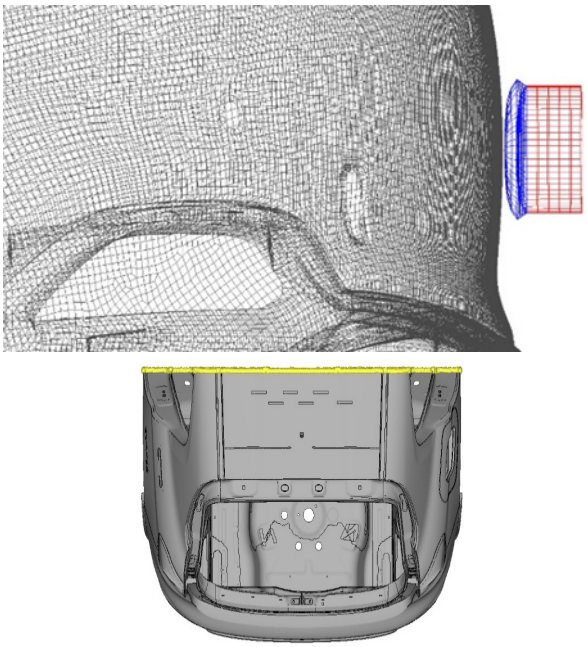

Figure 5. a) Boundry conditions b) Loading conditions

Bumper's area divided to specific zones which are described in norms [16]. These zones have no specific loading points, but all zones have different pre-defined pass criteria which are described in **Table 1**. According to loading zones, the indenter is positioned. Loading points of the indenter shown at **Figure 6**. Only loading point with red circle which leans on Zone B (Main Bumper) is selected for this study.

FEM is prepared on Hypermesh 2017.2.3 and solved by using ABAQUS 6.14 in nonlinear implicit solver. Results post-processed by using Hyperview 2017.2.3. Similar to [10,11,12], U, S, PEEQ and RF are requested for the results and plotted for graphs. Maximum displacement for loading can be seen from **Figure 7-a**. Pass criteria is defined as maximum displacement should be lower than 15mm. Permanent displacement with small denting after removing load slowly is shown at **Figure 7-b**. Permanent displacement according to pass criteria should be lower than 1mm. It is also known that dents higher than 0.5mm can be seen easily from anyone.

According to finite element result, force-displacement is plotted by using reference node values of the indenter and the reference node values of bumper. From **Graph 2**, the stiffness change can be seen at 4.5mm and 12mm displacements. In addition, graph has similar zones that described in **Fig. 1-b** except the buckling behavior.

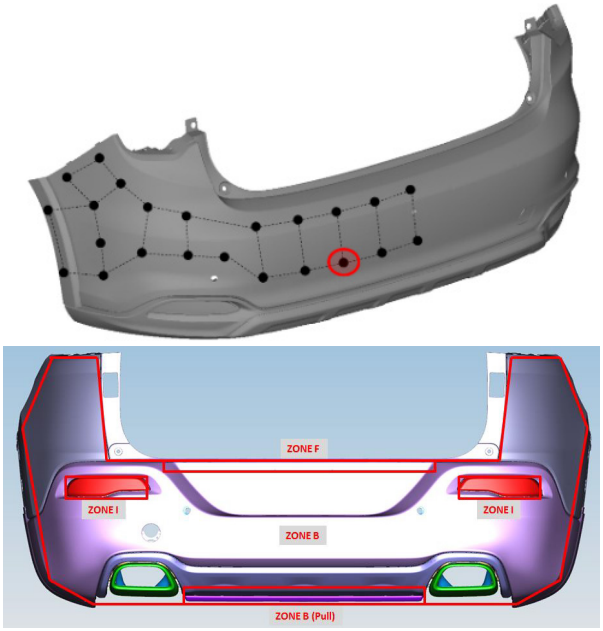

Figure 6. Indenter positions for bumper according to zones

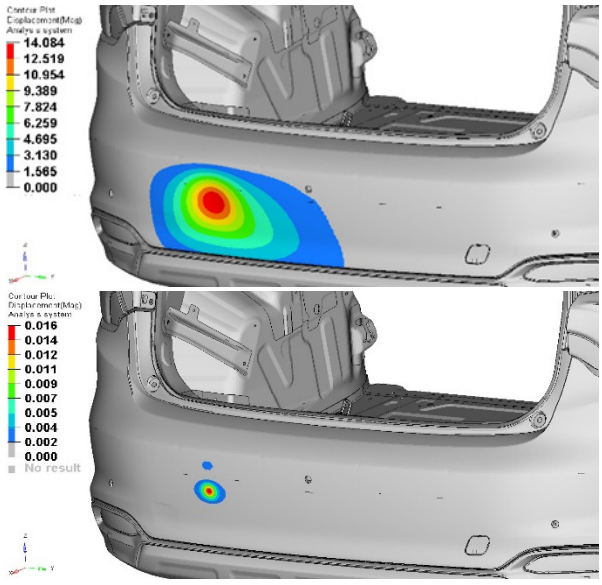

Figure 7. a) Maximum displacement contour b) Permanent displacement contour

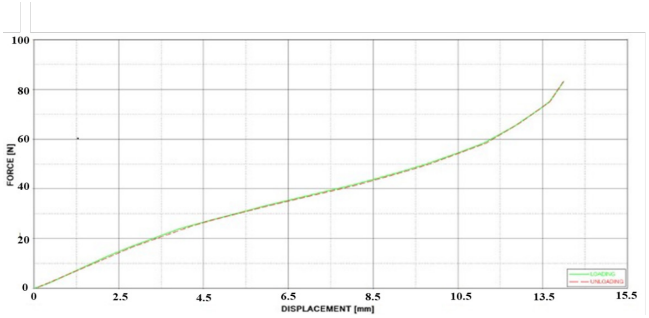

Graph 2. Force – displacement curve for current point extracted from analysis

4. EXPERIMENTAL VERIFICATIONS

The test vehicle is connected to a fixture which is rigid. A

general application can be seen from **Figure 8-a**. The load is applied from indenter according FCA test norm and removed in same axial direction which is normal to surface back. The maximum and permanent deformations are measured from linear displacement transducer. Also, reaction force of indenter is read from load cell as shown **Figure 8-a**. Loading point assessments for physical test setup shown at **Figure 9-b**. They are positioned to almost same location as FEM.

Figure 8. a) Typical physical test setup for denting resistance b) Loading point assessments

Physical test result for current position of indenter can be seen clearly from at **Graph 3** below. Stiffness changes which is result of contact between parts can be extracted from loading – unloading curves. In addition, no buckling behavior is seen in physical test result as finite element simulation. On the other hand, some differences can be extracted from graphs between physical test result and finite element simulation result.

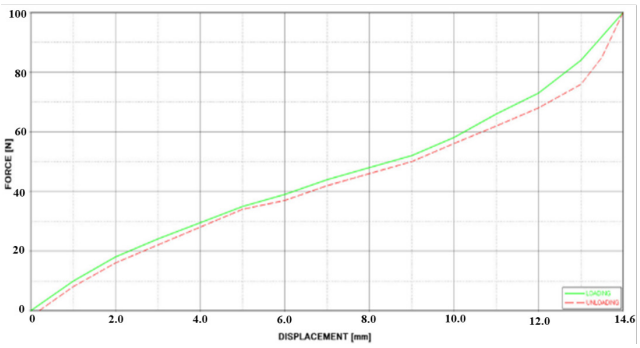

Graph 3. Force – displacement curve for current point extracted from physical test

5. DISCUSSIONS

The percentage of correlation status between finite element analysis and physical test is investigated by using force-displacement of actual point for loading and unloading conditions. Maximum and permanent deformations under static test load are so important to specify performance of a bumper. These parameters are also related with stiffness of bumper.

The other important thing is the buckling which is related with quality in terms of visible denting. As a result, several physical tests should be repeated in order to reach targets. Furthermore, it is required more prototype which means not only higher cost but also more waste of time. The better correlation between finite element simulations means that the less cost and waste of time.

Getting high percentage correlation is not easy at first step. In other words, some iterations are needed. For example, **Figure 9** shows us location difference between test (blue) and finite element simulation (red). At first step, the distance between two location is 20 mm in direction-y and 10 mm in direction-z. Although they are small distances, they cannot be ignored. In this scenario, the maximum displacement difference is 1.86 mm and the permanent set difference is 0.29 mm.

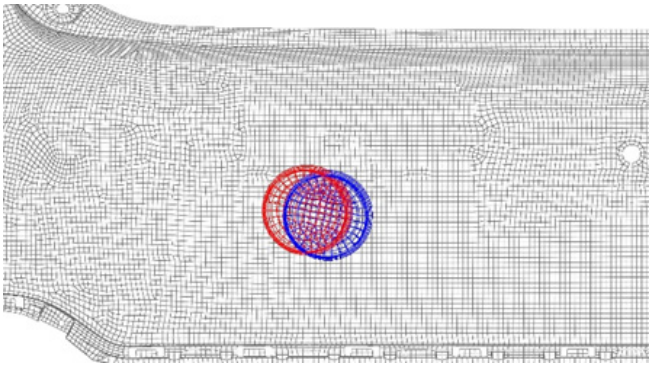

Figure 9. Correct and incorrect position of the indenter

The other issue is material properties and thickness. In this study material has been modeled like isotropic but, PP materials should be modeled composite in order to correct behavior. No action is taken for this issue because of necessary programs that are used for modeling composite materials.

Figure 10 shows the distribution of thickness. In early, same thickness has been used for whole model of bumper such as ribs, faces, radius but some areas have not same thickness ratio as other areas due to production processes in terms of molding, angle. Variable thickness ratio for different areas of same component location are so effective for deformations. For example, the maximum displacement difference between unique thickness and variables thickness is 1.22 mm and the permanent set difference between unique thickness and variables thickness is 0.11 mm.

After investigated issues above, some of them solved such positioning the indenter, correct thickness distribution but, any action taken for material modelling. The percentage of correlation status, between finite element simulation and physical test has been shown by using graph values at **Table 3**. With solved issues, correlation status got better as much

as need.

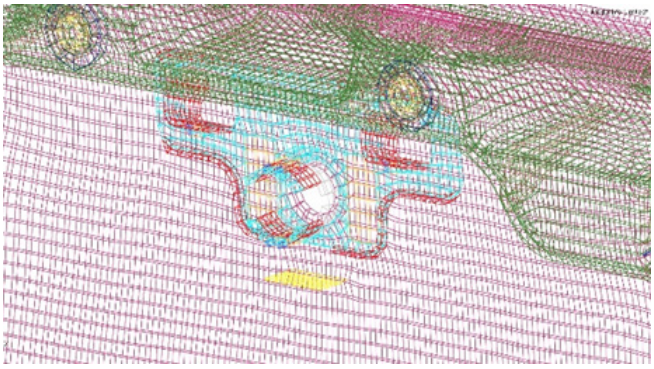

Figure 10. Thickness distribution of bumper's FEM

Table 3. Correlation Status

	Test	FEM	Diff %
Maximum Deformation [mm]	14.675	14.084	4.2
Permanent Deformation [mm]	0,020	0.016	25
Visible Denting	NO	NO	0.0

6. CONCLUSION

In this study, static dent resistance for automotive exterior rear bumper investigated by using nonlinear finite element method. In addition, the results that are obtained from physical test are also presented here to compare with the results of finite element simulations to see percentage of correlation. Results can be summarized below;

- All loading points should have positioned to exactly same location in both psychical tests and finite element simulations. A small different between positions effects results so that the percentage of correlation get worse.
- Not only bumper parts but also the other parts that belong to body in white should be into accounted in order to more accurate results. Because, nonlinear contact interactions are important for these type analyses.
- Material properties are also crucial effect for correlation. They should be defined correctly. In this study, PP material defined like Isotropic but composite behavior will effect the results.
- Thickness distribution for plastic parts so important. Because of production, generally plastic parts have different thicknesses on same components. They should be defined properly.

Due to the high coordination, these results show us that the number of prototypes can be reduced and optimization can be made at the same time by using finite element analysis in the early phases of automotive design processes.

7. NOMENCLATURE

CAD : Computer aided design

BIW : Body in white

FEM : Finite element model

U : Displacement

S : Stress

PEEQ : Equivalent plastic strain

RF : Reaction force

REFERENCES

[1] Shi, M., Brindza, J., Michel, P., Bucklin, P. et al. (1997). Static and Dynamic Dent Resistance Performance of Automotive Steel Body Panels. SAE Technical Paper 970158, DOI: https://doi.org/10.4271/970158

[2] Jung, D.W. (2004). A Parametric Study of Sheet Metal Denting Using a Simplified Design Approach. KSME International Journal, 16(12): 1479–1492.

[3] Mahmood, H. F. (1981). Dent Resistance of Surface Panel and Slam Area. SAE Technical Paper No. 810099, ISSN: 0148-7191, e-ISSN: 2688-3627, DOI: https://doi.org/10.4271/810099.

[4] Dylan, T., Hodgins, B., Worswick, M. (2001). Static and Dynamic Denting of Paint Laked aa6111 Panels: Comparison of Finite Element Prediction and Experiments. SAE Technical Paper No. 2001013047, DOI: https://doi.org/10.4271/2001-01-3047.

[5] Vreede, P. T., Tamis, P. J. Roelofsen, M. E. (1995). The Influence of Material Properties and Geometry on Dynamic Dent Resistance: Experiments and Simulations. Proceedings IBEC '95, International Body Engineering Conference, pp. 79–86.

[6] Sakai, H., Saito, K., Tsukada, H. (1983). Stiffness and Dent Characteristics of Body Outer Surface Panel-Finite Element Analysis and Experiment. Int. J. of Vehicle Design, 4(1): 13–22, DOI: 10.1504/IJVD.1983.061295.

[7] Holmberg, S., Nejabat, B. (2004). Numerical Assessment of Stiffness and Dent Properties of Automotive Exterior Panals. Materials and Design 25: 361-368, DOI: 10.1016/j.matdes.2003.12.005.

[8] Heckmann, M., Birkert, A., Scholle, M., Sobhani, M. (2018). Method to Increase Denting Stiffness of Car Body Skin Panels. Journal of Physics Conference Series 1063(1):012089, DOI: 10.1088/1742-6596/1063/1/012089.

[9] Jeong, D. W. (1983). A Parametric Study of Denting Using a Simplified Design Approach. the Korean Society of Mechanical Engineers, 26(8): 1472–1479, DOI: https://doi.org/10.3795/KSME-A.2002.26.8.1472.

[10] Zeng, D., Xia, Z. C. (2005). A Comparative Study of Dent Resistance Incorporating Forming Effects. SAE Technical Paper No. 2005010089, DOI: https://doi.org/10.4271/2005-01-0089.

[11] Werner, M. F. (1993). Finite Element Simulation of Steel Body Panel Performance for Quasi-Static Dent Resistance. Automotive Materials – IBEC'93.

[12] Sabbagh, M.A., Chavli, R. N., Montgomery Jay S. (1995). Quasi-Static Dent Depth Simulation Using Nonlinear FEA. IBEC'95 Automotive Body Materials, pp-87-90.

[13] ABAQUS Analysis Theory Manual. ABAQUS Inc., 2017.

[14] ABAQUS Analysis User's Manual. ABAQUS Inc., 2017.

[15] Altair Hyperworks 2017: Users Guide. Altair Engineering, Inc., Troy, Michigan.

[16] FCA Norms